Near-Field Radiative Heat Transfer between Plasmonic Nanostructures

JIN DAI

Doctoral Thesis in Physics
School of Information and Communication Technology
KTH Royal Institute of Technology
Stockholm, Sweden 2016

KTH School of Information and
Communication Technology
SE-164 40 Kista
SWEDEN

TRITA-ICT 2016:31
ISBN 978-91-7729-175-6

Akademisk avhandling som med tillstånd av Kungl Tekniska högskolan framlägges till offentlig granskning för avläggande av teknologie doktorsexamen i fysik onsdag den 07 december 2016 klockan 10.00 i Sal C, Electrum, Kungl Tekniska högskolan, Kistagången 16, Kista, Stockholm.

Tryck: Universitetsservice US AB

This thesis is dedicated to my parents, grandparents, and Hongyu Yan.

Abstract

Radiative heat transfer (RHT) due to coupled electromagnetic near fields can significantly exceed that dictated by Planck's law. Understanding such phenomenon is not only of fundamental scientific interest, but also relevant to a broad range of applications especially connected to nanotechnologies. This dissertation elaborates, through a scattering approach based on the rigorous coupled wave analysis method, how plasmonic nanostructures can tame the near-field RHT between two bodies. The transmission-factor spectra are corroborated by photonic band diagrams computed using a finite element method. The main work begins by showing that the phenomenon of spoof surface plasmon polariton (SSPP) guided on grooved metal surfaces can play a similar role as surface phonon polariton in enhancing the RHT between two closely placed plates. Since dispersions of SSPPs especially their resonance frequencies can be engineered through geometrical surface profiling, one has great freedom in tailoring spectral properties of near-field RHT. Further enhancement of RHT can be achieved through techniques like filling of dielectrics in grooves or deploying supercells. A thorough study of RHT between two 1D or 2D grooved metal plates confirms super-Planckian RHT at near-field limit, with 2D grooved metal plates exhibiting a superior frequency selectivity. We also present RHT with a more exotic type of plasmonic nanostructures consisting of profile-patterned hyperbolic metamaterial arrays, and show that with such plasmonic nanostructures one can achieve an ultrabroadband super-Planckian RHT.

Sammanfattning

Strålningsvärmeöverföring (radiative heat transfer, RHT) på grund av koppling av elektromagnetiska närfält kan avsevärt överstiga den som dikteras av Plancks lag. Att förstå sådana fenomen är inte bara av grundläggande vetenskapligt intresse, men också relevant för tillämpningar särskilt kopplade till nanoteknik. Denna avhandling undersöker, genom en rigorösa kopplade våg analysmetod, hur plasmoniska nanostrukturer kan bidra till att ändra spektrala egenskaper av RHT mellan två tätt placerade objekt. Resultaten verifieras av fotoniska banddiagram numeriskt beräknad med hjälp av finita elementmetoden. Arbetet börjar med att visa att fenomenet "spoof surface-plasmon polariton" (SSPP) kan spela en liknande roll som "surface-phonon polariton" för att öka RHT mellan två tätt placerade plattor. Eftersom dispersioner av SSPPs särskilt deras resonansfrekvenser kan manipuleras genom geometrisk ytprofilering, kan man ha en stor frihet att förändra spektrala egenskaperna hos närfält medierad RHT. En grundlig undersökning av RHT mellan två 1d eller 2d spårade metallplattor bekräftar super-Planckian RHT, med 2D spårade metallplattor uppvisar en överlägsen selektivitet av RHT över frekvens. Ytterligare förbättring av RHT kan ske genom metoder som att fylla i dielektrikum i spår eller designera superceller. Vi också studerade RHT med en mer exotiska typ av plasmoniska nanostrukturer - hyperbolisk metamaterial gitter - och visar att man kan uppnå med sådana metamaterial en ultrabredbands super-Planckian RHT.

Acknowledgements

Our accomplishments are never ours alone. They represent the combination of the greatest minds around us and in history along with our own humble efforts. I am indebted to many individuals and institutions for allowing me to work in a delightful environment and committing this dissertation.

This list begins with my supervisor for my master and PhD studies, Dr. Min Yan. His intellectual passion in science, deep numerical skills, positive attitude and easy going personality have make these past five years an exceedingly pleasurable experience. I have been aggressive and loudly sometimes during our academic discussions and he has never lost his temper and patiently convey his thought, which is almost always correct and enlightening. I would like to express my sincere gratitude for not only being my advisor, but also a good friend during these years. I also thank to Prof. Min Qiu as my co-supervisor for his support and guidance.

I would also like to thank Prof. Mingshan Zhao as my bachelor advisor who brings me to the world of photonics and introduces me to the Erasmus Mundus Master Programme which I joined later. Prof. Roel Baets and Prof. Heidi Ottevaera as the coordinators of Erasmus Mundus Master Propramme at Universiteit Gent and Vrije Universiteit Brussel gave me a lot of support and help; to them, other staffs, and classmates I have worked with, my deepest thanks.

My sincere appreciation also goes to Prof. Sergey I. Bozhevolnyi for offering me three month visit at his stimulating group at Syddansk Universitet. Your broad understanding of many subjects, your ability to explain the most difficult concepts in the simplest ways really impressed and inspired me.

I also thank Prof. Saulius Marcinkevičius for helping with the pump-probe measurements in their laboratory of ultrafast and near-field spectroscopy.

Most of the RHT simulations were performed on resources provided by the Swedish National Infrastructure for Computing (SNIC) at PDC Centre for High Performance Computing (PDC-HPC). I thank all the faculties at PDC-HPC for assistance concerning technical and implementational aspects.

I have also been fortunate to have wonderful colleagues and friends around me and share their knowledge and attitude to life. I would like to thank Dr. Yiting Chen for his help with nanofabrication, Dr. Sergey A. Dyakov for his collaboration on RHT, Dr. Fei Ding for his collaboration on HMM, Dr. Fei Ye for his collaboration on gold nanoparticles, Dr. Xi Chen, Dr. Qi Lu, Dr. Mounir Mensi, Dr. Himanshu Kataria, and Yun Feng for a lot of helpful discussions, Miao Zhang for proofreading of this thesis, Shuoben Hou, Ye Tian and Xu Sun as basketball and lunch buddies, and especially Madeleine Printzsköld for administration and other help. I would also like to thank many others who helped me in different ways.

Jin Dai
November 2016

Contents

Acronyms

1D	one-dimensional
2D	two-dimensional
CWES	complex wavenumber eigenvalue simulation
EMT	effective medium theory
FDTD	finite-difference time-domain
FEM	finite element method
GMP	grooved metal plate
G-SPP	gap-surface plasmon polariton
GSP	gap surface plasmon
HMM	hyperbolic metamaterial
MIM	metal-insulator-metal
PA	proximity approximation
PEC	perfect electric conductor
PMC	perfect magnetic conductor
RCWA	rigorous coupled-wave analysis
RHT	radiative heat transfer

SPhP	surface phonon polariton
SPP	surface plasmon polariton
SSPP	spoof surface plasmon polariton
TE	transverse electric
TM	transverse magnetic
TPV	thermophotovoltaic

List of Symbols

N_{eff}	effective mode index
Θ	mean energy of a Planck's oscillator
$\bar{\bar{\epsilon}}$	relative permittivity tensor
β_{gsp}	propagation constant of gap-surface plasmon polariton
β_{spp}	propagation constant of surface plasmon polariton
β	propagation constant or surface-parallel wavevector
δ_{BB}	Stefan-Boltzmann constant
$\delta_{\alpha\alpha'}$	Kronecker delta
δ	Dirac function
ϵ_0	permittivity of free space
$\epsilon_{\parallel}$	relative permittivity component parallel to optical axis
$\epsilon_{\perp}$	relative permittivity component perpendicular to optical axis
γ	collision frequency
$\hbar$	reduced Planck constant
$\mathbb{I}$	identity matrix
$\mathbf{B}$	magnetic induction

$\mathbf{D}$	electric displacement
$\mathbf{E}$	electric field
$\mathbf{H}$	magnetic field
$\mathbf{P}$	electric polarizability
$\mathbf{R}$	reflection matrix
$\mathbf{T}$	transmission matrix
$\mathcal{E}$	Fourier space electric field
$\mathcal{H}$	Fourier space magnetic field
$\mathbf{j}^{\mathbf{f}}$	fluctuating current density
$\mathbf{j}$	current density
$\mathcal{T}_j$	transmission factor, $j \in \{s, p\}$ represents the polarization
μ_0	permeability of free space
ω_{p}	volume plasmon frequency
ω_{sp}	surface plasmon frequency
ω	angular frequency
ρ	charge density
c_0	speed of light in vacuum
g^E	electric Weyl component
g^H	magnetic Weyl component
k_0	amplitude of wavevector in vacuum
k_B	Boltzmann constant
q	heat flux

$\overline{\overline{\mathbf{G}}}^{E}$	electric dyadic Green's function
$\overline{\overline{\mathbf{G}}}^{H}$	magnetic dyadic Green's function

List of Publications

Publications included in the thesis

[1] J. Dai, S. A. Dyakov, and M. Yan, "Enhanced near-field radiative heat transfer between corrugated metal plates: Role of spoof surface plasmon polaritons," Phys. Rev. B **92**, 035419 (2015).

[2] J. Dai, S. A. Dyakov, and M. Yan, "Radiative heat transfer between two dielectric-filled metal gratings," Phys. Rev. B **93**, 155403 (2016).

[3] J. Dai, S. A. Dyakov, S. I. Bozhevolnyi, and M. Yan, "Near-field radiative heat transfer between metasurfaces: A full-wave study based on two-dimensional grooved metal plates," Phys. Rev. B **94**, 125431 (2016).

[4] J. Dai, F. Ding, S. I. Bozhevolnyi, and M. Yan, "Ultrabroadband super-Planckian radiative heat transfer with profile-patterned hyperbolic metamaterial," arXiv preprint arXiv:1609.04319 (2016).

Other relevant publications not included in the thesis

[5] S. A. Dyakov, J. Dai, M. Yan, and M. Qiu, "Near field thermal memory based on radiative phase bistability of VO_2," J. Phys. D: Appl. Phys. **48**, 305104 (2015).

[6] S. A. Dyakov, J. Dai, M. Yan, and M. Qiu, "Thermal self-oscillations in radiative heat exchange," Appl. Phys. Lett. **106**, 064103 (2015).

[7] Y. Chen, J. Dai, M. Yan, and M. Qiu, "Metal-insulator-metal plasmonic absorbers: influence of lattice," Opt. Express **22**, 30807–30814 (2014).

[8] S. A. Dyakov, J. Dai, M. Yan, and M. Qiu, "Thermal radiation dynamics in two parallel plates: The role of near field," Phys. Rev. B **90**, 045414 (2014).

[9] M. Yan, J. Dai, and M. Qiu, "Lithography-free broadband visible light absorber based on a mono-layer of gold nanoparticles," J. Opt. **16**, 025002 (2014).

[10] X. Chen, Y. Chen, J. Dai, M. Yan, D. Zhao, Q. Li, and M. Qiu, "Ordered Au nanocrystals on a substrate formed by light-induced rapid annealing," Nanoscale **6**, 1756–1762 (2014).

[11] Y. Chen, J. Dai, M. Yan, and M. Qiu, "Honeycomb-lattice plasmonic absorbers at NIR: anomalous high-order resonance," Opt. Express **21**, 20873–20879 (2013).

[12] J. Dai, F. Ye, Y. Chen, M. Muhammed, M. Qiu, and M. Yan, "Light absorber based on nano-spheres on a substrate reflector," Opt. Express **21**, 6697–6706 (2013).

List of Figures

List of Tables

Chapter 1

Introduction

The word *Heat* is not a scientific term but we use it quite often in scientific world without ambiguity. Scottish scientist James Clerk Maxwell describes his definition of heat in four stipulations in his book *Theory of Heat* [1]:

- *Heat, then, is something which may be transferred from one body to another, so as to diminish the quantity of heat in the first and increase that in the second by the same amount.*
- *We have therefore a right to speak of heat as of a measurable quantity, and to treat it mathematically like other measurable quantities so long as it continues to exist as heat.*
- *We shall find, however, that we have no right to treat heat as a substance, for it may be transformed into something which is not heat, and is certainly not a substance at all, namely, mechanical work.*
- *We have, therefore, reason to believe that heat is of the same nature as mechanical work, that is, it is one of the forms of Energy.*

There are three universal types of heat transfer: conduction, convection, and thermal radiation. Thermal conduction describes thermal energy transfer through atomic lattice by free electrons or by phonon-phonon interactions due to a temperature gradient formed in the solid. In gases and liquids, thermal energy transfer is through fluid motion, which is called convection. Both of them need the presence of a medium as a carrier to convey thermal energy. However, thermal energy transfer can happen even between two bodies placed in vacuum through radiation in the form of electromagnetic waves or photons. Such phenomenon is formally known as the radiative heat transfer (RHT). We are living in an environment full of thermal radiation, since every material above absolute zero emits electromagnetic waves. However, we are not always aware of it. This is because objects at room temperature radiate dominantly electromagnetic waves at infrared frequencies, which are

not perceivable by our naked eyes. As the temperature of an object gets higher, we can both see and feel its radiant heat. For example, we can see the glowing of an iron heated up near its melting point, and in a clear winter day we can feel the sun is warm even the environment is near the freezing point. The thermal radiation can play an important role for scenarios when thermal conduction and convection are obstructed, intentionally or unintentionally, such as devices operating in space. Therefore, there is a demand for engineering the thermal radiation properties of an object to control heat dissipation via radiation.

During the 19th and early 20th century, a lot of theoretical and experimental studies have been carried out by our pioneers to investigate heat and radiation [2–11]. These work are undoubtedly the cornerstones of thermodynamics and thermal radiation. Kirchhoff's law states that the spectral directional emittance of a point on the surface of a thermal radiator at any temperature is equal to the spectral absorbance for radiation incident from the same direction [2]. Planck's law gives the spectral energy density of radiation emitted by a blackbody, which is an idealized concept describing a body that absorbs all the electromagnetic waves, regardless of their frequencies, polarizations, or directions [10]. It sets a far-field limit of the maximum spectral density of electromagnetic radiation that a body at a given temperature can emit, which is also known as Planck's blackbody limit. Their work inspire us and pave the way to understand and tame the thermal radiation properties.

More recently, with the advances in modern nanofabrication technology and computing power in the past decades, people have entered *the room at the bottom*, starting to investigate the optical responses of nanostructured materials both numerically and experimentally. A lot of interesting and exotic optical properties in light absorption/radiation have been achieved by utilizing metamaterials, which are artifical materials composed of sub-wavelength structures [12–16]. Researchers have demonstrated perfect light absorbers which almost absorb all incoming light at normal incidence at certain wavelengths in the near-infrared regime [17, 18]. Later on, metamaterial-based perfect absorbers have been extended to visible frequencies with a broadband absorption spectrum [19, 20]. Since then, a lot of effort has been invested to achieve light absorption with a tailored spectrum through nanostructure engineering. Tailored absorption spectrum can be applied to many applications, including solar energy harvesting [21–24], biomedical sensing [25], optical black holes [26], invisible cloaks [27–29], bolometers [30], etc. Following the guidance of Kirchhoff's law, people have also demonstrated a variety of metamaterial-based thermal emitters with desired frequency selectivity, directionality, and polarization [31–39]. Even a coherent thermal source has been demonstrated using a SiC grating structure [40]. More recently, metamaterial exhibiting a highly anisotropic permittivity with hyperbolic dispersion, namely hyperbolic metamaterial (HMM) is utilized to achieve exotic phenomena, including super-resolution imaging [41, 42], thermal emission engineering [43], etc.

With the advent of nanofabrication technologies, more and more attention was paid to physical phenomena happening at nanoscale. A natural question arises,

what will the thermal radiation/absorption look like at a small distance, and how much is the radiative heat transfer (RHT) between two objects placed extremly close to each other. In Planck's book of *The Theroy of Heat Transfer* [44], he clearly states that *"Throughout the following discussion it will be assumed that the linear dimensions of all parts of space considered, as well as the radii of curvature of all surfaces under consideration are large compared with the wavelengths of the rays considered."* It implies that Planck's theory only describes thermal radiation property in the far-field limit. However, at the length scale smaller than the characteristic thermal wavelength, the tunneling of evanescent photons has to be taken into consideration for heat transfer process. Based on fluctuational electrodynamics formulation derived by Rytov [45, 46], Polder and van Hove established a rigorous theory for calculating RHT considering the coupling of evanescent waves which are excluded by Planck [47]. Their theory explains the anomalous RHT between flat metallic surfaces observed by Hargreaves at room temperature [48]. The theoretical proposition ignites the investigation of RHT at the near field. Using simple parallel-plate structure [49–59], sphere-sphere structure [60–64], nano-tip/sphere-plate structure [65–74], and even two parallel plates of metamaterials [75–85], people have demonstrated that the RHT can exceed the far-field limit predicted by Planck's law when the bodies are separated by a vaccum gap much smaller than the thermal wavelength. Very recently, this enhanced RHT has been observed experimentally across a gap size as small as a few nanometers with the advances in characterization techniques [59, 74]. This enhanced near-field RHT opens up new possibilities for many promising applications, such as radiative cooling [64, 86–88], nano-gap thermophotovoltaics (TPVs) [89, 90], thermal rectifications [91–102], thermal transistors [103, 104], thermal memory devices [105, 106], super-resolution lithography [107], etc.

Although the study of near-field RHT has grown considerably, there are still many aspects lacking of exploration, especially for realizing a better control of spectral properties of RHT. It is very important for applications such as daytime radiative cooling [64, 86–88] or nano-gap TPV [89, 90] where the emitter's spectra have to match the absorption spectra of heat reserviors or the efficiency curves of photovoltaics. Nowadays, most of the studies are based on simple homogeneous plates consisting of polar dielectrics or heavily doped semiconductors, such as SiC and highly doped silicon, due to their intrinsic surface phonon polaritons (SPhPs) in the infrared regime. However, the spectral properties of heat flux can hardly be tuned by changing the thicknesses of the plates. Even though there exist a few basic studies on more delicate structures, such as one-dimensional (1D)/ or two-dimensional (2D) metal gratings [78, 80–82], nanopores [76], and HMMs consisting of homogeneous multilayer of dielectrics and phonon-polariton metals [56–58] or nanowire arrays [77, 85], there still exist many challenges, from rigorous numerical computation of RHT between structured bodies to designing of nanostructures for achieving enhanced RHT with desired radiation spectra.

In this thesis, we thoroughly study the enhanced near-field RHT between plasmonic nanostructures using a rigorous scattering approach based on rigorous coupled-

wave analysis (RCWA). We demonstrate the advantage of using plasmonic nanostructure in taming the spectral properties of RHT, which has not been obtained by homogeneous plates. Our results convincingly show that nanostructured metal plates can serve as an important material platform for achieving enhanced RHT for a diverse range of application purposes.

This thesis is divided into six chapters. Chapter 2 gives an introduction of the theoretical background and concepts for understanding the RHT between plasmonic nanostructures, including surface plasmon polaritons (SPPs), gap surface plasmons (GSPs), spoof surface plasmon polaritons (SSPPs), and HMMs. Chapter 3 covers the different numerical methods for calculating near-field RHT in different structures, ranging from simple homogeneous plates to more delicate 1D/2D periodic nanostructures. A finite element method (FEM) for calculating the photonic band diagram of periodic structures has also been introduced in this chapter. Chatper 4 discusses RHT between nanostructures of two basic types, 1D/2D grooved metal plates, and 1D profile-patterned HMM arrays. The underlying physical mechanisms that enhance the RHT in these structures have been explicitly addressed. It gives a roadmap for designing nanostructures to achieve an enhanced RHT with specific spectral properties. Chapter 5 presents the overall conclusions of this thesis work and proposes the potential continuation of this work in the future. Finally, Chapter 6 gives the guideline to papers.

Chapter 2

Theoretical Background

This chapter introduces the concepts needed for understanding the underlying physical mechanisms of surface modes supported by plasmonic nanostructures which contribute to the enhanced near-field RHT. Sec. 2.1 and Sec. 2.2 briefly introduce surface plasmon polariton (SPP) supported by nobel metals with resonance frequencies in the ultraviolet regime and gap surface plasmon (GSP) resulted from introducing lateral terminations in metal-insulator-metal (MIM) structures, respectively. Sec. 2.3 introduces an artificial surface wave supported by nanostructured surfaces, i.e., spoof surface plasmon polariton (SSPP), which mimics SPP at infrared. Sec. 2.4 gives an introduction of two types of hyperbolic metamaterials (HMMs).

2.1 Surface Plasmon Polaritons

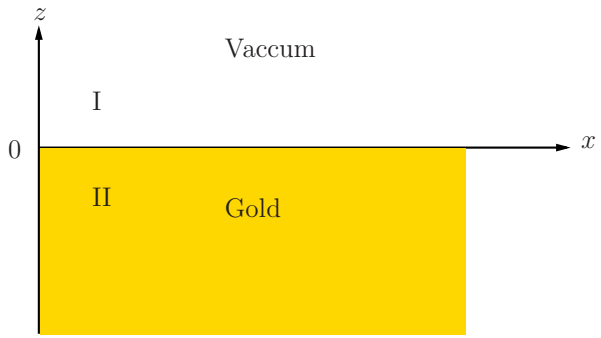

Figure 2.1: Geometry of a metal-dielectric interface between two semi-infinite media which supports surface plasmon polaritons.

SPPs are collective oscillation of free electrons on metal surfaces due to electromagnetic excitation. In its simplest picture, SPP propagates along a metal-dielectric interface and exponentially decays in the direction perpendicular to the interface into the neighboring media [108–112]. Figure 2.1 illustrates a simplest single-interface configuration which supports SPPs. The interface is formed by a semi-infinite metal and a semi-infinite dielectric medium. We choose gold as the metal medium whose relative permittivity can be described by a Drude model $\epsilon_1 = \epsilon_{\mathrm{Au}}(\omega) = 1 - \frac{{\omega_\mathrm{p}}^2}{\omega(\omega+i\gamma)}$, in which $\omega_\mathrm{p} = 9$ eV, and $\gamma = 35$ meV. We choose vacuum as the dielectric medium for simplicity $\epsilon_2 = \epsilon_{\mathrm{vacuum}} = 1$. To reveal the origin of SPP mode we have to find the eigenmode of the system without any external excitation by solving the Maxwell equations

$$\nabla \cdot \mathbf{D} = \rho, \tag{2.1a}$$
$$\nabla \cdot \mathbf{B} = 0, \tag{2.1b}$$
$$\nabla \times \mathbf{E} = -\frac{\partial \mathbf{B}}{\partial t}, \tag{2.1c}$$
$$\nabla \times \mathbf{H} = \frac{\partial \mathbf{D}}{\partial t} + \mathbf{j}. \tag{2.1d}$$

In the equations, $\mathbf{D}$ denotes the electric displacement, $\mathbf{B}$ the magnetic induction, $\mathbf{E}$ the electric field, $\mathbf{H}$ the magnetic field, $\mathbf{j}$ the current density, and ρ the charge density. The fact of source free of the system leads to $\mathbf{j} = 0$ and $\rho = 0$. Due to the evanescent nature of SPP we are aiming to find a surface wave propagating along x direction. Thus, the electric field and magnetic field can be then written as $\mathbf{E}(x, y, z) = \mathbf{E}(z)\mathrm{e}^{i\beta x}$ and $\mathbf{H}(x, y, z) = \mathbf{H}(z)\mathrm{e}^{i\beta x}$, respectively. Here, β is the propagation constant of the desired mode, which coincides with k_x in this problem. Substituting them into the wave equations

$$\nabla^2\mathbf{E} + k_0^2\epsilon\mathbf{E} = 0, \tag{2.2a}$$
$$\nabla^2\mathbf{H} + k_0^2\epsilon\mathbf{H} = 0, \tag{2.2b}$$

yields

$$\frac{\partial^2\mathbf{E}(z)}{\partial z^2} + (k_0^2\epsilon - \beta^2)\mathbf{E} = 0, \tag{2.3a}$$
$$\frac{\partial^2\mathbf{H}(z)}{\partial z^2} + (k_0^2\epsilon - \beta^2)\mathbf{H} = 0. \tag{2.3b}$$

For the time dependence ($\frac{\partial}{\partial t} = -i\omega$) and the homogeneity in y direction ($\frac{\partial}{\partial y} = 0$),

the two curl equations can be simplified to

$$\frac{\partial E_y}{\partial z} = -i\omega\mu_0 H_x, \tag{2.4a}$$

$$\frac{\partial E_x}{\partial z} - i\beta E_z = i\omega\mu_0 H_y, \tag{2.4b}$$

$$i\beta E_y = i\omega\mu_0 H_z, \tag{2.4c}$$

$$\frac{\partial H_y}{\partial z} = i\omega\epsilon_0\epsilon E_x, \tag{2.4d}$$

$$\frac{\partial H_x}{\partial z} - i\beta H_z = -i\omega\epsilon_0\epsilon E_y, \tag{2.4e}$$

$$i\beta H_y = -i\omega\epsilon_0\epsilon E_z. \tag{2.4f}$$

For TM or p modes, with non-zero components H_y, E_x, E_z, Eqs. 2.4d, 2.4f, and 2.3b give

$$E_x = -i\frac{1}{w\epsilon_0\epsilon}\frac{\partial H_y}{\partial z}, \tag{2.5a}$$

$$E_z = -\frac{\beta}{\omega\epsilon_0\epsilon}H_y, \tag{2.5b}$$

$$0 = \frac{\partial^2 H_y}{\partial z^2} + (k_0^2\epsilon - \beta^2)H_y, \tag{2.5c}$$

respectively. The analogous set for TE or s modes, with non-zero components E_y, H_x, H_z, can be expressed by

$$H_x = i\frac{1}{w\mu_0}\frac{\partial E_y}{\partial z}, \tag{2.6a}$$

$$H_z = \frac{\beta}{\omega\mu_0}E_y, \tag{2.6b}$$

$$0 = \frac{\partial^2 E_y}{\partial z^2} + (k_0^2\epsilon - \beta^2)E_y. \tag{2.6c}$$

Let's start looking for the solutions of TM mode. Applying Eqs. 2.5a-2.5c to the top and bottom half space depicted in Fig. 2.1 yields

$$H_y^{\mathrm{I}}(z) = A_{\mathrm{I}}\mathrm{e}^{i\beta x}\mathrm{e}^{-k_1 z}, \tag{2.7a}$$

$$E_x^{\mathrm{I}}(z) = iA_{\mathrm{I}}\frac{k_1}{\omega\epsilon_0\epsilon_d}\mathrm{e}^{i\beta x}\mathrm{e}^{-ik_1 z}, \tag{2.7b}$$

$$E_z^{\mathrm{I}}(z) = -A_{\mathrm{I}}\frac{\beta}{\omega\epsilon_0\epsilon_d}\mathrm{e}^{i\beta x}\mathrm{e}^{-ik_1 z}, \tag{2.7c}$$

and

$$H_y^{\mathrm{II}}(z) = A_{\mathrm{II}} \mathrm{e}^{i\beta x} \mathrm{e}^{k_2 z}, \tag{2.8a}$$

$$E_x^{\mathrm{II}}(z) = -iA_{\mathrm{II}} \frac{k_2}{\omega\epsilon_0\epsilon_m} \mathrm{e}^{i\beta x} \mathrm{e}^{ik_2 z}, \tag{2.8b}$$

$$E_z^{\mathrm{II}}(z) = -A_{\mathrm{II}} \frac{\beta}{\omega\epsilon_0\epsilon_m} \mathrm{e}^{i\beta x} \mathrm{e}^{ik_2 z}, \tag{2.8c}$$

respectively. k_1 and k_2 represent the z component of wavevectors in the top and bottom media which can be written as

$$k_1 = \sqrt{\beta^2 - k_0^2 \epsilon_d}, \tag{2.9a}$$

$$k_2 = \sqrt{\beta^2 - k_0^2 \epsilon_m}. \tag{2.9b}$$

By applying the boundary conditions at the interface z=0, which requires $H_y^{\mathrm{I}}(z = 0) = H_y^{\mathrm{II}}(z = 0)$ and $\epsilon_d E_z^{\mathrm{I}}(z = 0) = \epsilon_m E_z^{\mathrm{II}}(z = 0)$, we obtain

$$\frac{k_1}{\epsilon_d} + \frac{k_2}{\epsilon_m} = 0. \tag{2.10}$$

Substituting Eqs. 2.9a and 2.9b into it, we arrive at the dispersion relation of SPP propagating at the interface between two semi-infinite media

$$\beta_{\mathrm{spp}} = \frac{\omega}{c} \sqrt{\frac{\epsilon_d \epsilon_m}{\epsilon_d + \epsilon_m}}. \tag{2.11}$$

In Figs. 2.2(a) and 2.2(b), we plot the real and imaginary parts of propagating constant *vs* frequency curves for SPP given by Eq. 2.11, respectively. At low frequencies, the SPPs do not deviate too much from the light line. While, at frequencies close to the surface plasmon frequency $\omega_{\mathrm{sp}} = \frac{\omega_{\mathrm{p}}}{\sqrt{2}}$, the dispersion curve becomes a flat band with the group velocity approaching zero, which indicates a strong localization of electromagnetic field. To give a better understanding of SPPs, the electromagnetic field distributions corresponding to angular frequency of $\omega = 0.5\omega_{\mathrm{p}}$ are mapped in Fig. 2.3. We can see that the fields are strongly confined at the interface. As the frequency gets closer to ω_{sp}, this confinement can be even stronger. However, the imaginary part becomes larger, resulting a higher propagating loss and thus a shorter propagating length. As a result, there is a trade-off between field confinement and propagating length for using SPPs. By carrying out the same procedure for Eqs. 2.6a-2.6c and applying the boundary conditions of E_y and H_z at the interface, we end up with $A_{\mathrm{I}} = A_{\mathrm{II}} = 0$. It implies that SPPs only exist for TM polarization.

Now we turn to a slightly more complex MIM structure [113] consisting of two semi-infinite gold plates separated by a vacuum gap of thickness g [see Fig. 2.4],

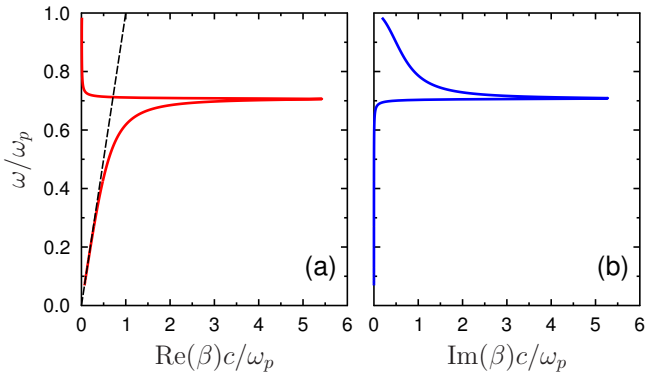

Figure 2.2: Dispersion relation of surface plasmon polariton at a vacuum-gold interface. (a) and (b) present the real and imaginary part of β, respectively. The dashed black line denotes the light line in vacuum.

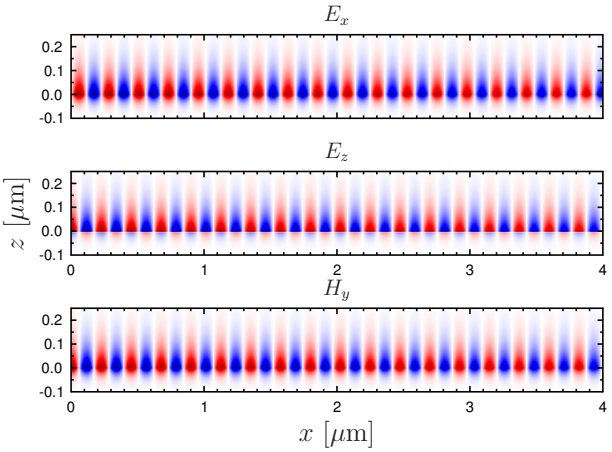

Figure 2.3: Electromagnetic field distribution of surface plasmon polaritons at a vacuum-gold interface at angular frequency $\omega = 0.5\omega_p$.

which is a well studied configuration for near-field RHT. For SPP modes, which

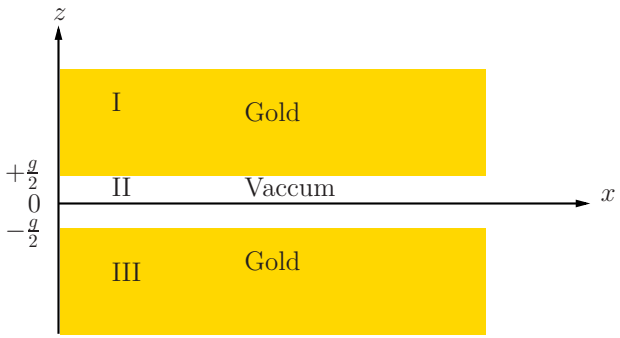

Figure 2.4: Geometry of metal-dielectric-metal structure consisting of two semi-infinite gold plates separated by a vacuum gap of g.

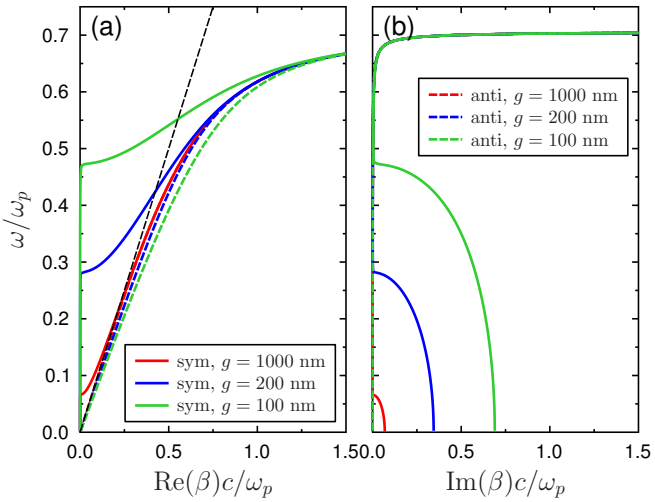

Figure 2.5: Dispersion relation of symmetric and antisymmetric surface plasmon polaritons supported by a metal-dielectric-metal structure depicted in Fig. 2.4 with different gap sizes g. (a) and (b) present the real and imaginary parts of β, respectively. The dashed black line denote the light line in vacuum.

only exist for TM polarization, the field components in the top gold plate are

$$H_y^{\mathrm{I}} = A\mathrm{e}^{i\beta x}\mathrm{e}^{-k_1 z}, \tag{2.12a}$$

$$E_x^{\mathrm{I}} = iA\frac{1}{\omega\epsilon_0\epsilon_m}k_1\mathrm{e}^{i\beta x}\mathrm{e}^{-k_1 z}, \tag{2.12b}$$

$$E_z^{\mathrm{I}} = -A\frac{\beta}{\omega\epsilon_0\epsilon_m}\mathrm{e}^{i\beta x}\mathrm{e}^{-k_1 z}, \tag{2.12c}$$

while for the bottom gold plate we get

$$H_y^{\mathrm{III}} = B\mathrm{e}^{i\beta x}\mathrm{e}^{k_1 z}, \tag{2.13a}$$

$$E_x^{\mathrm{III}} = -iB\frac{1}{\omega\epsilon_0\epsilon_m}k_1\mathrm{e}^{i\beta x}\mathrm{e}^{k_1 z}, \tag{2.13b}$$

$$E_z^{\mathrm{III}} = -B\frac{\beta}{\omega\epsilon_0\epsilon_m}\mathrm{e}^{i\beta x}\mathrm{e}^{k_1 z}. \tag{2.13c}$$

In the vacuum gap we have surface modes at both bottom and top metal-vacuum interfaces which decay in positive and negative z direction into the vacuum gap respectively. Thus the fields can be expressed by the superposition of them as

$$H_y^{\mathrm{II}} = C\mathrm{e}^{i\beta x}\mathrm{e}^{k_2 z} + D\mathrm{e}^{i\beta x}\mathrm{e}^{-k_2 z}, \tag{2.14a}$$

$$E_x^{\mathrm{II}} = -iC\frac{1}{\omega\epsilon_0\epsilon_d}k_2\mathrm{e}^{i\beta x}\mathrm{e}^{k_2 z} + iD\frac{1}{\omega\epsilon_0\epsilon_d}k_2\mathrm{e}^{i\beta x}\mathrm{e}^{-k_2 z}, \tag{2.14b}$$

$$E_z^{\mathrm{II}} = C\frac{\beta}{\omega\epsilon_0\epsilon_d}\mathrm{e}^{i\beta x}\mathrm{e}^{k_2 z}C\frac{\beta}{\omega\epsilon_0\epsilon_d}\mathrm{e}^{i\beta x}\mathrm{e}^{-k_2 z}. \tag{2.14c}$$

By applying the continuity of H_y and E_x at both interfaces ($z = \pm\frac{g}{2}$) one can get

$$\tanh\left(k_2\frac{g}{2}\right) = -\frac{k_2\epsilon_m}{k_1\epsilon_d}, \tag{2.15a}$$

$$\tanh\left(k_2\frac{g}{2}\right) = -\frac{k_1\epsilon_d}{k_2\epsilon_m}, \tag{2.15b}$$

in which k_1, k_2 are the z component of wavevectors in gold and vacuum, respectively. Solving these equations numerically for different gap sizes of $g = 1000,\ 200,\ 100$ nm gives us the dispersion curves shown in Fig. 2.5. Eqs. 2.15a and 2.15b describe the symmetric [$E_x(z)$ is an even function, $H_y(z)$ and $E_z(z)$ are odd functions] and antisymmetric [$E_x(z)$ is an odd function, $H_y(z)$ and $E_z(z)$ are even functions] SPPs, respectively. For gap size of an infinite thickness, Eqs. 2.15b and 2.15a reduce to the dispersion curve of SPP mode supported by a single vacuum-gold interface described by Eq. 2.10. As the gap size decreases, the coupling between SPPs supported at both vacuum-gold interfaces becomes much stronger. It splits the SPP mode into a symmetric and antisymmetric mode pair. It is worth noting that the antisymmetric modes [see dashed curves in Fig. 2.5], which exhibit odd symmetry of longitudinal electric field and even symmetry of transverse field, do not exhibit a cut-off even for an infinitely small gap size. This mode is also known as the gap-surface plasmon polariton (G-SPP) [114]. Figure 2.6 presents the symmetric and antisymmetric SPP mode profiles for gap size of $g = 100$ nm at angular frequency $\omega = 0.5\omega_{\mathrm{p}}$.

Besides SPP-related modes, this two-metal-plate structure, which is indeed a parallel-plate waveguide, also supports TM and TE waveguide modes. In the perfect electric conductor (PEC) approximation the dispersion of TM and TE guided modes

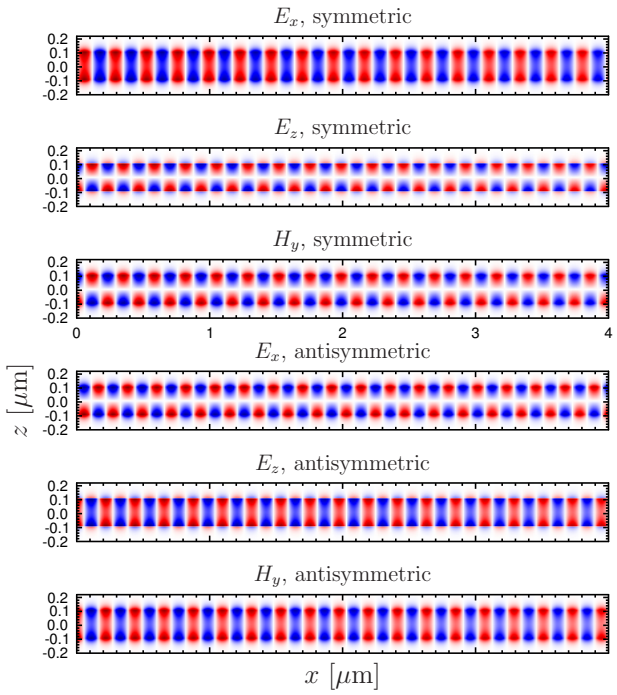

Figure 2.6: Electromagnetic field distributions of symmetric and antisymmetric surface plasmon polaritons at frequency $\omega = 0.5\omega_p$ supported by a metal-dielectric-metal structure depicted in Fig. 2.4 with gap size $g = 100$ nm.

can be described by

$$k_z = \sqrt{k_0^2 - \left(\frac{m\pi}{d}\right)},\ m \in \{0, 1, 2, 3\ \ldots\}, \tag{2.16}$$

and

$$k_z = \sqrt{k_0^2 - \left(\frac{m\pi}{d}\right)},\ m \in \{1, 2, 3\ \ldots\}, \tag{2.17}$$

respectively. We plot the numerically calculated dispersion relation of these waveguide modes and the corresponding field distributions at $\omega = 0.08\omega_\mathrm{p}$ in Fig. 2.7. The fundamental and the first-order TM waveguide modes TM_0 and TM_1 are the same as the low-frequency parts of the dispersion relation of antisymmetric and symmetric SPP modes. Due to the boundary condition at metal-vacuum interfaces [$E_z\left(z = \pm\frac{g}{2}\right) = 0$], except for the fundamental TM waveguide mode [TM_0

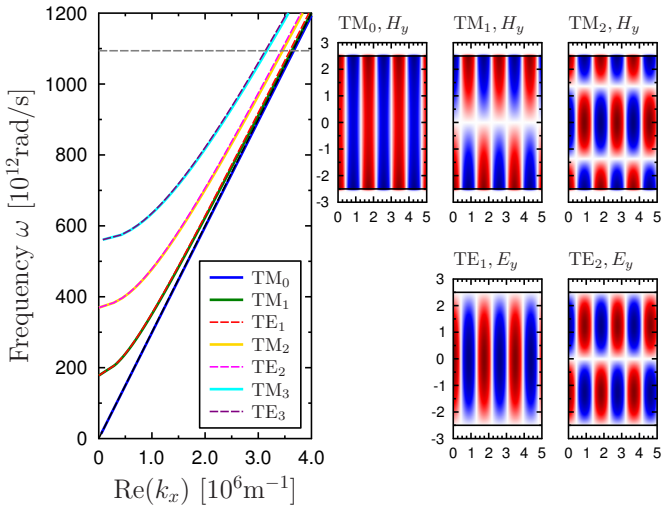

Figure 2.7: Dispersion relation of the waveguide modes supported by the MIM structure depicted in Fig. 2.4 with gap size of $g = 5000$ nm and the corresponding electromagnetic field distributions at frequency $\omega = 0.08\omega_p$, which is indicated by the gray dashed line. The black dashed line denotes the light line in vacuum.

or antisymmetric SPP] all the other modes show a cut-off frequency at around $\omega_c = \frac{m\pi}{g}$, $m \in \{1, 2, 3, \dots\}$. The TE and TM modes are nearly degenerate in the frequency range which is far from the resonance frequencies of SPPs.

2.2 Gap Surface Plasmon Resonance

Let's now focus on the gap surface plasmon (GSP) modes, which originate from the G-SPP mode supported by MIM structures described by Eq. 2.15b. Substituting $k_1 = \sqrt{\beta_{\text{gsp}}^2 - \epsilon_m k_0^2}$ and $k_2 = \sqrt{\beta_{\text{gsp}}^2 - \epsilon_d k_0^2}$ into Eq. 2.15b yields [113, 115]

$$\tanh(\frac{g}{2}\sqrt{\beta_{\text{gsp}}^2 - \epsilon_d k_0^2}) = -\frac{\epsilon_d\sqrt{\beta_{\text{gsp}}^2 - \epsilon_m k_0^2}}{\epsilon_m\sqrt{\beta_{\text{gsp}}^2 - \epsilon_d k_0^2}}, \tag{2.18}$$

in which β_{gsp} is the propagation constant of G-SPP. By applying the approximation $\tanh(x) \approx x$ in the sufficiently small gap size limit, the propagation constant can

be expressed by [114]

$$\beta_{\mathrm{gsp}} \approx k_0 \sqrt{\epsilon_d + 0.5\left(\frac{\beta^0_{\mathrm{gsp}}}{k_0}\right)^2 + \sqrt{\left(\frac{\beta^0_{\mathrm{gsp}}}{k_0}\right)^2 \left[\epsilon_d - \epsilon_m + 0.25\left(\frac{\beta^0_{\mathrm{gsp}}}{k_0}\right)^2\right]}}, \quad (2.19)$$

with $\beta^0_{\mathrm{gsp}} = -\frac{2\epsilon_d}{g\epsilon_m}$, which denotes the propagation of G-SPP in the limit of $g \sim 0$.

For relatively larger gap sizes, by applying the approximation $\tanh(x) \approx 1 - 2\exp(-2x)$ one gets the following first-order corrected expression for the G-SPP propagation constant [114]:

$$\beta_{\mathrm{gsp}} \approx \beta_{\mathrm{spp}} \sqrt{1 - \frac{4\epsilon_d\epsilon_m}{\epsilon_m^2 - \epsilon_d^2}\exp\left(-\alpha_0 g\sqrt{1 + \frac{4\epsilon_m^2}{\epsilon_m^2 - \epsilon_d^2}\exp(-\alpha_0 g)}\right)}, \quad (2.20)$$

in which $\alpha_0 = \sqrt{\beta^2_{\mathrm{spp}} - \epsilon_d k_0^2} = \frac{k_0\epsilon_d}{\sqrt{-\epsilon_m - \epsilon_d}}$. One can get the approximate effective mode index $N_{\mathrm{eff}} = \beta_{\mathrm{gsp}}/k_0$ from Eqs. 2.19 and 2.20, which dramatically increases with a decreasing gap size.

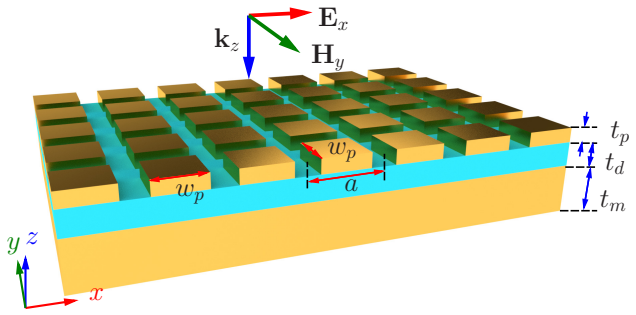

Figure 2.8: Geometry of a typical metal-insulator-metal plasmonic light absorber consisting of a periodic array of gold nanoparticles with width of $w_p = 190$ nm, thickness of $t_p = 30$ nm, and period of $a = 300$ nm, a continuous alumina spacer with thickness of $t_d = 15$ nm in the middle, and a gold reflector with thickness of $t_m = 80$ nm at the bottom.

Now we move to a similar MIM configuration as depicted in Fig. 2.4, but with a finite width of w along x direction. The G-SPP experiences an efficient reflection at the gap terminations due to its large mode index N_{eff}, thus larger Fresnel coefficients, for small gap sizes. The constructive interference of G-SPP and its reflection inside this MIM cavity leads to a resonance, namely GSP resonance. Taking into account the phase shift ϕ introduced by the reflection at the two terminations, the

resonant condition of this cavity can be expressed by [114]

$$w\frac{2\pi}{\lambda}N_{\text{eff}} = m\pi + \phi. \tag{2.21}$$

It is worth noting that this resonance due to constructive interference of G-SPP and its reflection by terminations, does not necessaryly require a finite size of structure as a whole. It is sufficient to have a finite gap size, which can be even defined by a finite size of metal particle as the top metal layer [17, 114, 116].

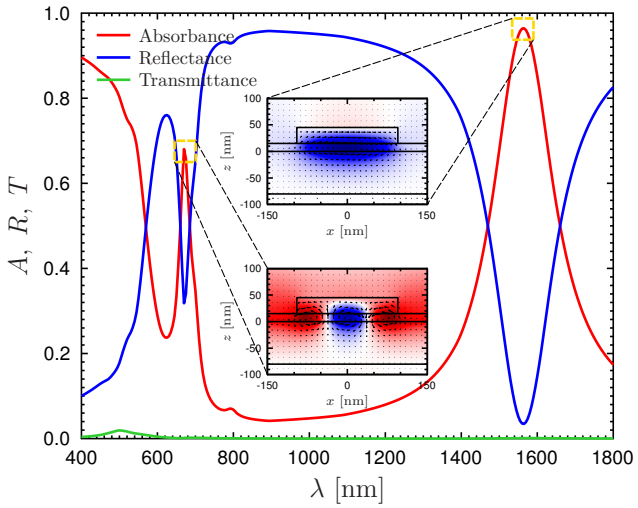

Figure 2.9: Reflectance, transmittance, absorbance, of the plasmonic light absorber as depicted in Fig. 2.8 for normal incidence light with TM polarization in x-z plane. The insets show the electromagnetic field distribution in x-z plane for the fundamental order and the 2nd order gap surface plasmon modes. The color map presents the y component of magnetic field and the arrow map presents x and z components of electric displacement field.

In Fig. 2.8 we show a typical kind of light absorber based on GSP resonator consisting of a 2D periodic array of square gold nanoparticles with width of w_p = 190 nm, thickness of t_p = 30 nm, period of a = 300 nm on top, an continuous alumina spacer of thickness t_d = 15 nm in the middle, and a continuous gold reflector of thickness t_m = 80 nm at the bottom. We numerically calculate the reflectance, transmittance, and absorbance at normal incidence using a FEM with experimentally measured optical constants of gold [117] and alumina [118].

Figure 2.9 shows that a GSP absorber, as depicted in Fig. 2.8, exhibits a near-perfect light absorption around 1550 nm and a slightly weaker absorption peak around 670 nm. The field distributions mapped in the insets of Fig. 2.9 indicate

that these two peaks in absorption correspond to the fundamental [first-order] and the second-order GSP resonance. It also shows the fundamental GSP resonance closely resembles a magnetic dipole resonance featuring enhanced magnetic field inside the dielectric gap. Inspired by Eq. 2.21, one can tune the resonance frequency by designing the width of the top particle.

In the light of GSP, people demonstrate a variety of GSP resonators operating at different frequency regimes ranging from visible to infrared for taming the electromagnetic response. A great amount of applications have been demonstrated during the last decade, including solar energy harvesting [21–24], thermal emitters [31–39], surface-enhanced Raman scattering [119–123], sensors [18, 25], modulators [124, 125], single photo emission [126], etc.

However, most of the applications mentioned above utilize the far-field absorption/emission properties of GSP resonators, the near-field RHT between two surfaces patterned with GSP resonators are still left unexplored. It can potentially provide us a spectrally tailorable heat flux and probably an enhancement in RHT.

2.3 Spoof Surface Plasmon Polaritons

The concept of SSPP is first proposed by J. B. Pendry *et al.* [127]. It describes surface modes supported on semi-infinite perfectly conducting surfaces perforated by holes in the infrared regime. It behaves as a counterpart of SPPs existing naturally on smooth nobel metal surfaces in visible/near-infrared regime. The surface waves originate from the waveguide modes supported by holes in perfect conductors [127, 128].

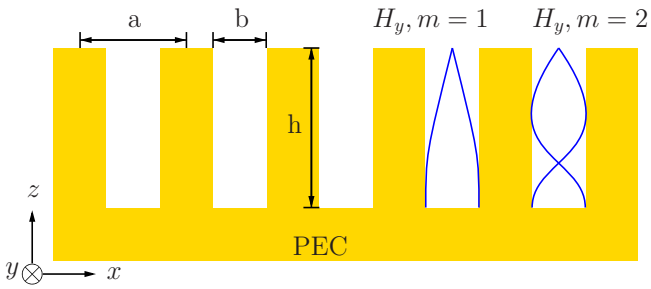

Figure 2.10: Geometry of a one-dimensional periodic array of metal grooves of width b, depth h, and period a.

Here we discuss the SSPP supported by a simple 1D structure, as depicted in Fig. 2.10. It consists of a periodic array of grooves with width of b, depth of h, and a period of a and a metal substrate. The period of the grooves is much smaller than the wavelength under consideration [$a \ll \lambda$]. Each groove can be treated as a hollow metallic waveguide [as discussed in section 2.1] in z direction truncated by

vacuum on top and metal at bottom. Due to its deep sub-wavelength nature, there only exists a fundamental TM mode $[H_y, E_x \neq 0]$. In the PEC approximation, the metal groove layer can be treated as a homogeneous layer of an anisotropic material with permittivity of $\epsilon_x = a/b$, $\epsilon_y = \epsilon_z = \infty$ and permeability of $\mu_x = 1$, $\mu_y = \mu_z = b/a$ [127, 128]. The reflection coefficient of this structure consisting of an anisotropic layer on top and a PEC layer at bottom can be written as [128]

$$r_{\text{groove}} = |r_{\text{groove}}|\mathrm{e}^{i\phi} = \frac{(\frac{a}{b}k_z - k_0) + (k_0 + \frac{a}{b}k_z)}{(\frac{a}{b}k_z + k_0) - (k_0 - \frac{a}{b}k_z)}, \tag{2.22}$$

in which ϕ is the phase of the reflected light. Setting the denominator of Eq. 2.22 to zero leads to the dispersion relation of SSPP modes:

$$\sqrt{\left(\frac{k_x}{k_0}\right)^2 - 1} = \frac{b}{a}\tan(k_0 h). \tag{2.23}$$

This expression can only predict the dispersion of SSPP modes in the limit of $\lambda > 4h$, in which all diffraction orders of the grooves can be safely neglected. At the resonance frequency the vacuum-groove interface can be approximately treated as a perfect magnetic conductor (PMC), where the reflected light gains zero phase shift. In contrast, the groove bottom acts as a PEC, which reflects light with a π-phase shift. Thus the resonance condition of this cavity can be described by

$$f_m = \frac{4c}{mh},\ m \in \{1, 3, 5, 7 \dots\}. \tag{2.24}$$

In Figs. 2.11(a) and 2.11(b) we plot the relation between real part of k_x and angular frequency ω for the structure depicted in Fig. 2.10 with $a = 500$ nm, $b = 100, 200, 300$ nm, and $h = 4.7$ μm using Eq. 2.23 and a FEM [see Section 3.3 of Chapter 3] using a Drude gold, respectively. Compared to the dispersion relation described by Eq. 2.23 for lossless PEC grooved plate, the k_x for the grooved plate with Drude gold does not go to infinity as ω approaching the resonance frequency, but folds back and crosses the light line eventually. It indicates that for Drude gold grooved plates the vacuum-groove interface and groove bottom cannot be simply treated as PMC and PEC, respectively. It leads to a non-π phase gained due to reflection for one round trip inside the cavity. Thus the resonance frequency deviates from that describe by Eq. 2.24.

Figure 2.12 shows the numerically calculated dispersion relation for Drude gold grooved plate with $b = 200$ nm, $a = 500$ nm and $h = 4700$ nm. The y component of magnetic field distribution H_y for the marked mode positions in Fig. 2.12 are mapped in Fig. 2.13. The non-zero H_y at $z = -0.5$ μm indicates the deviation of PMC approximation for vacuum-groove interface. As a result, the optical cavity length along z direction is slightly larger than the groove depth which gives rise to the slightly lower resonance frequencies than predicted by Eq. 2.23. The gold substrate still can be safely approximated as a PEC in the infrared regime, evidenced by the H_y fields reaching their maxima at groove bottoms.

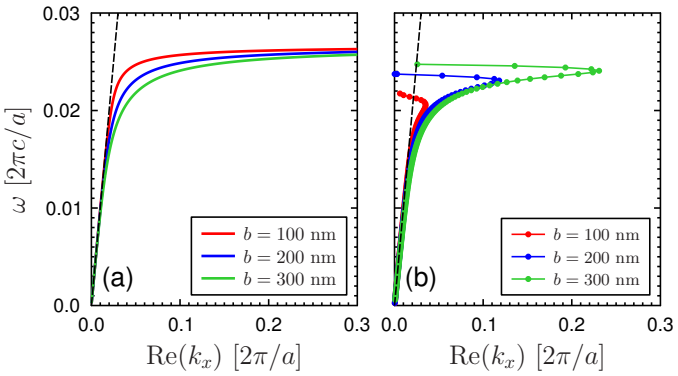

Figure 2.11: Dispersion relation of spoof surface plasmon polaritons supported by one-dimensional array of metal grooves depicted in Fig. 2.10. (a) the real part of k_x obtained by formula with perfect electric conductor approximation, and (b) numerically calculated k_x using a Drude model of gold.

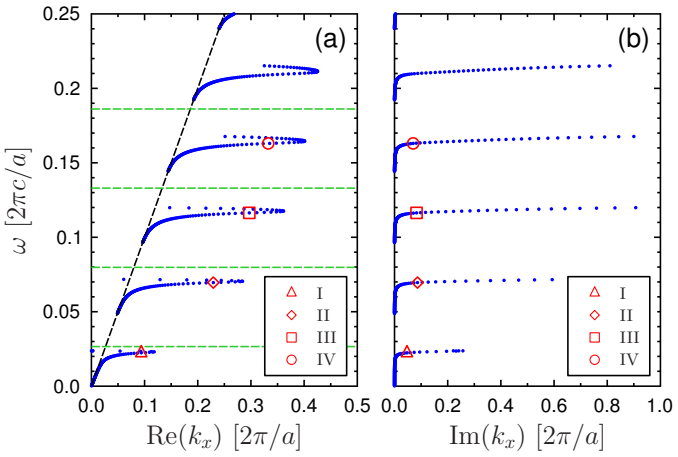

Figure 2.12: Numerically calculated dispersion relation of spoof surface plasmon polaritons supported by one-dimensional array of metal grooves depicted in Fig. 2.10. (a) and (b) present the real and imaginary part of β, respectively. The dashed green lines denote the resonance frequencies predicted by Eq. 2.24. The dashed black line denote the light line in vacuum. The markers denote the mode positions on the band diagram, whose corresponding field distributions are mapped in Fig. 2.13.

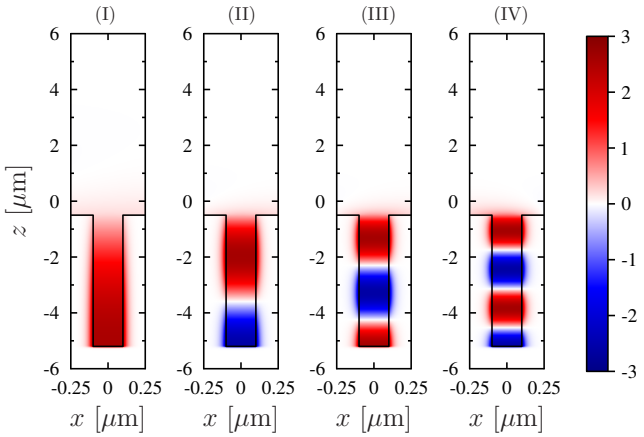

Figure 2.13: y component of magnetic fields in x-z plane corresponding to the mode positions marked in Fig. 2.12.

This grooved metal plate (GMP) structure supports the SSPP modes which have close resemblances to the SPP modes in the visible/near-infrared regime supported by a smooth plate of noble metals. Its resonance frequency can now be tailored to be in the infrared regime as it is determined by the geometrical size of grooves. It gives us the opportunities to tame the infrared electromagnetic response of metal plates by properly designing their surface geometries. This can be potentially used for engineering the near- and far-field thermal radiation/absorption of metal surfaces. Besides 1D GMP [129–135], 2D GMP [136], perfect conducting plates perforated by infinitely deep square [127, 137, 138] or circular holes [136–138], and some other structures [139, 140] have also been proved to support SSPP modes.

2.4 Hyperbolic Metamaterials

Metamaterials are artificial media consisting of sub-wavelength structures that exhibit exotic electromagnetic properties rarely possessed by nature materials. With the advances in nanofabrication techniques, utilizing metamaterials to manipulate electromagnetic response has been demonstrated for many attractive applications, including hyperlenses [41, 42] for super-resolution imaging, thermal emission property engineering [43, 58], enhanced RHT [56–58, 77, 85], spontaneous emission engineering [141–144], etc [23, 145]. Here, we provide a comprehensive understanding of a special type of metamaterials, namely hyperbolic metamaterials (HMMs) [146, 147], which are highly anisotropic with both positive and negative relative permittivities. The name hyperbolic comes from their hyperbolic disper-

sion. Here, we consider a nonmagnetic uniaxial material with optical axis along z direction. Thus, the relative permittivity tensor can be written in the following form:

$$\bar{\bar{\epsilon}} = \begin{bmatrix} \epsilon_\perp & 0 & 0 \\ 0 & \epsilon_\perp & 0 \\ 0 & 0 & \epsilon_\parallel \end{bmatrix}. \tag{2.25}$$

The subscript $\perp$ and $\parallel$ denote the components perpendicular and parallel to the optical axis, respectively. Substituting it into Eq. 2.2 and writing in matrix form yields:

$$\begin{bmatrix} {k_0}^2\epsilon_\perp - k_y^2 - k_z^2 & k_x k_y & k_x k_z \\ k_x k_y & {k_0}^2\epsilon_\perp - k_x^2 - k_z^2 & k_y k_z \\ k_x k_z & k_y k_z & {k_0}^2\epsilon_\parallel - k_x^2 - k_y^2 \end{bmatrix} \begin{bmatrix} E_x \\ E_y \\ E_z \end{bmatrix} = 0. \tag{2.26}$$

The solution of it gives the dispersion relation of this material:

$$\left(k_\perp^2 + k_\parallel^2 - \epsilon_\perp {k_0}^2\right)\left(\frac{k_\perp^2}{\epsilon_\parallel} + \frac{k_\parallel^2}{\epsilon_\perp} - {k_0}^2\right) = 0, \tag{2.27}$$

in which $k_\perp = \sqrt{k_x^2 + k_y^2}$ and $k_\parallel = k_z$ are the wavevector components along the direction perpendicular and parallel to the optical axis, respectively. Setting the first term of Eq. 2.27 to zeros leads to a spherical isofrequency surface in **k**-space, which describes the dispersion of this material under TE [electric field in a plane perpendicular to optical axis] excitation. Whereas, setting the second term of Eq. 2.27 to zero leads to an either ellipsoidal or hyperboloidal isofrequency surface depending on the sign of both $\epsilon_\parallel$ and $\epsilon_\perp$, which describes the dispersion of this material under TM [electric field in a plane parallel to the optical axis] excitation. When the signs are opposite, the material shows a hyperbolic dispersion, which is an open curve in contrast to ellipsoidal dispersion relations. As a result, electromagnetic wave with an arbitrarily large wavevector can still retain a propagating wave nature. Depending on the choice of signs of $\epsilon_\parallel$ and $\epsilon_\perp$, HMMs are categorized into two types: type I with $\epsilon_\parallel < 0$, $\epsilon_\perp > 0$, and type II with $\epsilon_\parallel > 0$, $\epsilon_\perp < 0$.

In order to realize a HMM, one has to design a metamaterial with a negative relative permittivity only in one or two spatial dimensions. In metals, free electrons move in the opposite direction to the electric field of the external excitation. As a consquence, metals have negative real part of relative permittivities below their plasmon frequency. By restricting the movement of free electrons in one or two directions, one or two positive relative permittivities can be achieved, thus a HMM. The most common way to realize a HMM is by a stack of deep subwavelength metal-dielectric bilayers structure as depicted in Fig. 2.14(a). A variety of choices of metal-dielectric bilayer materials as listed in Table. 2.1 [148], have been experimentally demonstrated to realize HMMs in the spectral range covering from ultraviolet to infrared.

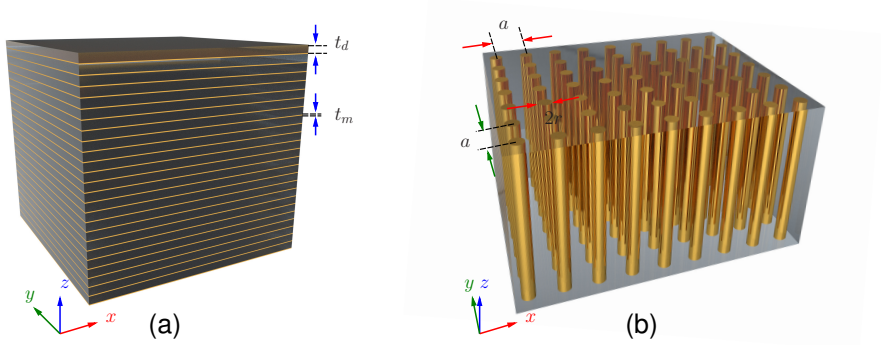

Figure 2.14: Geometry of (a) a multilayer and (b) a nanowire hyperbolic metamaterials.

When the metal-dielectric bilayer is of deep subwavelength thickness, the effective relative permittivity of the HMM can be evaluated by [165]:

$$\epsilon_\perp = f_m\epsilon_m + (1 - f_m)\epsilon_d, \tag{2.28a}$$

$$\epsilon_\parallel = \frac{\epsilon_m\epsilon_d}{\epsilon_d f_m + \epsilon_m(1 - f_m)}. \tag{2.28b}$$

Here, $f_m = t_m/(t_m + t_d)$ represents the volume filling ratio of metal in a period.

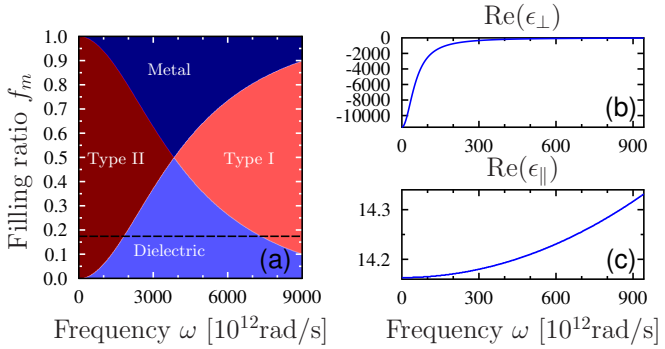

Figure 2.15: (a) Optical phase diagram of a Si/Au multilayer hyperbolic metamaterial. Real parts of (b) $\epsilon_\perp$, and (c) $\epsilon_\parallel$ of effective permittivities for the Si/Au multilayer system corresponding to the filling ratio f_m=20/(20+95) indicated by the dashed black line in (a).

Figure 2.15(a) presents the optical phase diagram of a Si/Au multilayer HMM.

Table 2.1: Material combinations for the fabrication of multilayer hyperbolic metamaterials.

Range	Material	Period (nm)	f	nr. of periods	Ref
UV	Ag/Al_2O_3	70	0.5	8	[149]
VIS	Au/Al_2O_3	38	0.5	8	[150–152]
	Au/Al_2O_3	40	0.5	8	[153]
	Au/Al_2O_3	43	0.35	10	[154]
	Au/TiO_2	48	0.33	4	[155]
	Au/PMMA	55	0.45	10	[156]
	Au/Si	10	0.6	10	[157]
	Ag/LiF	75	0.4	8	[156]
	Ag/MgF_2	50	0.4	8	[156]
	Ag/MgF_2	60	0.42	7	[158]
	Ag/TiO_2	31	0.29	5	[159]
	Ag/Ti_3O_5	60	0.5	9	[160]
	Ag/SiO_2	30	0.5	3	[161]
	Ag/Si	20	0.5	15	[141]
IR	AlInAs/InGaAs	160	0.5	50	[162]
	Al:ZnO/ZnO	120	0.5	50	[163]
	Ag/Ge	50	0.4	3	[164]

At different frequencies and filling ratios, the multilayer metal-dielectric bilayer structure can not only behave as a type-I or type-II HMM but also as an effective metal or dielectric material. Figure 2.15(b) and 2.15(c) show the corresponding $\epsilon_\perp$ and $\epsilon_\parallel$ for $f_m = 20/(20+95)$, which is used for the enhanced near-field RHT later in Chapter 4. It behaves as a type-II HMM, a metal for polarization with electric field in a plane parallel to the optical axis and a dielectric for electric field in a plane perpendicular to the optical axis, in the frequency range up to $\omega \sim 1800\times10^{12}$ rad/s.

Another way to realize a HMM is using nanowire arrays consisting of plasmonic or phonon-polaritonic metals embedded in a dielectric matrix [see Fig. 2.14(b)] [77, 85]. With optical axis along z direction, the effective relative permittivities are determined by [166, 167]

$$\epsilon_\perp = \frac{(1+f_m)\epsilon_m + (1-f_m)\epsilon_d}{(1-f_m)\epsilon_m + (1+f_m)\epsilon_d}, \tag{2.29a}$$

$$\epsilon_\parallel = f_m\epsilon_m + (1-f_m)\epsilon_d. \tag{2.29b}$$

Such nanowire arrays are typically realized by fabricating porous matrices with dielectrics or semiconductors via anodic electrochemical etching, followed by metal filling through electrochemical deposition [168–173].

There are a few more alternative ways to realize a HMM, including a hybrid structure consisting of nanolayered metal-dielectric tapered gratings [23, 145] or

pyramid arrays [24, 164]. It is worth noting that the hyperbolic dispersion does possess by nature materials. For example, triglycine sulphate [low-terahertz], sapphire [mid-infrared], and pyrolytic graphite [ultraviolet] behave as HMMs in a certain frequency ranges [174].

The effective medium description of HMMs can reduce the computing power and simplify the process for designing a HMM with a desired electromagnetic response. However, it cannot always precisely predict its properties especially when there are SPPs or near-field interaction involved. The nonlocal effects, i.e., the permittivity components are not only functions of the frequency but also functions of the wavevector, have to be taken into consideration [175, 176]. Therefore a rigorous numerical simulation of HMM is important for such cases [177, 178].

Chapter 3

Numerical Methods

When two or many bodies at different temperatures are brought closely enough to each other, comparable to the corresponding thermal wavelength, the radiative energy transfered can exceed the far-field limit predicted by Planck's law. The first experimental observation of this anomalous radiative heat transfer (RHT) can date back to 1969 between two metal plates separated by a micrometer-gap [48]. Two years later D. Polder and M. van Hove published the seminal paper to clarify the role of photon tunneling through evanescent waves in this anomalous phenomenon [47]. In this chapter, we provide several numerical techniques needed for computing near-field RHT between closely spaced planar structures and understanding the underlying physical mechanisms. Starting with the simplest homogeneous layered structure, we solve the stochastic Maxwell's equations using dyadic Green's functions and give the final expression for calculating RHT in terms of reflection coefficients which one can get by different scattering approaches. And then we extend the method to manage 1D/2D periodic structures by introducing RCWA. We also briefly introduce an alternative finite-difference time-domain (FDTD) method based on a Langevin approach, which can also calculate RHT between periodic nanostructured bodies. At last, we present a complex wavenumber eigenvalue simulation (CWES) approach, which we used to solve the dispersion relation and analyze the mode profile through the entire thesis.

3.1 Dyadic Green's Function Picture of Radiative Heat Transfer

Thermal radiation comes from the random motion of the constituents of matter, i.e., electrons, atoms or ions, under thermal agitation, which can be described by a stochastic current density $\mathbf{j}^{\mathbf{f}}$. One can get the electromagnetic field excited by this

thermally induced current by solving the stochastic Maxwell's equations

$$\mathbf{E}(\mathbf{r},\omega) = i\mu_0\omega \int_V \overline{\overline{\mathbf{G}}}^{E}(\mathbf{r},\mathbf{r}',\omega)\mathbf{j}^{\mathbf{f}}(\mathbf{r}',\omega), \tag{3.1a}$$

$$\mathbf{H}(\mathbf{r},\omega) = \int_V \overline{\overline{\mathbf{G}}}^{H}(\mathbf{r},\mathbf{r}',\omega)\mathbf{j}^{\mathbf{f}}(\mathbf{r}',\omega), \tag{3.1b}$$

using a dyadic Green's function formalism. Here, $\mathbf{j}^{\mathbf{f}}(\mathbf{r}',\omega)$ represents the fluctuating current density at point $\mathbf{r}'$. The terms $\overline{\overline{\mathbf{G}}}^{E}$ and $\overline{\overline{\mathbf{G}}}^{H}$ respectively denote the electric and magnetic dyadic Green's functions, which link the electromagnetic field at point $\mathbf{r}$ with the thermally induced current at $\mathbf{r}'$. In Cartesian coordinates, the spectral distribution of radiative heat flux at location z_c can be expressed by the ensemble average of Poynting vector along z direction, which can be written in the following form:

$$q(\omega, z_c) = \langle S_z(z_c,\omega)\rangle = 4 \times \frac{1}{2}\,\mathrm{Re}\left\{\left\langle E_x H_y^{\dagger} - E_y H_x^{\dagger}\right\rangle\right\}. \tag{3.2}$$

According to fluctuation-dissipation theorem, for fluctuating current density $\mathbf{j}^{\mathbf{f}}$ at two distinct spatial coordiantes $\mathbf{r}'$ and $\mathbf{r}''$ in an isotropic homogeneous medium, the ensemble average can be expressed by [179–181]

$$\langle \mathbf{j}^{r}_{\alpha}(\mathbf{r}',\omega)\mathbf{j}^{r}_{\alpha'}(\mathbf{r}'',\omega')\rangle = \frac{\omega\epsilon_0\epsilon_r''(\omega)}{\pi}\Theta(\omega,T)\delta(\mathbf{r}'-\mathbf{r}'')\delta(\omega-\omega')\delta_{\alpha\alpha'}, \tag{3.3}$$

in which $\Theta(\omega,T) = \hbar\omega/\exp\left[(\hbar\omega/k_BT)-1\right]$ is the mean energy of a Planck's oscillator in thermal equilibrium at angular frequency ω and temperature T, ϵ_r'' the imaginary part of relative permittivity of the emitting medium, δ the Dirac function, and $\delta_{\alpha\alpha'}$ the Kronecker delta function, which is a consequence of isotropy. Substitution of Eq. 3.1 and Eq. 3.3 into Eq. 3.2 yields

$$\begin{aligned} q(\omega, z_c) =& \frac{2{k_0}^2\Theta(\omega,T)}{\pi} \\ & \mathrm{Re}\left\{ i\epsilon_r''(\omega)\int_V \mathrm{d}V' \left[G^{E}_{x\alpha}(\mathbf{r},\mathbf{r}',\omega)G^{H\dagger}_{y\alpha}(\mathbf{r},\mathbf{r}') - G^{E}_{y\alpha}(\mathbf{r},\mathbf{r}',\omega)G^{H\dagger}_{x\alpha}(\mathbf{r},\mathbf{r}')\right]\right\}. \end{aligned} \tag{3.4}$$

The dyadic Green's function can be represented by plane waves in terms of electric and magnetic Weyl components g^E and g^H. Thus the heat flux $q(z_c)$ along z direction at coordinate $z = z_c$ inside the receiver layer Z_c, due to a source layer Z_s of temperature T, in cylindrical coordinates can be written as

$$\begin{aligned} q(\omega, z_c) =& \frac{2{k_0}^2\Theta(\omega,T)}{\pi} \\ & \mathrm{Re}\left\{ i\epsilon_{rs}''(\omega)\int_0^{\infty}\beta\mathrm{d}\beta\int_{Z_s}\mathrm{d}z' \begin{bmatrix} & g^{E}_{sc\beta\alpha}(\beta,z_c,z',\omega)g^{H\dagger}_{sc\phi\alpha}(\beta,z_c,z',\omega) \\ - & g^{E}_{sc\phi\alpha}(\beta,z_c,z',\omega)g^{H\dagger}_{sc\beta\alpha}(\beta,z_c,z',\omega)\end{bmatrix}\right\}, \end{aligned} \tag{3.5}$$

in which $\beta = \sqrt{k_x^2 + k_y^2}$ represents the surface-parallel wavevector. The net heat flux absorbed by the layer Z_c can then be calculated by the difference between fluxes at the top- and bottom-surface of the receiver medium.

The heat flux between two homogeneous isotropic or uniaxial (with optical axis z direction) stratified media can be casted into the form

$$q = \frac{1}{2\pi}\int_0^\infty \Theta_{12}(\omega, T_1, T_2)\mathrm{d}\omega \frac{1}{2\pi}\int_0^\infty \sum_{j=s,p} \mathcal{T}_j(\omega, \beta, \phi)\beta \mathrm{d}\beta, \tag{3.6}$$

and between two anisotropic stratified media in the form of

$$q = \frac{1}{2\pi}\int_0^\infty \Theta_{12}(\omega, T_1, T_2)\mathrm{d}\omega \frac{1}{(2\pi)^2}\int_{-\infty}^\infty\int_{-\infty}^\infty \sum_{j=s,p} \mathcal{T}_j(\omega, k_x, k_y)\mathrm{d}k_x\mathrm{d}k_y. \tag{3.7}$$

Here $\mathcal{T}_j$ is the transmission factor which describes the probability of one thermally excited photon of either s or p polarization with surface-parallel wavevector (k_x, k_y) or (β, ϕ) transferring from one plate to the other. The transmission factor can be further calculated by

$$\sum_{j=s,p} \mathcal{T}_j(\omega, \beta) = \begin{cases} \mathrm{Tr}\left[(\mathbb{I} - \mathbf{R}_2^\dagger\mathbf{R}_2 - \mathbf{T}_2^\dagger\mathbf{T}_2)D_{12}(\mathbb{I} - \mathbf{R}_1^\dagger\mathbf{R}_1 - \mathbf{T}_1^\dagger\mathbf{T}_1)D_{12}^\dagger\right], & \beta < k_0 \\ \mathrm{Tr}\left[(\mathbf{R}_2^\dagger - \mathbf{R}_2)D_{12}(\mathbf{R}_1 - \mathbf{R}_1^\dagger)D_{12}^\dagger\right]\mathrm{e}^{-2|k_{z0}g|}, & \beta > k_0 \end{cases} \tag{3.8}$$

in which $D_{12} = [\mathbb{I} - \mathbf{R}_1\mathbf{R}_2\mathrm{e}^{i2k_{z0}g}]^{-1}$ is a Fabry-Pérot-like denominator describing the interference in the vacuum between two media, $\mathbb{I}$ the identity matrix, and $k_{z0} = \sqrt{{k_0}^2 - \beta^2}$ the z component of wavevector in the vacuum gap. And $\mathbf{R}$ is the reflection matrix defined by:

$$\mathbf{R}_i = \begin{bmatrix} r_i^{s,s}(\omega, k_x, k_y) & r_i^{s,p}(\omega, k_x, k_y) \\ r_i^{p,s}(\omega, k_x, k_y) & r_i^{p,p}(\omega, k_x, k_y) \end{bmatrix}, \tag{3.9}$$

$\mathbf{T}$ the transmission matrix defined by:

$$\mathbf{T}_i = \begin{bmatrix} t_i^{s,s}(\omega, k_x, k_y) & t_i^{s,p}(\omega, k_x, k_y) \\ t_i^{p,s}(\omega, k_x, k_y) & t_i^{p,p}(\omega, k_x, k_y) \end{bmatrix}, \tag{3.10}$$

in which r_i^{ss}, r_i^{pp} (t_i^{ss}, t_i^{pp}) represent the reflection (transmission) coefficients of a plate under s- and p-polarized incident light. $r_i^{s,p(p,s)}$ ($t_i^{s,p(p,s)}$) denotes the cross-polarization reflection (transmission) coefficient. One can get the contributions of s- and p-polarization separately by considering top-left and bottom-right quadrants of the matrix terms inside the rectangular bracket in Eq. 3.8, respectively.

The expression for transmission factor between two stratified media given in Eq. 3.8 is derived from Eq. 3.5 by using appropriate Weyl components and a scattering matrix method [182]. For homogeneous isotropic stratified structures, the

reflection matrices can be calculated by using a standard scattering matrix approach when many layers are involved. For simple semi-infinite plates, it will reduce to the Fresnel coefficients at the plate-vacuum interface. For homogeneous anisotropic stratified structures, one should use a 4-by-4 scattering matrix method instead of a 2-by-2 scattering matrix method used for isotropic stratified structures or anisotropic Fresnel coefficients for semi-infinite plates.

We define the integrated transmission factor as

$$\begin{aligned}\Phi(\omega) &= \frac{1}{4\pi^2}\sum_{j=s,p}\int_0^{2\pi}\int_0^{\infty}\beta\mathcal{T}_j(\omega,\beta,\phi)\mathrm{d}\beta\mathrm{d}\phi \\ &= \frac{1}{4\pi^2}\sum_{j=s,p}\int_{-\infty}^{+\infty}\int_{-\infty}^{+\infty}\mathcal{T}_j(\omega,k_x,k_y)\mathrm{d}k_x\mathrm{d}k_y,\end{aligned} \tag{3.11}$$

which describes the flux of transmission factor in the unit of $[\mathrm{m}^{-2}]$. For blackbodies, the transmission factor is 1 for both s- and p- polarized photons at any frequencies and wavevectors inside the light cone, which indicates that only propagating waves are considered. The integrated transmission factor between two blackbodies is the following:

$$\Phi_{BB} = \frac{\omega^2}{2\pi {c_0}^2}. \tag{3.12}$$

And one can easily get the heat flux between two blackbodies at different temperatures in the following form

$$q_{\mathrm{BB}}(T_1,T_2) = \frac{1}{2\pi}\int_0^{\infty}\Theta(\omega,T_1,T_2)\Phi_{\mathrm{BB}}\mathrm{d}\omega = \delta_{BB}(T_1^4 - T_2^4), \tag{3.13}$$

which recovers the Setefan-Boltzmann law. And $\delta_{BB} = 5.670367\times10^{-8}\mathrm{Wm}^{-2}\mathrm{K}^{-4}$ is the Stefan-Boltzmann constant.

3.2 Radiative Heat Transfer between Periodic Nanostructures

In homogeneous stratified medium, the dyadic Green's function is calculated by 2-by-2 or 4-by-4 scattering matrix. In this section, we introduce two different numerical techniques used for calculating the dyadic Green's function for 1D/2D periodic metamaterials with square or rectangular lattices. The first method uses the RCWA [183–192], which expands the electromagnetic and the spatial distribution of permittivity into Fourier series, to calculate the reflection and transmission matrices [78, 79, 193–196]. The second one uses the FDTD method incorporating with a Langevin approach [197, 198] to solve for the Green's function.

3.2.1 Rigorous Coupled-Wave Analysis Approach

We start with writing two curl equations of Maxwell equation in the following form

$$\frac{\partial E_z}{\partial y} - \frac{\partial E_y}{\partial z} = ik_0\mu_r\widetilde{H}_x, \tag{3.14a}$$
$$\frac{\partial E_x}{\partial z} - \frac{\partial E_z}{\partial x} = ik_0\mu_r\widetilde{H}_y, \tag{3.14b}$$
$$\frac{\partial E_y}{\partial x} - \frac{\partial E_x}{\partial y} = ik_0\mu_r\widetilde{H}_z, \tag{3.14c}$$
$$\frac{\partial \widetilde{H}_z}{\partial y} - \frac{\partial \widetilde{H}_y}{\partial z} = -ik_0\epsilon_r E_x, \tag{3.14d}$$
$$\frac{\partial \widetilde{H}_x}{\partial z} - \frac{\partial \widetilde{H}_z}{\partial x} = -ik_0\epsilon_r E_y, \tag{3.14e}$$
$$\frac{\partial \widetilde{H}_y}{\partial zx} - \frac{\partial \widetilde{H}_x}{\partial y} = -ik_0\epsilon_r E_z, \tag{3.14f}$$

in which we normalize the magnetic field according to $\widetilde{\mathbf{H}} = \sqrt{\frac{\mu_0}{\epsilon_0}}\mathbf{H}$. The materials considered in the thesis are nonmagnetic, i.e., $\mu_r = 1$. The 2D periodical spatial distribution plane of relative permittivity in x-y plane can be written by the summation of Fourier components along x and y directions

$$\epsilon_r = \sum_{m=-\infty}^{\infty}\sum_{n=-\infty}^{\infty} a_{m,n}\mathrm{e}^{-i\left(\frac{2\pi m}{\Lambda_x}x+\frac{2\pi n}{\Lambda_y}y\right)} \tag{3.15}$$

It follows that the Fourier expansion of electric and magnetic fields are

$$\begin{bmatrix}E_x(x,y,z)\\E_y(x,y,z)\\E_z(x,y,z)\end{bmatrix} = \sum_{m=-\infty}^{\infty}\sum_{n=-\infty}^{\infty}\begin{bmatrix}\mathcal{E}_x(x,y,z)\\\mathcal{E}_x(x,y,z)\\\mathcal{E}_x(x,y,z)\end{bmatrix}\mathrm{e}^{i[k_{x,\mathrm{inc}}-\frac{2\pi m}{\Lambda_x}x+k_{y,\mathrm{inc}}-\frac{2\pi n}{\Lambda_y}y]}, \tag{3.16a}$$

$$\begin{bmatrix}\widetilde{H}_x(x,y,z)\\\widetilde{H}_y(x,y,z)\\\widetilde{H}_z(x,y,z)\end{bmatrix} = \sum_{m=-\infty}^{\infty}\sum_{n=-\infty}^{\infty}\begin{bmatrix}\widetilde{\mathcal{H}}_x(x,y,z)\\\widetilde{\mathcal{H}}_y(x,y,z)\\\widetilde{\mathcal{H}}_z(x,y,z)\end{bmatrix}\mathrm{e}^{i[k_{x,\mathrm{inc}}-\frac{2\pi m}{\Lambda_x}x+k_{y,\mathrm{inc}}-\frac{2\pi n}{\Lambda_y}y]}, \tag{3.16b}$$

respectively. The subscript "inc" denotes the incident wavevector. Substituting Eqs. 3.16 and 3.15 into Eqs. 3.14 yields the following matrix form of curl equations

$$\partial_z\mathcal{E} = \begin{bmatrix}i\mathbf{K}_x[\![\epsilon]\!]_{xy}^{-1}\mathbf{K}_y & \mathbb{I}-i\mathbf{K}_x[\![\epsilon]\!]_{xy}^{-1}\mathbf{K}_x\\ i\mathbf{K}_y[\![\epsilon]\!]_{xy}^{-1}\mathbf{K}_y-i\mathbb{I} & -i\mathbf{K}_y[\![\epsilon]\!]_{xy}^{-1}\mathbf{K}_x\end{bmatrix}\widetilde{\mathcal{H}} = \mathbb{P}\widetilde{\mathcal{H}}, \tag{3.17a}$$

$$\partial_z\widetilde{\mathcal{H}} = \begin{bmatrix}-i\mathbf{K}_x\mathbf{K}_y & -i[\![\epsilon]\!]_x^y+i\mathbf{K}_x\mathbf{K}_x\\ -i\mathbf{K}_y\mathbf{K}_y+i[\![\epsilon]\!]_y^x & i\mathbf{K}_y\mathbf{K}_x\end{bmatrix}\mathcal{E} = \mathbb{Q}\mathcal{E}, \tag{3.17b}$$

in which $\mathbf{K}_x$ and $\mathbf{K}_y$ are $(2\times M+1)\times(2\times N+1)$ diagonal matrices with elements present by

$$\mathcal{K}_x = \frac{k_{x,\mathrm{inc}}}{k_0} - \frac{2\pi m}{k_0\Lambda_x},\ m\in\{-M,\ldots,-2,-1,0,1,2,\ldots,M\}, \tag{3.18}$$

$$\mathcal{K}_y = \frac{k_{y,\mathrm{inc}}}{k_0} - \frac{2\pi n}{k_0\Lambda_y},\ n\in\{-N,\ldots,-2,-1,0,1,2,\ldots,N\}. \tag{3.19}$$

Here, we normalize all the wavevectors to k_0. $[\![\epsilon]\!]$ is the Toeplitz matrix of the spatial distribution of dielectric function. It is worth noting that in Eq. 3.17 we have applied Li's factorization rule [199], i.e., for $\mathbb{P}$ matrix

$$[\![\epsilon]\!]_{xy} = \left[\!\!\left[\frac{1}{\Lambda_x\Lambda_y}\int_0^{\Lambda_y}\int_0^{\Lambda_x} \mathrm{d}x\mathrm{d}y \mathrm{e}^{-i(\mathcal{K}_x-\mathcal{K}'_x)x-i(\mathcal{K}_y-\mathcal{K}'_y)y}\epsilon(x,y)\right]\!\!\right], \tag{3.20}$$

with Laurent's rule in both directions and for $\mathbb{Q}$ matrix with inverse rule in one direction, Laurent's rule in the other direction:

$$[\![\epsilon]\!]_x^y = \left[\!\!\left[\frac{1}{\Lambda_y}\int_0^{\Lambda_y} \mathrm{d}y \mathrm{e}^{-i(\mathcal{K}_y-\mathcal{K}'_y)y} \left[\!\!\left[\frac{1}{\Lambda_x}\int_0^{\Lambda_x}\mathrm{d}x\mathrm{e}^{-i(\mathcal{K}_x-\mathcal{K}'_x)x}\frac{1}{\epsilon(x,y)}\right]\!\!\right]^{-1}(y)\right]\!\!\right], \tag{3.21a}$$

$$[\![\epsilon]\!]_y^x = \left[\!\!\left[\frac{1}{\Lambda_x}\int_0^{\Lambda_x} \mathrm{d}x \mathrm{e}^{-i(\mathcal{K}_x-\mathcal{K}'_x)x} \left[\!\!\left[\frac{1}{\Lambda_y}\int_0^{\Lambda_y}\mathrm{d}y\mathrm{e}^{-i(\mathcal{K}_y-\mathcal{K}'_y)y}\frac{1}{\epsilon(x,y)}\right]\!\!\right]^{-1}(x)\right]\!\!\right], \tag{3.21b}$$

to decrease the Gibbs phenomenon for high dielectric contrast structures. Solving the wave equation corresponding to Eqs. 3.17

$$\partial_z^2\mathcal{E} = \mathbb{P}\mathbb{Q}\mathcal{E} = \mathcal{W}\mathbb{LAM}^2\mathcal{W}, \tag{3.22}$$

we can get the egienvector $\mathcal{W}$, and eigenvalues $\mathbb{LAM}^2$ of the periodically structured layer by

$$[\mathcal{W},\mathbb{LAM}^2] = \mathrm{eig}(\mathbb{PQ}). \tag{3.23}$$

Thus, one can express the electromagnetic field at z along z direction with respect to the bottom surface of the periodically structured layer as

$$\mathcal{E}(z) = \mathbb{P}(\mathrm{e}^{\mathbb{LAM}z}\mathcal{C}^+ + \mathbb{P}\mathrm{e}^{-\mathbb{LAM}z}\mathcal{C}^-), \tag{3.24a}$$

$$\mathcal{H}(z) = \mathbb{V}(\mathrm{e}^{\mathbb{LAM}z}\mathcal{C}^+ - \mathbb{P}\mathrm{e}^{-\mathbb{LAM}z}\mathcal{C}^-), \tag{3.24b}$$

in which $\mathbb{V} = \mathbb{P}^{-1}\mathcal{W}\mathbb{LAM}$, and $\mathcal{C}^\pm$ are column vectors containing the amplitude coefficient of each mode. By applying boundary conditions at each interface incorporating with a scattering approach, one can get the scattering matrix

$$\begin{bmatrix}\mathcal{R}\\ \mathcal{T}\end{bmatrix} = \begin{bmatrix}S_{11} & S_{12}\\ S_{21} & S_{22}\end{bmatrix}\begin{bmatrix}\mathcal{I}^+\\ \mathcal{I}^-\end{bmatrix} \tag{3.25}$$

for the periodic nanostructures, which connects the incident field with reflected and transmitted fields. $S_{11} = \mathbf{R}$ and $S_{21} = \mathbf{T}$ are the reflection and transmission matrices, respectively. And S_{12} and S_{22} are the backward reflection and transmission matrices, respectively. If the nanostructured plates are semi-infinite or thick enough to stop all light from transmission, we can safely set $\mathbf{T} = \mathbf{0}$, and the expression for transmission factor similar as Eq. 3.8 can be casted in the following matrix form:

$$\sum_{j=s,p} \mathcal{T}_j(\omega, k_x, k_y) = \mathrm{Tr}(\mathbb{D}\mathbb{W}_1\mathbb{D}^\dagger\mathbb{W}_2), \tag{3.26a}$$

$$\mathbb{D} = (\mathbb{I} - \mathbf{S}_1\mathbf{S}_2)^{-1}, \tag{3.26b}$$

$$\mathbb{W}_1 = \sum_{-1}^{\mathrm{pw}} -\mathbf{S}_1 \sum_{-1}^{\mathrm{pw}} \mathbf{S}_1^\dagger + \mathbf{S}_1 \sum_{-1}^{\mathrm{ew}} - \sum_{-1}^{\mathrm{ew}} \mathbf{S}_1^\dagger, \tag{3.26c}$$

$$\mathbb{W}_2 = \sum_{1}^{\mathrm{pw}} -\mathbf{S}_2^\dagger \sum_{1}^{\mathrm{pw}} \mathbf{S}_2 + \mathbf{S}_2^\dagger \sum_{1}^{\mathrm{ew}} - \sum_{1}^{\mathrm{ew}} \mathbf{S}_2, \tag{3.26d}$$

$$\mathbf{S}_1 = \mathbf{R}_1(\omega, k_x, k_y), \tag{3.26e}$$

$$\mathbf{S}_2 = \mathrm{e}^{i\mathbb{K}_z g}\mathbf{R}_2(\omega, k_x, k_y)e^{i\mathbb{K}_z g}. \tag{3.26f}$$

The operators $\sum_{n=\pm1}^{\mathrm{pw/ew}} = \mathbb{K}_z^n \prod^{\mathrm{pw/ew}}$ are defined as [79]

$$\prod_{\alpha\alpha'}^{\mathrm{pw}} = \frac{1}{2}\delta_{\alpha\alpha'}\left[\mathbb{I} + \mathrm{sgn}(\mathbb{K}_z^2)\right], \tag{3.27}$$

$$\prod_{\alpha\alpha'}^{\mathrm{ew}} = \frac{1}{2}\delta_{\alpha\alpha'}\left[\mathbb{I} - \mathrm{sgn}(\mathbb{K}_z^2)\right], \tag{3.28}$$

which are projection operators to identify propagating and evanescent waves. The $\mathbb{K}_z$ is constructed by

$$\begin{bmatrix} \mathbf{K}_z & \mathbf{0} \\ \mathbf{0} & \mathbf{K}_z \end{bmatrix}, \tag{3.29}$$

with dimensionality of $4 \times (2 \times M + 1) \times (2 \times N + 1)$ and $\mathbf{K}_z = \sqrt{\mathbb{I} - \mathbf{K}_x - \mathbf{K}_x}$. For 2D periodic structure one can get the integrated transmission factor $\Phi(\omega)$ by integrating over the first Brillouin zone

$$\Phi(\omega) = \frac{1}{4\pi^2} \sum_{j=s,p} \int_{-\frac{\pi}{a_y}}^{+\frac{\pi}{a_y}} \int_{-\frac{\pi}{a_x}}^{+\frac{\pi}{a_x}} \mathcal{T}_j(\omega, k_x, k_y)\mathrm{d}k_x\mathrm{d}k_y. \tag{3.30}$$

3.2.2 FDTD Approach

From Eq. 3.4, we know that in order to get the heat flux along z direction, we need to calculate the Green's function which connects the electromagnetic fields in receiver

plane with all the fluctuations in the emitting layer. The most straightforward and naive way to do so is to put dipoles with different polarizations and wavevectors in the emitting layer and check the resulting electromagnetic fields in the receiver plane using FDTD. However, there will be a large number of simulations due to the richness in combinations of wavevectors and spatial coordinates. In order to overcome this obstacle, one can use FDTD incorporating a Langevin approach, which adds a random force term $\mathbf{K}(t)$, representing the thermal fluctuations, to the harmonic response of polarizability $\mathbf{P}$ to a local electric field $\mathbf{E}$. The time harmonic equation then expresses as:

$$\frac{\mathrm{d}^2\mathbf{P}}{\mathrm{d}t^2} + \gamma\frac{\mathrm{d}\mathbf{P}}{\mathrm{d}t} + \omega_0^2\mathbf{P} = \sigma\mathbf{E} + \mathbf{K}(t). \tag{3.31}$$

Here, γ is the collision frequency expressing the loss of material, and ω_0 is the resonance frequency of the polarization system, which is 0 for Drude metals. The random force term has to satisfy the fluctuation dissipation theorem. Then one can get the correlation function of $\mathbf{K}$ with detailed expression in Ref. [197]. Due to the randomly generated fluctuation terms, one has to take ensemble average over many times of repeated simulations and use enough number of time steps. This method takes much longer time and more computing resources compared to RCWA based method. Additionally, it sometimes gives slightly overestimated transmission factors, i.e., $\mathcal{T}_j(\omega, k_x, k_y) > 1$. To get a better convergence, even larger number of repeated simulations may be needed.

3.3 Complex k Band Diagram Calculation

The numerical simulation of photonic band diagram is an important tool for analyzing the origins and properties of different types of modes supported by metamaterials. Thus, one can engineer the band structures to achieve a desired function. In this section, we introduce a complex wavenumber eigenvalue simulation (CWES), which uses a real frequency as an input and gives complex wavevectors, used for calculating photonic band diagram throughout this thesis. Another sign convention with $\mathrm{e}^{i\omega t}$ has been used in this section.

To begin with, we start with the wave equation of magnetic field $\mathbf{H}$:

$$\nabla \times \left(\frac{1}{\epsilon}\nabla \times \mathbf{H}\right) - \mu\frac{\omega^2}{{c_0}^2}\mathbf{H} = 0. \tag{3.32}$$

For periodic metamaterials, we can apply Bloch periodic boundary conditions to the electromagnetic field in the periodic structure according to Bloch's theorem . Thus the magnetic field reads as:

$$\mathbf{H}(\mathbf{r}) = \mathbf{u}(\mathbf{r})\exp[i(\omega t - \mathbf{k}\cdot\mathbf{r})], \tag{3.33}$$

in which $\mathbf{k}$ is the Bloch wavevector, ω the angular frequency of the electromagnetic field, and $\mathbf{u}(\mathbf{r})$ a vector function which describes the spatial distribution of magnetic

field of the corresponding mode. Substitution of Eq. 3.33 into Eq. 3.32 yields

$$\frac{k^2}{\epsilon} - \frac{\mathbf{k}}{\epsilon}(\mathbf{k}\cdot\mathbf{u}) - i\mathbf{k}\times\left(\frac{1}{\epsilon}\nabla\times\mathbf{u}\right) - i\nabla\times\left(\frac{1}{\epsilon}\mathbf{k}\times\mathbf{u}\right) + \nabla\times\left(\frac{1}{\epsilon}\times\mathbf{u}\right) - \mu\frac{\omega^2}{{c_0}^2} = 0, \tag{3.34}$$

which can be treated as the eigenvalue problem solving for Bloch wavevector $\mathbf{k}$. This equation can be solved through the following weak form

$$\begin{aligned} F_H(\mathbf{v},\mathbf{u}) = {} & \frac{k^2}{\epsilon}\mathbf{v}\cdot\mathbf{u} - \frac{1}{\epsilon}(\mathbf{k}\cdot\mathbf{v})(\mathbf{k}\cdot\mathbf{u}) - i\frac{1}{\epsilon}\mathbf{v}\cdot[\mathbf{k}\times(\nabla\times\mathbf{u})] \\ & - i(\nabla\times\mathbf{v})\cdot\frac{1}{\epsilon}(\mathbf{k}\times\mathbf{u}) + (\nabla\times\mathbf{v})\cdot\frac{1}{\epsilon}(\nabla\times\mathbf{u}) - \mu\frac{\omega^2}{{c_0}^2}\mathbf{v}\cdot\mathbf{u}, \end{aligned} \tag{3.35}$$

where $\mathbf{v}$ denotes a test function. The CWES is based on setting the integral of the weak form Eq. 3.35 over the domain of interest to 0, i.e.,

$$\int_\Omega \mathrm{d}\mathbf{r} F_H(\mathbf{v},\mathbf{u}) = 0. \tag{3.36}$$

In order to solve the eigenvalue described by Eq. 3.36, the three degrees of freedom that comprise the Bolch wavevector $\mathbf{k}$ have to be reduced to one by setting $\mathbf{k} = \mathbf{k}_0 + \lambda\mathbf{k}_n$. Here, λ denotes the eigenvalue solved for, $\mathbf{k}_0$ the offset wavevector, $\mathbf{k}_n$ a unit vector describing the direction of the corresponding eigenvalue solved for.

By carrying out the same mathematical procedure as for $\mathbf{H}$ field, one can get weak form for $\mathbf{E}$ field as the following:

$$\begin{aligned} F_E(\mathbf{v},\mathbf{u}) = {} & \frac{k^2}{\mu}\mathbf{v}\cdot\mathbf{u} - \frac{1}{\mu}(\mathbf{k}\cdot\mathbf{v})(\mathbf{k}\cdot\mathbf{u}) - i\frac{1}{\mu}\mathbf{v}\cdot[\mathbf{k}\times(\nabla\times\mathbf{u})] \\ & - i(\nabla\times\mathbf{v})\cdot\frac{1}{\epsilon}(\mathbf{k}\times\mathbf{u}) + (\nabla\times\mathbf{v})\cdot\frac{1}{\mu}(\nabla\times\mathbf{u}) - \epsilon\frac{\omega^2}{{c_0}^2}\mathbf{v}\cdot\mathbf{u}. \end{aligned} \tag{3.37}$$

The CWES method is convenient for calculating band diagrams of periodic metamaterials, especially when lossy dispersive materials, such as metals, are involved. It solves a quadratic eigenvalue problem, instead of solving a nonlinear eigenvalue problem iteratively, which is the case for using a real wavevector solving for complex eigen frequencies.

Chapter 4

Radiative Heat Transfer between Plasmonic Nanostructures

The previous chapter described a number of computational methods which allow direct calculation of radiative heat transfer (RHT) between plasmonic nanostructures and the corresponding photonic band structures. In this chapter, we demonstrate the tailorability and flexibility of using plasmonic nanostructures to achieve spectrally controllable enhanced RHT by studying two categories of plasmonic nanostructures based on these numerical methods. Section 4.1 briefly revisits the RHT between two homogeneous isotropic plates, which has been intensively studied during the last decade. Section 4.2 presents the numerical demonstration of RHT in grooved metal plate (GMP) sturctures, including 1D/2D GMPs and dielectric-filled 1D GMPs, and illustrates the role of SSPPs and waveguide modes in enhanced RHT. Section 4.3 describes the study on a rectangular and a trapezoidal profile-patterned HMM arrays based on a multilayer type-II HMM consisting of gold-silicon bilayers as discussed in Chapter 2. We demonstrate the unprecedented potential of profile-patterned HMMs in achieving a controllable super-Planckian RHT.

4.1 Unstructured Plates

It is known that when two bodies in vacuum are placed close enough to each other, at a length scale comparable to the corresponding thermal wavelength, a much higher radiative energy transfer, exceeding that dictated by Planck's law can be observed due to extra radiative energy transferred by photon tunneling via evanescent waves, including SPhPs, SPPs, frustrated total internal reflection modes, etc. Homogeneous polar dielectrics and noble metals have their intrinsic SPhP resonances in the infrared frequencies and surface plasmon resonances in the ultraviolet frequencies, respectively. The surface plasmon resonances are at too high frequencies to make significant contribution to RHT. As a result, most of the studies are focused on enhanced RHT mediated by the SPhPs [49, 50, 52, 55].

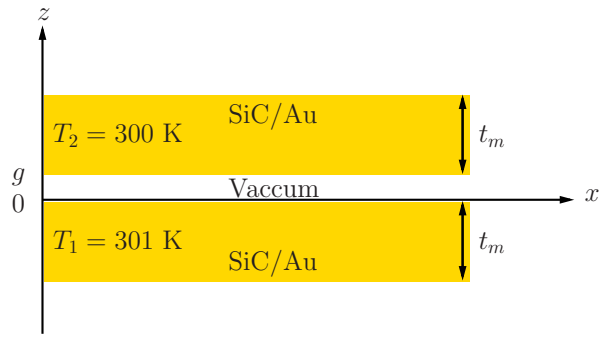

Figure 4.1: Geometry of two SiC or Au plates with the same thickness of t_m separated by a vacuum gap of g.The temperatures of the hot and the cold plates are $T_1 = 301$ K and $T_2 = 300$ K, respectively.

In this section, we present the near-field RHT between two homogeneous plates of phonon-polaritonic metals or plasmonic metals of the same thickness separated by a vacuum gap of g as depicted in Fig. 4.1. We take two representative materials, SiC and Au. The optical constant of SiC is described by a Drude-Lorentz model [118]:

$$\epsilon_{\mathrm{SiC}}(\omega) = \epsilon_\infty \left(\frac{\omega^2 - \omega_{\mathrm{LO}}^2 + i\gamma\omega}{\omega^2 - \omega_{\mathrm{TO}}^2 + i\gamma\omega} \right), \tag{4.1}$$

in which $\epsilon_\infty = 6.7$ is the high-frequency dielectric constant, $\omega_{\mathrm{LO}} = 182.53 \times 10^{12}$ rad/s the longitudinal optical phonon frequency, $\omega_{\mathrm{TO}} = 149.37 \times 10^{12}$ rad/s the transverse optical phonon frequency, and $\gamma = 0.8966 \times 10^{12}$ rad/s the collision frequency. The optical constant of gold is modeled by a Drude model:

$$\epsilon_{\mathrm{Au}}(\omega) = 1 - \frac{{\omega_{\mathrm{p}}}^2}{\omega(\omega + i\gamma)}, \tag{4.2}$$

in which $\omega_{\mathrm{p}} = 9$ eV, and $\gamma = 35$ meV, throughout this thesis.

Figures 4.2(a) and 4.2(b) present the transmission factors $\mathcal{T}_j(\omega, \beta)$ as a function of both angular frequency and surface-parallel wavevector for two SiC and gold plates, as depicted in Fig. 4.1, respectively. The thickness of plates is $t_m = 5$ μm and the vacuum gap size is $g = 50$ nm. For two SiC plates, there are two types of modes below the light line, i.e., $\beta > \frac{\omega}{c_0}$, which are evanescent in the vacuum gap. The first type of evanescent modes is confined between the light line of vacuum and that of SiC [indicated by the dashed white line in Fig. 4.2(a)], i.e., $\frac{\omega}{c_0} < \beta < \sqrt{\epsilon_{\mathrm{SiC}}}\frac{\omega}{c_0}$. These modes, which are propagating in SiC and evanescent in vacuum, are due to total internal reflections at SiC-vacuum interface. When the gap sizes are small enough, energy carried by these evanescent waves can be transfered from one plate to the other by photon tunneling. Due to the pole in optical constant

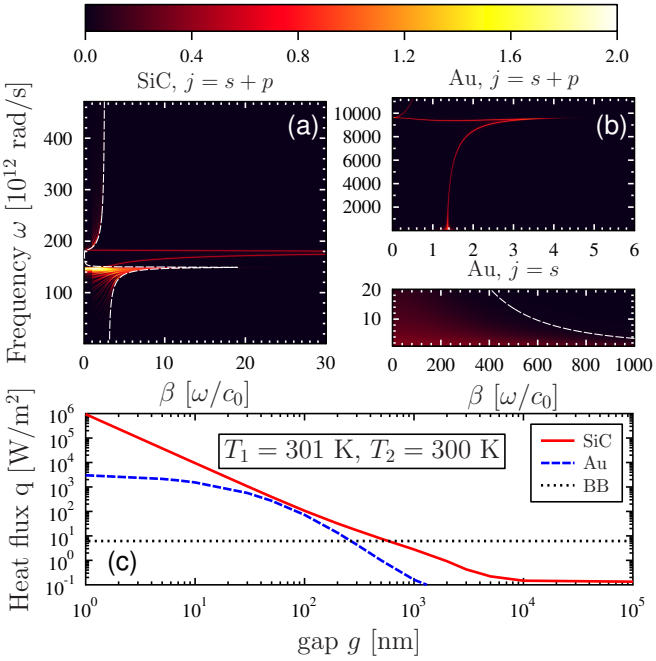

Figure 4.2: Transmission factor $\mathcal{T}_j(\omega, \beta)$ (a) between two SiC plates and (b) between two Au plates as depicted in Fig. 4.1 with thickness of 5 μm separated by a vacuum gap of $g = 50$ nm. The dashed white line denotes $\omega = \beta c_0/\sqrt{\epsilon_{\mathrm{SiC}}}$. (c) Heat flux between two plates structures as a function of gap size. The temperatures of the hot and cold plates are $T_1 = 301$ K and $T_2 = 300$ K, respectively. The dotted black line denotes the heat flux between two blackbodies with the same temperature configuration.

at transverse optical phonon frequency ω_{TO}, i.e., a large imaginary part around this frequency, the contributions are strong both below and above the light line of vacuum for frequencies close to ω_{TO}. However, this type of mode is still bounded by $\beta < \sqrt{\epsilon_{\mathrm{SiC}}}\frac{\omega}{c_0}$. On the contrary, the other type of evanescent mode between the transverse and longitudinal optical phonon frequencies, which is evanscent in both vacuum and SiC, can still be excited by p-polarized photons with very large surface-parallel wavevectors β. It originates from the coupling of thermally excited SPhPs at the top and bottom surfaces of SiC plates. The strong coupling of SPhP modes splits the mode into symmetric and antisymmetric SPhP modes. These SPhPs modes lead to a strong peak in spectral heat flux [see Fig. 4.3(a)]. The optical constants in this frequency range are negative; therefore the material behaves like metals. Thus, no frustrated total internal reflection modes can be excited [200]. In Fig. 4.3(a) and 4.3(b), we plot the heat flux between two identical SiC plates

and that between two identical Au plates for four different thickness settings, i.e., $t_m = 5$ μm, $t_m = 1$ μm, $t_m = 0.1$ μm and $t_m = 0.01$ μm, respectively. We find out that for a smaller plate thickness, which allows a stronger coupling between SPhPs supported by the top and bottom surfaces of each individual plate, the peak in spectral heat flux originating from SPhP resonances may be broadened but still within this frequency range. Even for asymmetric plates, i.e. two plates of different thicknesses, the resonance frequency can be hardly tuned outside the frequency range between transverse and longitudinal optical phonon frequencies as reported in Ref. [52].

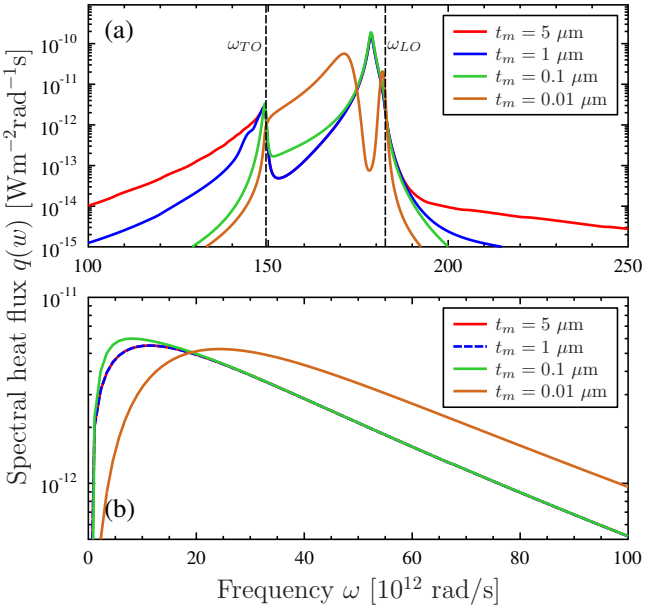

Figure 4.3: Spectral heat flux $q(\omega)$ (a) between two SiC plates and (b) between two Au plates as depicted in Fig. 4.1 with thickness of t_m separated by a vacuum gap of $g = 50$ nm.

Now turning to a plasmonic metal, we plot the transmission factor map between two gold plates of thickness $t_m = 5$ μm separated by a 50 nm vacuum gap in Fig. 4.2(b). The two brighter bands on the transmission factor map around surface plasmon frequency $\omega_{\rm sp} = \omega_{\rm p}/\sqrt{2} = 9669 \times 10^{12}$ rad/s originate from the symmetric and antisymmetric SPP modes as discussed in Chapter 2. However, SPP modes are at too high frequency, at which the mean energy of Planck's oscillators are too low to make significant contribution to RHT. At extremely low frequencies, there exists a broadband non-resonant contribution from s-polarized photons, which exisits even

for photons with very large surface-parallel wavevectors. This *s*-polarized non-resonant evanescent mode dominates the RHT for small gap sizes. The contribution of this mode is explained by the induced eddy currents [51]. The thermally excited *s*-polarized photons [electric field parallel to the metal surface] drive fluctuating currents flowing parallel to the gold-vacuum interface within the skin depth of gold in gold plates, which generate large magnetic fields at infrared frequencies. These fields penetrate into the other gold plate and generate large eddy currents which are dissipated by the Joule effect [51].

Figure 4.2(c) shows the heat flux between two SiC or Au plates of 5 μm thickness as a function of gap size. We can see that benifiting from the non-resonant *s*-polarized contribution at low frequencies, the RHT between gold plates at a gap size around 50 nm is almost as good as SiC. However, for gap sizes smaller than the skin depth of gold a saturation in heat flux appears as reported in Ref. [51].

Overall, the enhanced near-field RHT using homogeneous phonon-polaritonic metals or plasmonic metals lacks of spectral tunability, which is desired by many applications. Especially, for plasmonic metals, their SPP resonances are usually at ultraviolet frequencies which are too high to contribute to near-field RHT. On the other hand, the dominant *s*-polarized non-resonant heat transfer channels are at extremely low frequencies for practical applications besides heat dissipation. There is an urgent need to achieve a spectrally controllable near-field RHT for applications such as TPVs [201–203] and radiative cooling [64, 86–88].

4.2 Grooved Metal Plates

Metals are known as very good thermal conductors which have been used for heat dissipation applications such as heat sinks. Meanwhile, they are perfect reflectors for infrared radiations, which means poor absorption of infrared radiations. Thus, according to Kirchhoff's law metals are poor thermal emitters in the infrared regime, at which the Planck's oscillators are mainly distributed at room temperture. This fact has been widely deployed in our daily applications, e.g., vacuum flasks, survival blankets, which use metal coatings or films to keep heat from slipping away via far-field thermal radiation. From the previous section we know the fact that near-field coupling of surface waves can tremendously enhance the RHT, but SPPs intrinsically supported by homogeneous metals are at too high frequencies to make contributions. In order to enhance RHT between metals, we need to create artificial surface waves mimicking SPPs but in the infrared regime. In the seminal paper by J. B. Pendry *et al.* [127], it was shown that by perforating the surface of a perfect metal with 2D periodic array of subwavelength rectangular holes the nanostructured surface can support the so-called spoof surface plasmon polariton (SSPP) whose resonance frequency is mainly determined by the surface geometry. The SSPP can be designed with almost arbitrary dispersion in frequency and in space [127]. Later, people also observe SSPP in 1D/2D GMPs [128–136], and 2D perforated metal plates with holes of different shape [127, 128, 137, 138],

etc [139, 140]. In this section, we will thoroughly investigate the enhanced near-field RHT with GMP structures and elaborate the roles of different kinds of modes involved in the enhanced RHT.

4.2.1 1D Grooved Metal Plates with a Supercell

Here we start with a simple 1D GMP structure as described in Fig. 4.4. It consists of two identical gold plates nanostructured with 1D periodic array of grooves separated by a vacuum gap of g. The period of the unit cell is $a = 500$ nm. The width and the depth of the grooves are $b = 200$ nm and $h_1 = 4.7$ μm, respectively.

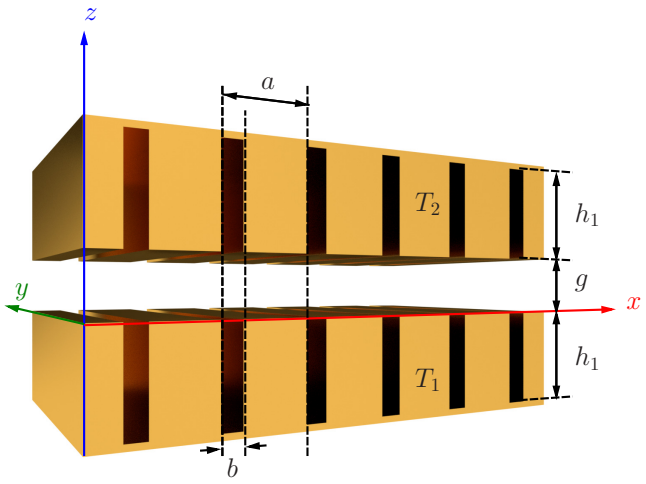

Figure 4.4: Geometry of two gold plates decorated with one-dimensional periodic array of grooves with width of $b = 200$ nm, depth of $h_1 = 4.7$ μm, and period of $a = 500$ nm. The vacuum gap size between these two plates is g.

Figure 4.5(a) shows the transmission factor $\mathcal{T}_{s+p}(\omega, k_x, k_y = 0)$ for surface-parallel wavevectors along x direction as a function of k_x and angular frequency ω using the RCWA method as we discussed in Chapter 3. The superimposed dashed white line indicates the dispersion relation of the modes supported by this structure calculated by CWES for p polarization. The dispersion curve falls on the brighter parts of the transmission factor map which indicate larger transmission factors. It implies that it is these modes supported by the double GMPs structure which contribute to the RHT. To further identify the origin of these modes, we plot the y component of magnetic field H_y in Fig. 4.5(c) corresponding to the four mode points on the band diagram marked by the orange markers in Fig. 4.5(a). The field distribution in each individual GMP is similar as that of SSPPs supported by a single GMP plotted in Fig. 2.13. It tells that the modes contributing to the brighter bands on the transmission factor map come from the coupling of SSPPs

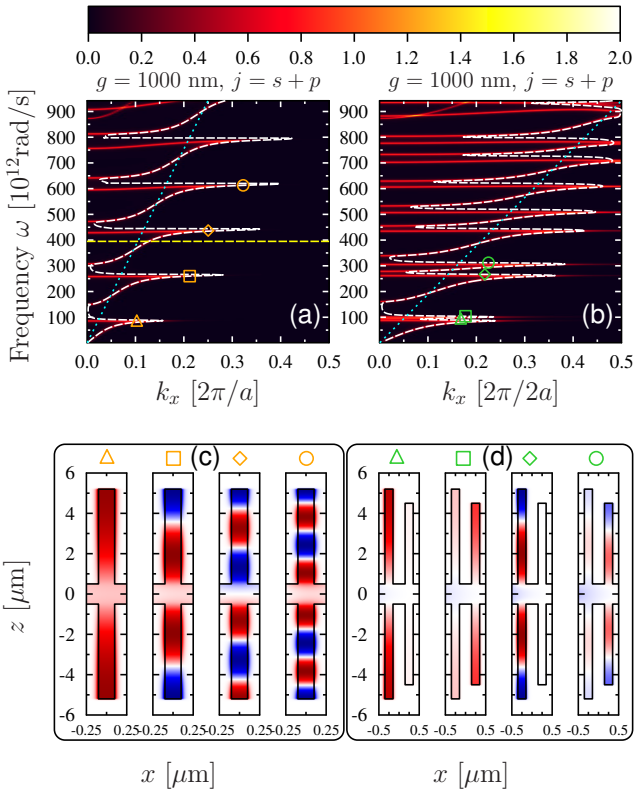

Figure 4.5: Transmission factor $\mathcal{T}_{s+p}(\omega, k_x, 0)$ between two one-dimensional grooved gold plates with a unit cell (a) of a single groove depth of $h_1 = 4.7$ μm and a period of $a = 500$ nm. (b) The same plot but for a supercell structure with double groove depths of $h_1 = 4.7$ μm, $h_2 = 4.0$ μm and a period of $2a = 1000$ nm. The groove width is $b = 200$ nm and the vacuum gap size is $g = 1000$ nm. The dashed white line denotes the dispersion relation of the structure, and the dotted cyan line denotes the light line in vacuum. The dashed yellow line indicates the frequency at which the transmission factors are plotted for whole k space in Fig. 4.7. The y components of magnetic fields H_y for the modes marked in (a) and (b) are mapped in (c) and (d), respectively.

supported by each individual GMP. As the two GMPs are brought close enough to each other, the coupling of the SSPP modes allows photon tunneling.

From Chapter 2 we know that the resonance frequency of SSPP is mainly determined by the depth of the grooves. It is natural that one can use a supercell structure, e.g., with a period of $2a$ but dual groove depths [see inset of Fig. 4.8(b)],

to enrich the number of resonances. In Figs. 4.5(b) and 4.5(d), we plot the transmission factor map $\mathcal{T}_{s+p}(\omega, k_x, k_y = 0)$ for the supercell structure with two groove depths $h_1 = 4.7$ μm, $h_2 = 4.0$ μm, groove width $b = 200$ nm, and the H_y field distributions corresponding to the marked mode positions on its dispersion curve, respectively. By having multiple groove depths one can certainly enrich the SSPP band within the same frequency range. However, as presented in the field distribution in Fig. 4.5(d), the coupling of the same order of SSPP supported by neighboring grooves of different depths may weaken the strength of resonances. To illustrate this, let's take the contribution to transmission factor map from the first order of SSPP resonance due to the groove depth of $h_1 = 4.7$ μm for both single- and double-groove-depth structures as an example. The transmission factor extinguishes faster as surface-parallel wavevector increases, approximately after $k_x = 0.2$ $\left[\frac{2\pi}{a}\right]$ for single-groove-depth structure and after $k_x = 0.18$ $\left[\frac{2\pi}{a}\right]$ for double-groove-depth-structure.

Apart from the p-polarized SSPP there also exists a s-polarized mode, which is not outlined by the dispersion curve, in both single- and double-groove-depth structures with a cutoff frequency around 870 [10^{12}rad/s]. This mode is purely above the light line, i.e. propagating mode, which comes from the s-polarized waveguide mode in the vacuum gap supported by MIM structure formed by the two GMP and the vacuum gap in between. This mode can still exist for s polarization. Because unlike for p polarization, the groove-vacuum interfaces can still be approximately treated as perfect metals.

To see what kind of modes contributes to RHT for surface-parallel wavevector along y directions, we plot the transmission factor as a function of both k_y and angular frequency for s and p polarization separately in Fig. 4.6. We also map the field distribution of the corresponding marked modes at angular frequency $\omega = 395 \times 10^{12}$ rad/s, as denoted by the dashed yellow line in Fig 4.5(a), at the bottom. The mode marked by the green star, which is very close to the light line, presents a G-SPP mode between MIM structure [see also Fig. 2.5 and Fig. 2.7]. The other four modes are the first- and the second-order symmetric and antisymmetric modes due to the coupling of the waveguide modes supported by each individual GMP. Each groove can be treated as a waveguide since the groove-vacuum interface can be approximately treated as a PMC and the groove bottom serves as a PEC.

Having looked at the contributions of surface waves propagating along either x or y directions, we would like to see how the mode evolves, as the direction of surface-parallel wavevector changing away from the direction perpendicular or parallel to the groove direction. In Fig 4.7, we plot the transmission factor as a function of both k_x and k_y at the same angular frequency. We also superimpose the dispersion of the modes within the first Brillouin zone, denoted by blue dots, to trace each mode. It shows that the surface modes are not isotropically excited for different wavevector directions, which gives rise to slightly broadened peaks in spectral heat flux [see Fig. 4.8]. Moreover, for surface-parallel wavevector direction between x and y direction, the waveguide modes are hybrid in polarization.

To evaluate the overall heat flux between two 1D periodic structure we integrate

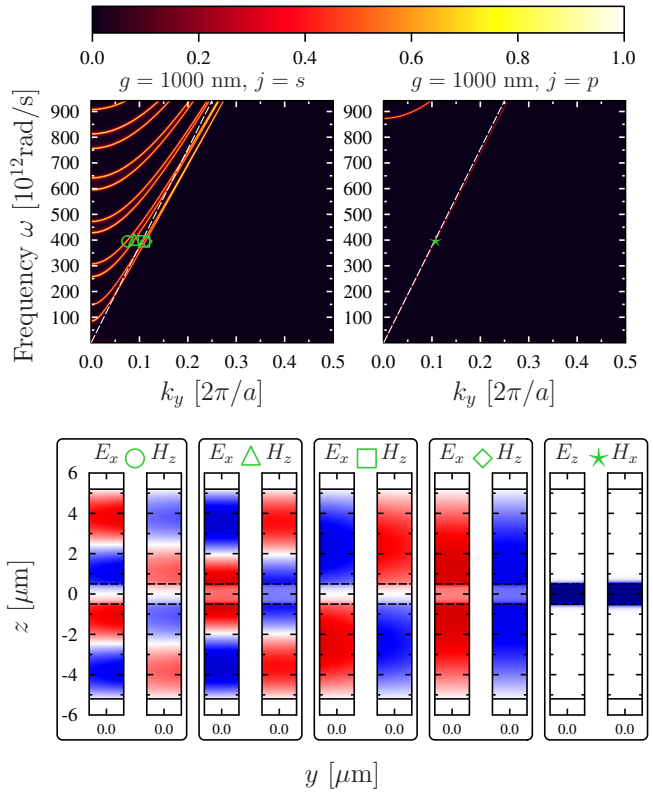

Figure 4.6: Transmission factor $\mathcal{T}_j(\omega, 0, k_y)$ between two one-dimensional grooved gold plates with a unit cell of a single groove depth of $h_1 = 4.7$ μm and gap size of $g = 1000$ nm for surface-parallel wavevectors along y direction. The white dashed line denotes the light line in vacuum. The field distribution in x-z plane across the middle of the groove for the modes marked by green markers are mapped at the bottom.

the transmission factor in the first Brillouin zone by

$$\Phi(\omega) = \frac{1}{4\pi^2} \sum_{j=s,p} \int_{-\infty}^{+\infty} \int_{-\frac{\pi}{a_x}}^{+\frac{\pi}{a_x}} \mathcal{T}_j(\omega, k_x, k_y) \mathrm{d}k_x \mathrm{d}k_y. \tag{4.3}$$

Figure 4.8 (a) presents the integrated transmission factor for both single lattice [solid lines] and supercell [dashed lines] GMP structures with gap sizes of $g = 1000$ nm, $g = 400$ nm, and $g = 100$ nm. As the gap size decreases we observe an increase in amplitude of integrated transmission factor due to the enhancement of near-field coupling. Compared to the single-groove-depth structure, the supercell GMP

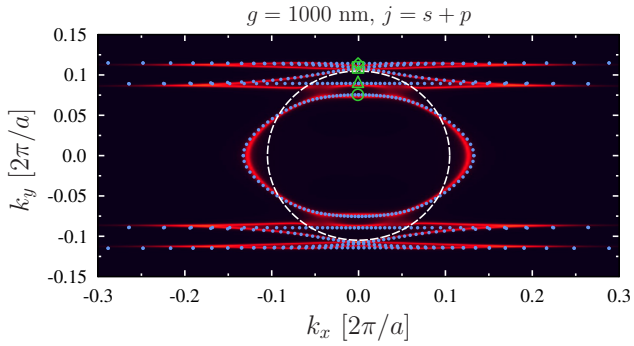

Figure 4.7: Transmission factor $\mathcal{T}_{s+p}(\omega, k_x, k_y)$ between two one-dimensional grooved gold plates with a unit cell containing a single groove of depth $h_1 = 4.7$ μm and gap size of $g = 1000$ nm at angular frequency $\omega = 395 \times 10^{12}$ rad/s. The blue dots denote the modes supported by this structure. The green markers are the same as those marked in Fig. 4.6. The dashed white line denotes the light line in vacuum.

structure with two different groove depths has an extra set of resonant peaks in integrated transmission factor owing to the SSPPs supported by the grooves with depth of $h_2 = 4.0$ μm. However, the peaks due to grooves with $h_1 = 4.7$ μm are not as strong as that in the corresponding single-groove-depth GMP structure. For gap size of $g = 100$ nm, both structures show a peak at very low frequencies due to the induced eddy current by s-polarized photons. The induced eddy current is a property possessed by closely spaced bulk metal plates as we discussed in the previous section. For both structures, the top surface area of metal in both GMP are the same in a unit area, which gives almost the same contribution to RHT due to such effect.

Figures 4.8(b) and 4.8(c) show the spectral heat flux between two 1D GMPs with temperature configurations of $T_1 = 301$ K, $T_2 = 300$ K and $T_1 = 701$ K, $T_2 = 700$ K for both single- and double-groove-depth GMPs. Due to the spectral distribution of Planck's oscillator [described by the blue and red shadings in Fig. 4.8(a)], the low-frequency components in integrated transmission factors weigh more than those for high frequencies, especially for lower temperatures. From Fig. 4.8(a) we know that the integrated transmission factor at the lower frequencies shows a great advantage over blackbodies [$\Phi_{\rm BB}$ denotes by solid black curve]. It leads to the super Planckian radiation at these frequencies as plotted in Fig. 4.8(a)-4.8(c).

In Figs. 4.9(a) and 4.9(b), we plot the contributions of s and p polarizations to the heat flux separately as a function of gap size for both temperature configurations as used in Fig. 4.8. For the lower temperature configuration [see Fig. 4.9(a)], the RHT is dominated by p-polarized modes for gap size larger than ~ 400 nm. For gap

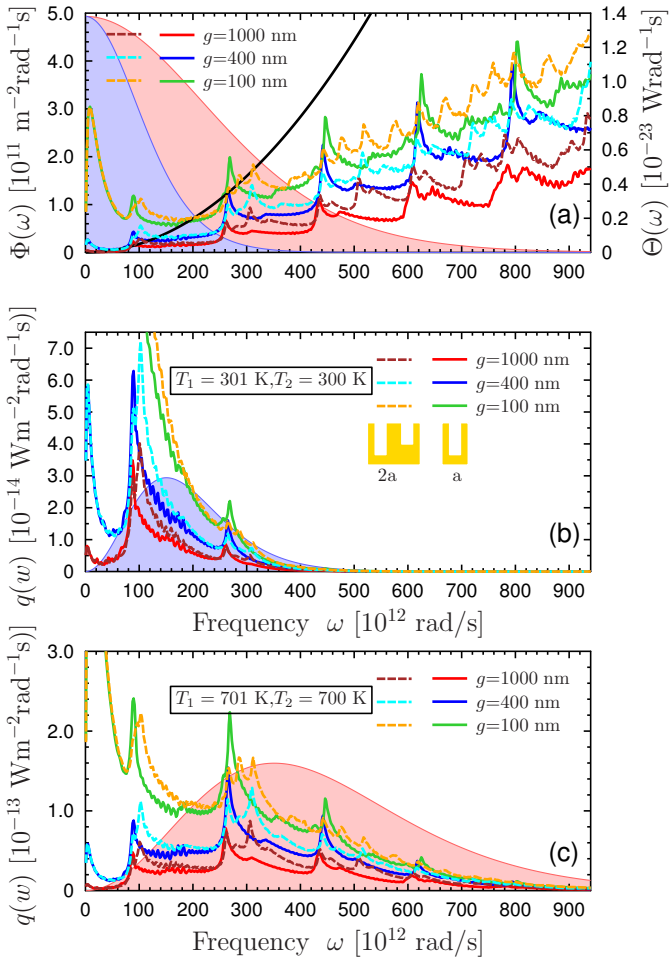

Figure 4.8: (a) Integrated transmission factor $\Phi(\omega)$ as a function of angular frequency for single- and double-groove-depth structures at different gap sizes. The solid black line denotes integrated transmission factors Φ_{BB} between two blackbodies. Spectral heat flux $q(\omega)$ for these two structures for (b) $T_1 = 301$ K, $T_2 = 300$ K and (c) $T_1 = 701$ K, $T_2 = 700$ K at different gap sizes. The solid lines and dashed lines present the results for single- and double-groove-depth structures as shown in the inset in (b), respectively. The blue shading and red shading denote the Planck's oscillator terms and spectral heat flux between blackbodies correspondingly.

sizes smaller than this, the contribution of s polarization takes over and becomes

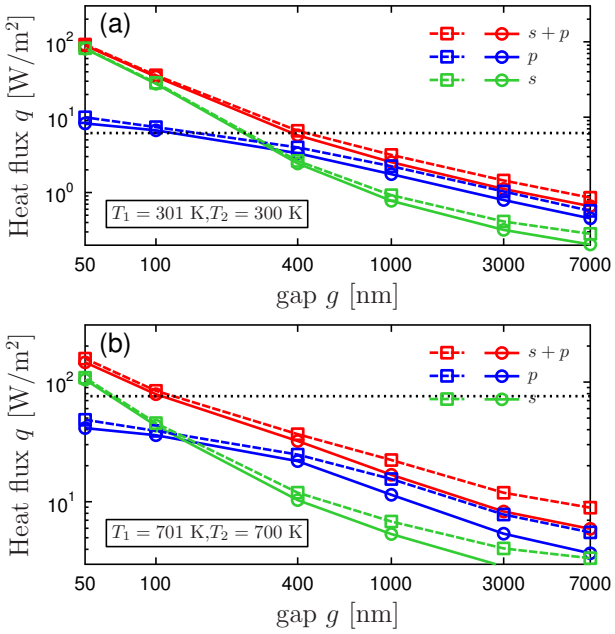

Figure 4.9: Heat flux for the single- and double-groove-depth structures as a function of gap size with temperature configurations of (a) $T_1 = 301$ K, $T_2 = 300$ K and (b) $T_1 = 701$ K, $T_2 = 700$ K. The dotted black line denotes the heat flux between two blackbodies with the corresponding temperature configurations.

more and more dominant as the gap size decreases. For the higher temperature configuration, this gap size moves to ~ 100 nm due to the spectral distribution of the Planck's oscillator. In order to exceed the heat transfer between two blackbodies, the gap size needs to be smaller than 400 nm and 100 nm, respectively. It implies that the 1D GMP structure discussed above with the corresponding parameters shows a great advantage over blackbodies in RHT for the lower temperature configuration in the near field. Moreover, by having a supercell GMP with multiple groove depths one can further enhance the RHT between GMPs [80]. To utilize it for relative higher temperature configurations, the parameters need to be redesigned, for instance decreasing the groove depth and period.

4.2.2 1D Grooved Metal Plates with Dielectric Fillings

In the previous subsection, we identified the role of coupled SSPPs in the enhanced RHT. Utilizing the fact that the resonance of SSPP can be engineered by the groove depth, we demonstrated that by having a supercell GMP structure one can further

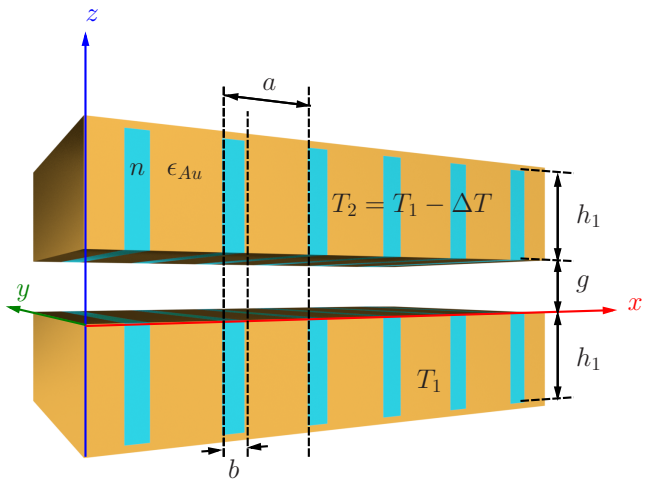

Figure 4.10: Geometry of two gold plates decorating with one-dimensional period array of grooves with width of $b = 200$ nm, depth of $h_1 = 5$ μm, and period of $a = 1000$ nm. The grooves are filled with a dielectric of refractive index of n, The vacuum gap size between these two plates is g.

enhance the RHT. Another way to increase the number of resonances within the thermal window of Planck's oscillator is to increase the groove depth physically or optically. Physically increasing the groove depth will lead to an insanely high aspect ratio of grooves which are difficult to fabricate from a practical point of view. In this subsection, we present further enhancement of the RHT by filling the grooves with a dielectric material, which optically increases the groove depth.

The schematic geometry of the structure under study is depicted in Fig. 4.10. It consists of two identical 1D gold GMPs filled with a dielectric of refractive index n separated by a vacuum gap of g without any lateral offset. The thickness gold substrate is 0.5 μm. The period $a = 1$ μm, groove width depth $h_1 = 5$ μm, and groove width $b = 200$ nm are fixed in this study. The refractive index n of the dielectric fillings varies from 1.0 to 4.0 with an increment of 0.5.

To illustrate the effects of dielectric fillings on the enhanced RHT, we map the transmission factor between two 1D GMPs filled with a dielectric with refractive index of $n = 4$, depth of 5 μm and that between two GMPs with depth of 5 μm and 20 μm without dielectric filling ($n = 1$) at a gap size $g = 1000$ nm for surface parallel wavevector along x and y directions in Fig. 4.11. The introduction of dielectric fillings will both increase the effective depth and width of the groove. The consequences of these two effects can be clearly seen by comparing the transmission factors of all three structures. Both resonance frequencies of p-polarized SSPP modes and cutoff frequencies of the s-polarized waveguide modes redshift because

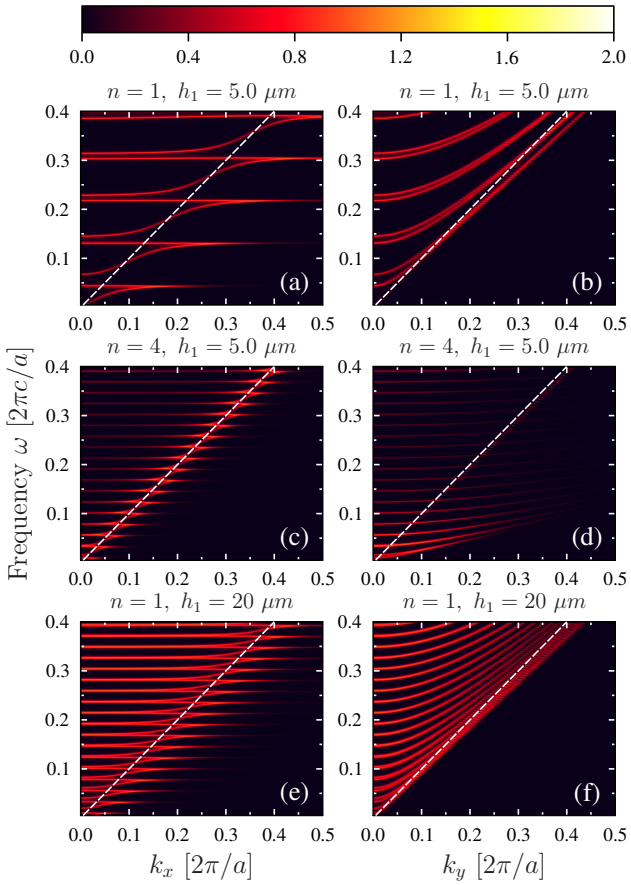

Figure 4.11: Transmission factor $\mathcal{T}_j(\omega, k_x, k_y)$ between two dielectric-filled grooved gold plates for $n = 1$, $h_1 = 5$ μm (a) along x direction, (b) along y direction, $n = 4$, $h_1 = 5$ μm (c) along x direction, (d) along y direction $n = 1$, $h_1 = 20$ μm (e) along x direction, (f) along y direction with a vacuum size of $g = 1000$ nm

of the increasing groove depth . On the other hand, the increase in groove width leads to more dispersive p-polarized SSPP modes [see Fig. 4.11(c)], i.e. decay faster with increasing wavevectors, but less dispersive s-polarized waveguide modes [see Fig. 4.11(d)]. The existence of nontrivial transmission factors below the light line in all structures leads to the enhanced near-field RHT.

The spectral distribution of radiative heat flux $q(\omega)$ can be obtained by Eq. 4.3. We plot the spectral heat flux $q(\omega, T_1, T_2)$ between two dielectric-filled GMPs for two temperature configurations, i.e., $T_1 = 250$ K, and $T_1 = 600$ K with $T_2 = T_1 - \Delta T$,

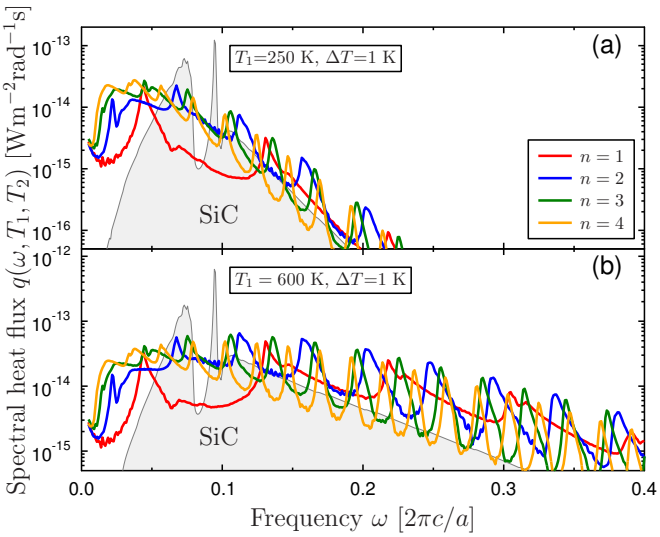

Figure 4.12: Spectral heat flux between two dielectric-filled grooved gold plates with $n = 1$, $n = 2$, $n = 3$, $n = 4$. The temperature of the hot plate and temperature difference between two plates are (a) $T_1 = 250$ K and $\Delta T = 1$ K; (b) $T_1 = 600$ K and $\Delta T = 1$ K. The solid black line with gray shading indicates the spectral heat flux between two SiC plates of 5.5 μm.

$\Delta T = 1$ K, in Fig. 4.12(a) and 4.12(b), respectively. For each temperature configuration four different spectra corresponding to four dielectric fillings with different refractive indices. For a comparison between dielectric-filled GMP structure and SiC plates, which have been most widely used for the study of near-field RHT, we superimpose the radiative heat flux between two identical SiC plates of the same overall thickness, i.e., 5.5 μm, and the corresponding temperature configuration in Figs. 4.12(a) and 4.12(b). The frequencies of the peaks presented in spectral heat flux can be well correlated to the resonance frequencies of the coupled SSPPs, i.e. zero-dispersion band as observed in the transmission factor map for surface-parallel wavevector along x direction. The increases in refractive index of the dielectric filling shift the resonant peaks in spectral heat flux to the lower frequencies, where the Planck's oscillator term has a larger value. We also observe a broadening in spectral heat flux at low frequencies. It originates from the s-polarized waveguide modes, which become less dispersive and even support the symmetric and antisymmetric waveguide mode pairs below the light line due to the dielectric fillings.

Figure 4.13(a) and 4.13(b) show the heat flux between two dielectric-filled gold GMPs as a function of both refractive index of the dielectric filling and the temperature of the hot plate T_1. Two scenarios, i.e., temperature difference of $\Delta T = 1$ K

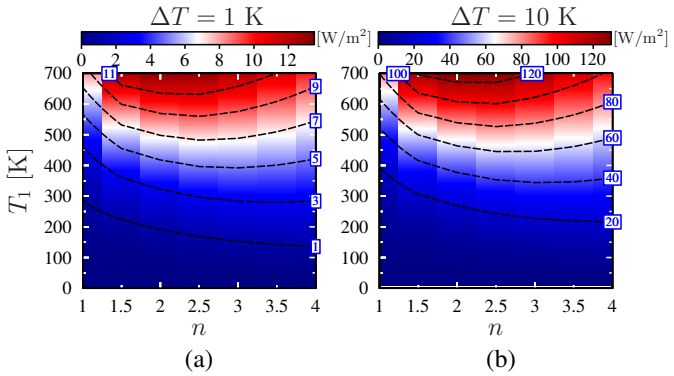

Figure 4.13: Heat flux between two dielectric-filled grooved gold plates as a function of refractive index of the filled dielectric n and the temperature of the hot plate T_1. The temperature difference between the two plates are (a) $\Delta T = 1$ K, and (b) $\Delta T = 10$ K. The dashed black lines denote the lines of equal heat flux.

and $\Delta T = 10$ K, are studied. In the lower temperature regime, the GMPs filled with a higher refractive index show a larger heat flux. On the contrary, for higher temperatures the largest heat flux happens at a moderate filling refractive index. This can be explained by the profile of Planck's oscillator Θ. At lower temperatures, the GMPs benefit *majorly* from having an increasing number of resonances at *lower* frequencies with a higher index of the dielectric fillings. That's why we observe the radiative heat flux increases monotonically with increasing refractive index in Fig. 4.13. At higher temperatures, the Planck's oscillator term weighs more and more heavily on resonances at higher frequencies. Since there are already many resonances contributing critically to the RHT, further contributions from additional number of resonances owing to a optical dense dielectric filling may become less significant. Moreover, the higher refractive index of the dielectric filling can negatively affect the heat flux due to the fact that the p-polarized SSPP modes decay faster with increasing wavevectors. As a result, we observe first an increase and then a decrease in radiative heat flux at higher temperatures. We compare the overall heat flux between two GMP with or without dielectric filling and observe a relative enhancement up to 650%. This highest enhancement is obtained at $T_1 = 77$ K and refractive index of the dielectric filling of $n = 4$. At room temperature, this enhancement is about 3 times. Therefore, a dielectric filling provides us another degree of freedom for designing the GMP structures to achieve the enhanced RHT.

Since a dielectric filling affects the properties of surface modes, including s-polarized waveguide modes and p-polarized SSPP modes, it should directly affect the dependence on gap size of evanescent wave mediated RHT. In Fig. 4.14 we compare the heat flux as a function of gap size between two 1D GMPs with a

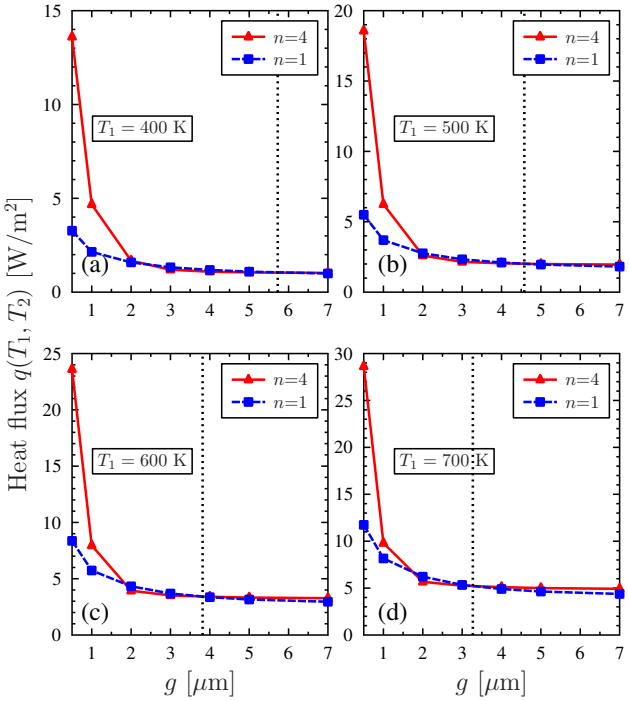

Figure 4.14: Heat flux between two dielectric-filled grooved gold plates with $n = 1$ and $n = 4$ as a function of vacuum gap size g. The temperature of the hot plate is (a) $T_1 = 400$ K, (b) $T_1 = 500$ K, (c) $T_1 = 600$ K, and (d) $T_1 = 700$ K, respectively. The temperature difference between the hot plate and the cold plate is $\Delta T = 1$ K. The black dotted lines indicate thermal wavelengths for the corresponding temperatures.

dielectric filling of $n = 4$ to that between two GMPs without dielectric fillings. Four different temperature settings, i.e., $T_1 = 400$ K, $T_1 = 500$ K, $T_1 = 600$ K, and $T_1 = 700$ K with $\Delta T = 1K$, are presented in Figs. 4.14(a)-4.14(d), respectively. The comparison of heat flux between two GMPs with or without dielectric filling indicates that the dielectric-filled GMP structure owns a much larger heat flux and it decreases faster in the very near-field regime with increasing gap size. It implies that the coupling between the evanescent modes supported by dielectric-filled GMPs are more sensitive to changes in gap size in this regime. As the gap size further increases, the contribution originating from coupled evanescent modes becomes weaker, thus the RHT is less gap size dependent in this region. Due to the less dispersive [strongly coupled] SSPPs modes, the heat flux between two GMPs without dielectric fillings becomes slightly larger compared to the dielectric-filled GMPs at certain gap sizes. In the far-field regime, when the gap size larger than the corresponding thermal wavelength, the dielectric-filled GMPs possess more

propagating modes than the GMPs without dielectric fillings. It results in a larger heat flux for the dielectric-filled GMPs in this regime.

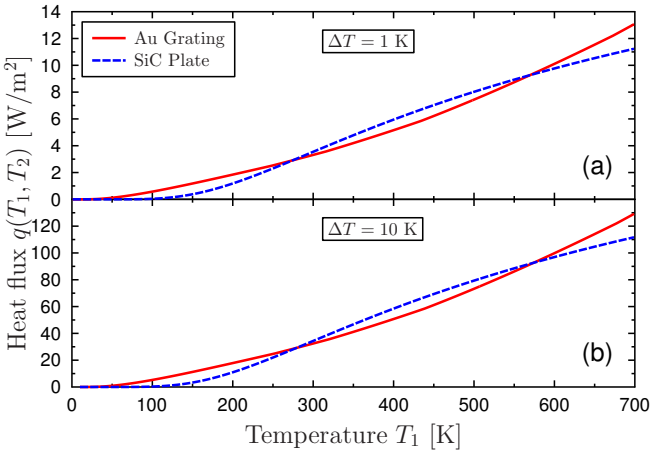

Figure 4.15: Maximum achieved heat flux between two dielectric-filled grooved metal plates from Fig. 4.13 (solid red lines) and heat flux between two SiC plates of 5.5 μm (dashed blue lines) as a function of temperature of the hot plate T_1. The temperature differences between the two plates are (a) $\Delta T = 1$ K and (b) $\Delta T = 10$ K.

As discussed above, the dielectric-filled GMPs can further enhance the RHT, hence it will be interesting to compare it to SiC, which is a popular choice of material for the study of enhanced RHT due to its SPhP resonance at $\omega = 1.786 \times 10^{14}$ rad/s. For comparison, we choose the largest achieved heat flux from Fig. 4.13 at different temperatures T_1 and compare to that between two SiC plates of 5.5 μm in thickness. The temperature and the total thickness of these two structures are identical. Heat fluxes for these two structures with two temperature difference $\Delta = 1$ K and $\Delta = 10$ K are plotted in Figs. 4.15(a) and 4.15(b), respectively. We can see that for both scenarios the dielectric-filled GMPs perform better than SiC in RHT in the temperature range smaller than ~ 270 K or larger than ~ 570 K. To understand this we can refer to the superimposed spectral heat flux in Fig. 4.12 and also Section. 4.1. The very sharp peak around $\omega \approx 0.1$ $[2\pi c/a]$ is due to the symmetric and antisymmetric SPhP resonances and the broad peak around $\omega \approx 0.08$ $[2\pi c/a]$ is due to frustrated total internal reflections. At lower temperatures, the Planck's oscillator term Θ has a relatively lower value for frequencies close to SPhP resonance. For dielectric-filled GMP structure, it has richer SSPP modes in the lower frequency range, where the Θ term has a larger value. Even though the peaks corresponding to these resonances are not as high as those due to SPhP

resonances for SiC, the overall heat flux can still be larger. At higher temperatures, the resonances at higher frequencies start to play a non-negligible role in the RHT. However, SiC plates don't support any resonances in high-frequency regime that can contribute to the RHT. This is why the dielectric-filled GMP has the advantage over SiC plates in this temperature region.

In conclusion, we have demonstrated the enhanced RHT with 1D GMPs with or without dielectric filling. It can enhance the RHT tremendously, and provides us another way to tailor the spectral properties. The anisotropic contribution from SSPPs with wavevectors along different surface-parallel directions implies that the spectral-selectivity can still be further improved for applications such as TPVs. It is worth commenting that other noble metals, which can be approximately treated as PECs in the infrared regime, can also used for GMP structure to enhance near-field RHT.

4.2.3 2D Grooved Metal Plates

The 1D GMP supports both SSPP modes and waveguide modes which can enhance the near-field RHT. However, due to the lack of symmetry (C_2) of 1D GMP, these modes cannot be isotropically excited for different surface-parallel wavevector directions; this leads to a broadening of peaks in spectral heat flux. In this subsection, we introduce a 2D GMP structure, which has a C_4 symmetry, for enhanced RHT with a better spectral selectivity.

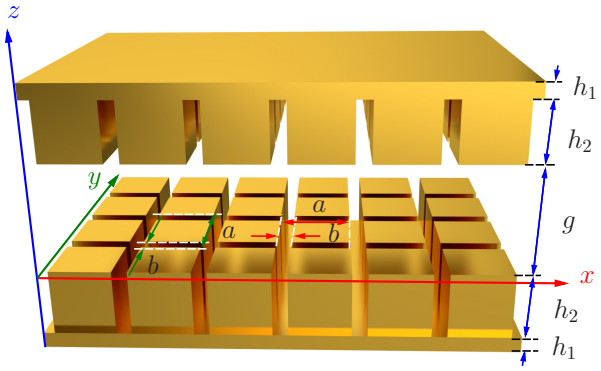

Figure 4.16: Geometry of two two-dimensional grooved metal plates with a square lattice with a period of $a = 1$ μm separated by vacuum gap of g. The thickness of the homogeneous gold substrate is $h_1 = 1$ μm. The groove depth and groove width are $h_2 = 4.7$ μm and $b = 200$ nm, respectively. The temperatures of the bottom (hot) and top (cold) plates are $T_1 = 301$ K and $T_2 = 300$ K, respectively.

The schematic geometry of the 2D GMP under study is depicted in Fig. 4.16. It consists of two identical 2D grooved gold plates, without any lateral offsets or

rotations, separated by a vacuum gap of g. We choose a simple square lattice with period of $a = 1$ μm. The groove width $b = 200$ nm, groove depth $h_2 = 4.7$ μm, and the thickness of the homogeneous gold substrate $h_1 = 1$ μm are fixed. We choose the temperatures of the hot (bottom) and cold (top) plates at $T_1 = 301$ K and $T_2 = 300$ K. These parameters are chosen to make sure that the 2D GMPs exhibit resonant modes within the frequency range where the Planck's oscillator term has a relatively large value at the given temperatures.

In order to investigate the contribution from different thermally excited s- and p-polarized modes supported by the 2D GMP structure, we plot the transmission factor $\mathcal{T}_j$ of each polarization separately along $\Gamma - X$ as a function of angular frequency in Fig. 4.17. Three gap sizes of $g = 3000,\ 1000,\ 100$ nm are presented. At $k_x = 0$ and $k_y = 0$ in $\mathbf{k}$-space, the s-polarized mode and p-polarized mode are degenerate due to C_4 symmetry of the 2D GMP structure. Compared to 1D GMPs, RHT between 2D GMPs contains s-polarized contributions [see Figs. 4.17(a), 4.17(c), 4.17(e)] for surface-parallel wavevector along x direction. When examined carefully, the contribution is very similar to that of 1D GMPs for surface-parallel wavevector along y direction [see Figs. 4.6 and 4.11(b)]. They in fact share the same origin, i.e., owing to the symmetric and antisymmetric waveguide modes. The high transmission factors of p polarization [see Fig. 4.17(b), 4.17(d), 4.17(e)] clearly picture the dispersion curves of SSPPs as in the 1D GMP case [see Fig. 4.5(a)].

As the gap size decreases, the contribution below the light line becomes more and more significant and the splitting between the s-polarized symmetric and antisymmetric modes becomes more notable. Moreover, for gap size as small as $g = 100$ nm, the non-resonant contribution due to induced eddy current [51] starts to play a significant role and the p-polarized SSPP mode can be excited by thermally excited photons with $\mathbf{k}$-vector as large as $k_x = 0.5$ $[2\pi c/a]$, which is at the first Brillouin zone boundary. Both of these phenomena indicate a further enhancement in the RHT at a small gap size.

In order to confirm the physical origin of these modes, we plot the photonic band digram calculated using CWES and the corresponding electromagnetic field distribution of the marked modes for two 2D GMPs structure with a vacuum of $g = 1000$ nm in Figs. 4.18(a)-4.18(c). The summation of transmission factors in Fig. 4.17(c) and 4.17(d) are superimposed in the band diagram to get a better correlation between the photonic modes and their contributions to the RHT [see Fig. 4.18(a)]. For p-polarized modes, the H_y field in the x-z plane across the middle of the groove is presented, which shows the the 1st and the 2nd order of SSPP modes [see Fig. 4.18(b)]. For s-polarized modes, the E_y component, which has its zero at the groove-gold interface (approximately PEC) maximum at groove-vacuum interface (approximately PMC) are plotted. It clearly indicates the 1st and the 2nd order of symmetric and antisymmetric waveguide modes [see Fig. 4.18(c)].

In Figs. 4.19(a)-4.19(d), we plot the transmission factor, s- and p-polarized contributions separately, between two 2D GMPs separated by gap sizes of $g = 1000, 100$ nm for all surface-parallel wavevector directions [from 0 to 2π with re-

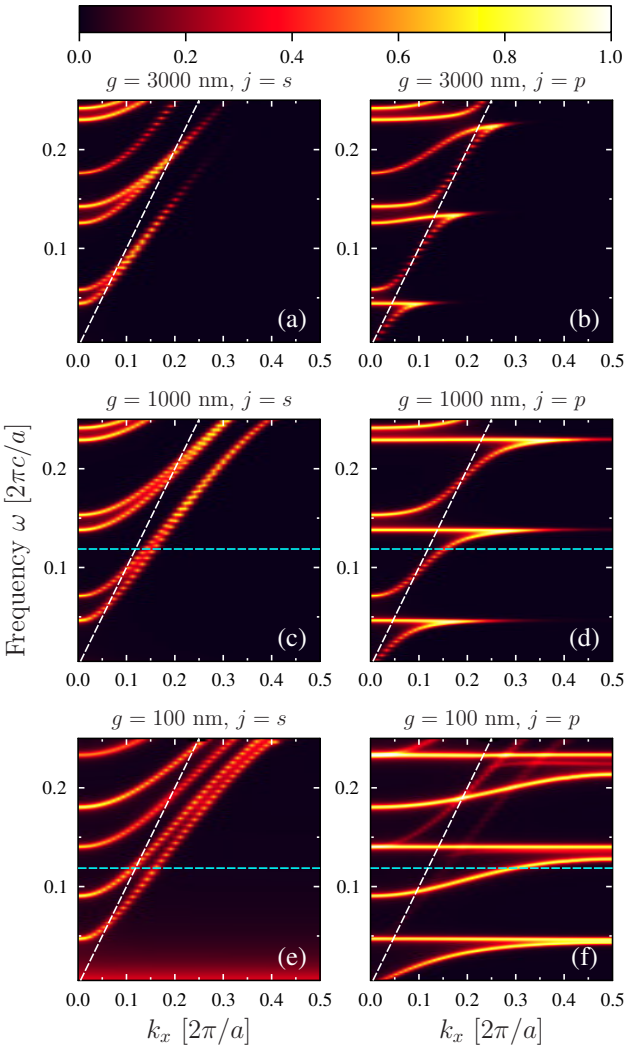

Figure 4.17: Transmission factors $\mathcal{T}_j(\omega, k_x, 0)$ of s- and p-polarizatoins between two grooved metal plates with surface-parallel wavevector along Γ-X direction as a function of angular frequency ω and wavevector k_x for gap size of (a) $g = 3000$ nm, (b) $g = 1000$ nm, and (c) $g = 50$ nm. The white dashed line denotes the light line in vacuum and the cyan dashed line denotes the frequency at which the transmission factors for wavevector of all surface parallel directions are mapped in Fig. 4.19.

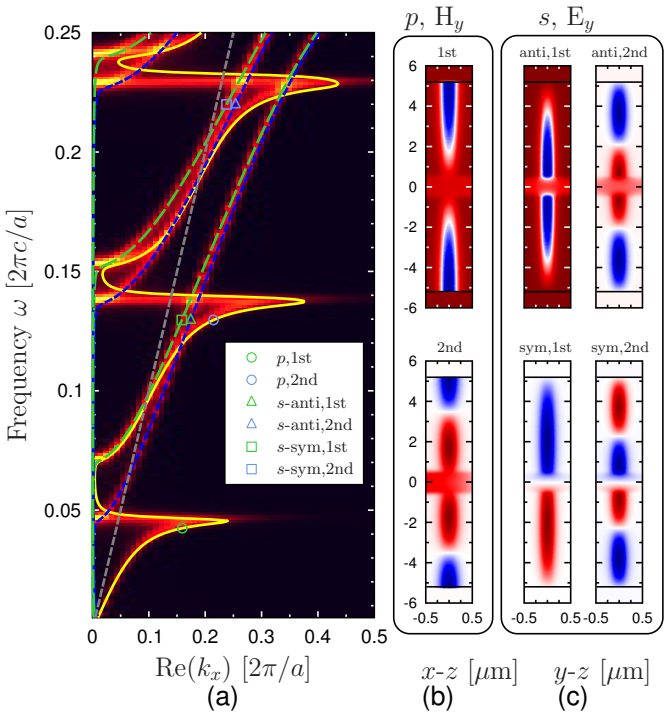

Figure 4.18: (a) The dispersion relation of the two grooved metal plates separated by a vacuum gap of $g = 1000$ nm for wavevector along Γ-X direction and the transmission factor for both s (TE) and p (TM) polarization (colormap). The solid yellow curve denotes the p-polarized modes, and the dashed lines denote the symmetric (green) and antisymmetric (blue) s-polarized modes. The field distributions of the marked p-polarized modes in x-z and s-polarized modes in y-z plane in (a) are mapped in (b) and (c), respectively.

spective to x axis] at angular frequency $\omega = 0.1306$ $[2\pi c/a]$. The transmission factor map shows almost an isotropic behavior for both s and p polarizations. Such isotropic transmission factor is preserved even at the resonance frequencies of SSPPs, which will give rise to a better frequency selectivity in spectral heat flux. To examine the spectral properties of heat flux between two 2D GMPs, we show the spectral heat flux in Figs. 4.20(a)-4.20(c). For comparisons, we also superimpose the spectral heat flux between two 1D GMPs and that between two homogeneous gold plates with thicknesses of 5.7 μm. The period and the groove geometry of 1D GMP and 2D GMP are identical. It is shown that for gap size of $g = 400$ nm [or even larger, not shown here], the RHT is mainly contributed by the 1st order of SSPP mode, leading to a sharp peak at angular frequency around $\omega = 86 \times 10^{12}$ rad/s.

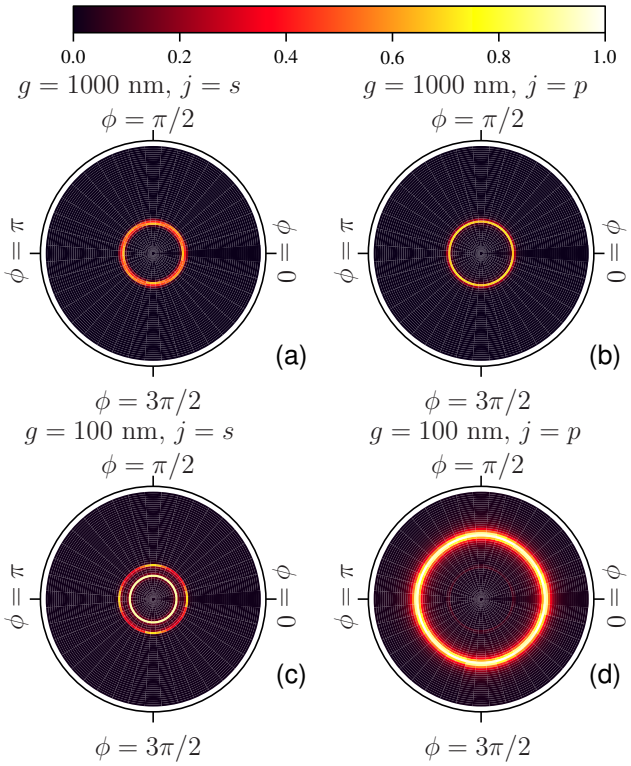

Figure 4.19: The transmission factor at angular frequency $\omega = 0.1306\ [2\pi c/a]$ (cyan line in Fig. 4.17) for surface-parallel wavevector directions ranging from 0 to 2π with respect to $+x$ axis for (a) s polarization, (b) p plarization with gap size of $g = 1000$ nm, and (c) s polarization, (d) p polarization with gap size of $g = 100$ nm.

The lower peak at $\omega = 262 \times 10^{12}$ rad/s mainly comes from the contribution of the 2nd order SSPP mode. Due to the spectral distribution of Planck's oscillator [see Fig. 4.8(a)], even though it has a higher amplitude in integrated transmission factor $\Phi(\omega)$, the spectral heat flux can still be lower. It is worth commenting that at higher temperatures even higher-order modes may make non-negligible contributions to the near-field RHT. Since the s-polarized waveguide modes exhibit more dispersive bands, their spectral heat flux is broadband and weaker compared to SSPP modes.

As the gap size further decreases, a broadband peak at very low frequencies starts to dominate the RHT process. This comes from the heat dissipation via the Joule effect due to the surface induced eddy current [51] as shown in Fig. 4.17 (e). The fact that the non-resonant broad peak weighs much more than geometry-

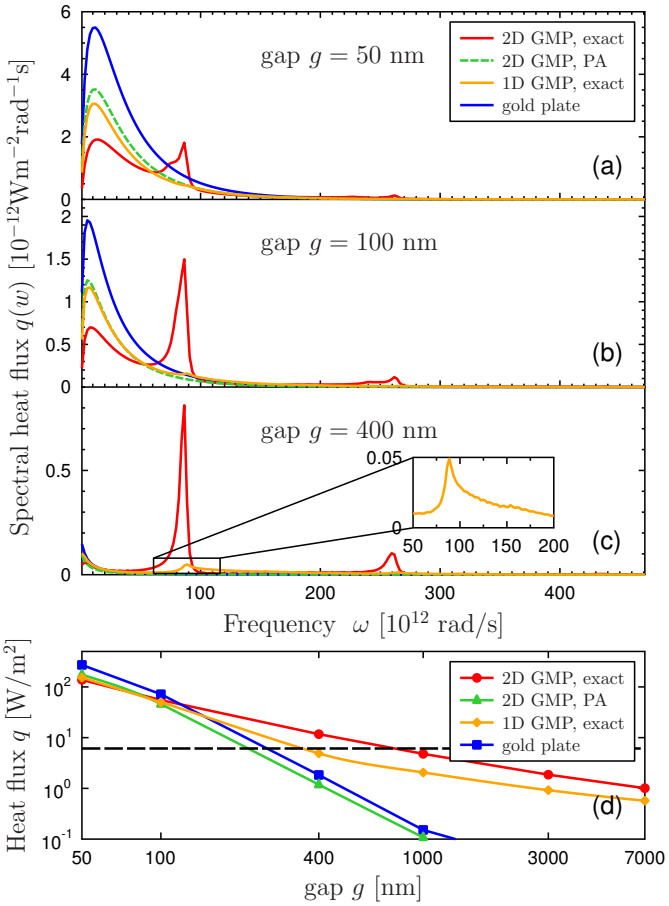

Figure 4.20: Spectral heat flux between two two-dimensional grooved gold plates with an exact solution calculated by a scattering approach (solid red line) and PA (dashed red line), two 1D grooved gold plates, and two 5.7 μm gold plates for gap size of (a) $g = 400$ nm, (b) $g = 100$ nm, (c) $g = 50$ nm. (d) The integrated heat flux as a function of gap size for these four configurations with temperature configuration $T_1 = 301$ K, $T_2 = 300$ K. The black dashed line denotes the heat flux between two blackbodies.

induced modes, especially at a small gap size, motivates us to check the validity of Derjaguins proximity approximation (PA). We find out that the PA can capture the basic features of spectral heat flux at very low-frequency due to induced eddy

current as shown in Fig. 4.20(a)-4.20(c).

An important spectral property achieved using 2D GMPs for the enhanced RHT is that SSPP modes give rise to sharper and higher peaks in the spectral heat flux $q(\omega)$ thus a better frequency selectivity [see Fig. 4.20(c)]. The property is owing to the isotropic contribution from thermally excited photons with different surface-parallel wavevector directions as demonstrated by Figs. 4.19(a)-4.19(d). Such superior frequency selectivity is important for, e.g., near-field TPV applications.

Figure 4.20(d) plots the overall heat flux for the structures demonstrated in Figs. 4.20(a)-4.20(c) as a function of vacuum gap size. We find out that for gap size larger than 100 nm the GMP structure significantly enhances the RHT compared to those using unstructured homogeneous gold plates. The enhancement is about two orders in magnitude at gap size of $g = 1000$ nm and increases towards larger gap sizes. As for sub-100-nm gap sizes, the frustrated mode due to induced eddy current prevails over the geometry induced modes, which leads to a better performance of unstructured gold plates. However, this frustrated mode is at too low frequencies and has a very poor frequency selectivity.

Overall, the 2D GMP structure allows us to achieve the enhanced RHT with a great spectral tailorability. By properly designing especially 2D GMP, one can achieve enhanced RHT via desired frequency channels, which is extremely attractive for certain applications.

4.3 Profile-Patterned Hyperbolic Metamaterials

In the previous section, we study the RHT between GMPs by taking a representative noble metal, i.e. gold, as the constitutional material. In the current section we turn to a HMM based structure. Due to their exotic properties for manipulation of electromagnetic field, HMMs have drawn a lot of attention for enhanced near-field RHT [56–58, 77, 84, 85]. Significant enhancements in near-field RHT in two types of HMM based structures have been demonstrated: (i) HMM formed by a stack of deep subwavelength bilayers consisting of a homogeneous layer of phonon-polaritonic metals, such SiC or heavily doped Si, and a homogeneous layer of dielectrics [56–58]; (ii) nanowire arrays consisting of phonon-polaritonic metals embedded in a dielectric matrix [77, 84, 85]. Most of these studies are limited to smooth plates of HMMs, and the RHT phenomena were therefore determined by the homogenized material properties of hyperbolic media. Due to the complexity in numerical simulations, profile-patterned HMMs, which could potentially give rise to a superior spectral tailorability, has not yet been studied. For nanowire HMMs, the enhanced RHT has been calculated with the help of effective medium theory (EMT) [77, 85]. However, the effective medium theory (EMT) cannot always precisely predict the RHT between two closely spaced nanowire HMMs or two multilayer HMMs, even for a gap size larger than the peiodicity in the HMMs [177, 178].

In this section, we numerically demonstrate the super-Planckian RHT with profile-patterned HMMs using a rigorous scattering approach based on RCWA.

4.3.1 Rectangular-Shaped Hyperbolic Metamaterial Array

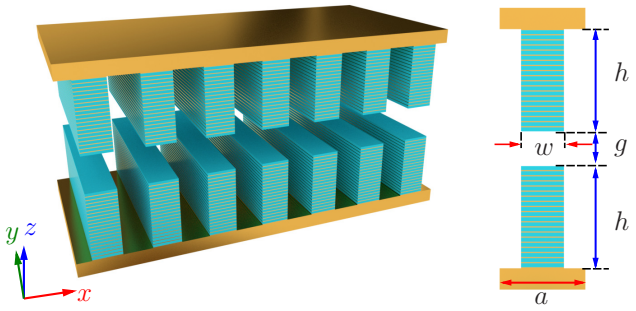

Figure 4.21: Geometry of two rectangular-shaped hyperbolic metamaterial arrays separated by a vacuum gap g. The width and the height of the grating are $w = 1000$ nm and $h = 2300$ nm, respectively. The period of the grating is $a = 2000$ nm. The cyan layers denote dielectric and the golden layers denote gold.

We start with a simple rectangular-shaped HMM array structure to facilitate easier understanding of the underlying physical mechanism of RHT between profile-patterned HMMs. Later on, we move to a more complex trapezoidal-shaped HMM array structure which shows ultrabroadband super-Planckian RHT.

The HMM used as the building blocks consists of 20 deep subwavelength Si-Au bilayers which we discussed in Chapter 2. The top and bottom layers are Si and Au, respectively. The thickness of Si layer is $t_d = 95$ nm and that of Au layer is $t_m = 20$ nm. The schematic geometry of the two rectangular-shaped HMM plate structure is described in Fig. 4.21. Each plate consists of a periodic array of rectangular-shaped HMM and a gold substrate. The width of the rectangular is $w = 1000$ nm and the height is equal to the thickness of the HMM, i.e., $h = (95\text{ nm} + 20\text{ nm}) \times 20 = 2.3\ \mu$m. The period is $a = 2000$ nm and the vacuum gap size is g.

To show the possibility of utilizing this kind of profile-patterned HMM for enhanced near-field RHT, we plot transmission factor $\mathcal{T}_j(\omega, k_x, k_y = 0)$ between two such rectangular-shaped HMM arrays for surface-parallel wavevector along x direction as a function of angular frequency ω and k_x. Four different gap sizes $g = 5000,\ 1000,\ 500,\ 50$ nm are presented in Fig. 4.22. We observe several bands with both propagating and evanescent states that contribute to the RHT. Particularly as the gap size decreases, the splitting of the two low-frequency bands

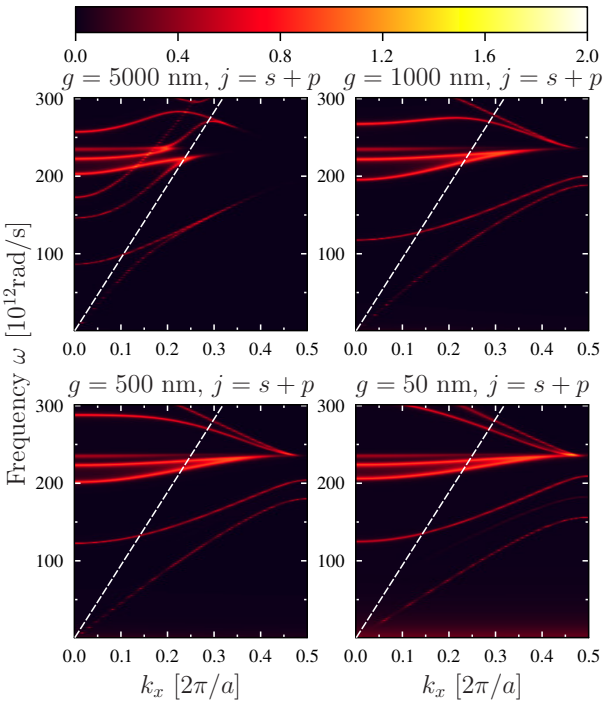

Figure 4.22: Transmission factor $\mathcal{T}_j(\omega, k_x, 0)$ between two rectangular-shaped hyperbolic metamaterial arrays depicted in Fig. 4.21 for surface-parallel wavevector along x direction at different gap sizes $g = 5000$ 1000, 500, 50 nm. The dashed white line indicates the light line in vacuum.

increases. For gap size of $g = 50$ nm, the contribution from induced eddy currents is observed.

To gain further knowledge of the origin of these modes, we plot the complex valued $k_x(\omega)$ dispersion curves of the two profile-patterned HMM plates structure with a vacuum gap size of $g = 1000$ nm, as well as their representative electromagnetic field distributions in Fig. 4.23. We also superimpose the corresponding transmission factor $\mathcal{T}_j(\omega, k_x, 0)$ to link each mode to its contribution to the RHT. In the field distribution maps, the color maps and the arrow maps present the y component of magnetic field H_y and the in-plane electric field component in x-z plane. Field distributions at points I and II imply that the light-blue bands are antisymmetric and symmetric SPPs supported between two gold substrates filled by a two rectangular-shaped HMM arrays plus a vacuum layer. The symmetric mode exhibits a lower cutoff frequency, while the antisymmetric mode does not. As we discussed in Chapter 2, this HMM is a type-II HMM. Since the electric field is

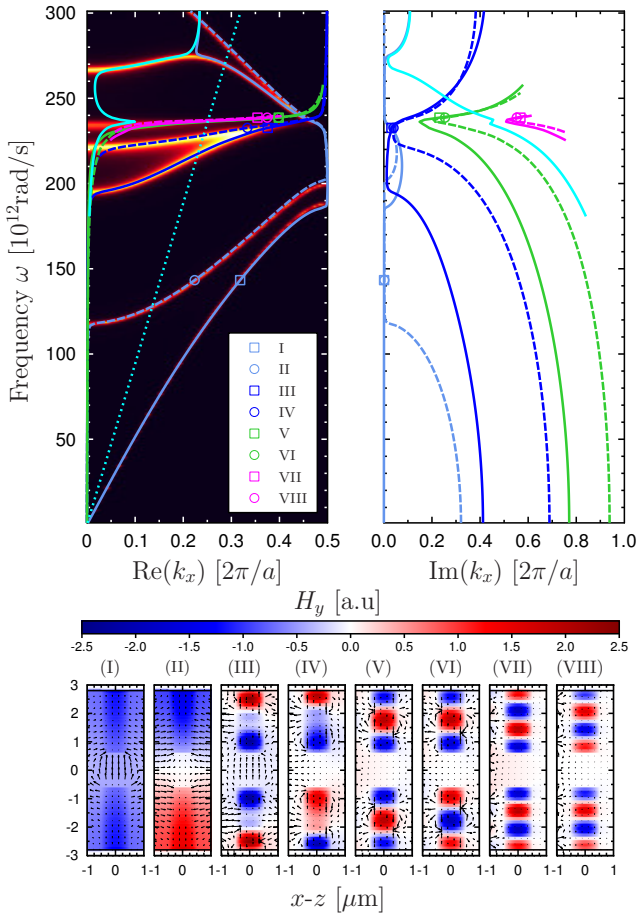

Figure 4.23: Top: The real and imaginary part of k_x vs ω curves of the two rectangular hyperbolic metamaterial arrays structure depicted in Fig. 4.21 for gap size of $g = 1000$ nm and surface-parallel wavevector along x direction. The corresponding transmission factor map is superimposed as the background. Bottom: Field distributions in x-z plane of the marked modes on the dispersion curves. The color maps present the y component of the magnetic field and the arrow maps presents the electric field in x-z plane.

majorly z-polarized, the HMMs act effectively as a dielectric. Field distributions at mode points III-VIII show the higher z-order modes. These modes are mainly confined in the rectangular-shaped HMM and less coupled between periods, suggesting their less dispersive bands or more localized resonance nature.

By checking several rectangular-shaped HMM of different widths. We find out that the resonance frequencies of such modes are heavily determined by the width of the rectangular-shaped HMM. A simple way to interpret such rectangular-shaped HMMs is that they can be treated as coupled MIM resonators. The very thin metal layer [$t_m = 20$ nm] allows the coupling of GSPs supported by the neighboring MIM structures. The coupling of these modes supported by each rectangular-shaped HMM array structure eventually leads to the brighter bands in Fig. 4.22.

4.3.2 Trapezoidal-Shaped Hyperbolic Metamaterial Array

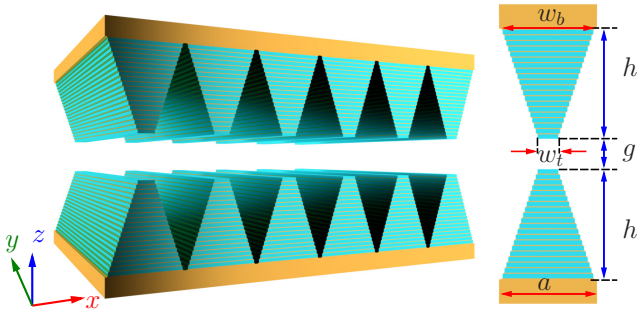

Figure 4.24: Geometry of two trapezoidal-shaped hyperbolic metamaterial gratings separated by a vacuum gap g. The long side and the short side of the trapezoidal cross section are $w_t = 400$ nm and $w_b = 1900$ nm, respectively. The height of the trapezoidal cross section is $h = 2300$ nm. The period of the grating is $a = 2000$ nm. The cyan layers denote dielectric and the golden layers denote gold.

Inspired by the rectangular-shaped HMM array structure, we are interested in seeing if profile-patterned HMM array with a varying width will give rise to an ultrabroadband super-Planckian RHT. It is straightforward to deploy a trapezoidal-shaped HMM array structure as depicted in Fig. 4.24. It consists of two identical 1D periodic array of trapezoidal-shaped HMM on a gold substrate separated by a vacuum gap g without any lateral offset or rotation. The trapezoidal-shaped cross-section with short base of $w_t = 400$ nm, long base of $w_b = 1900$ nm, and height of $h = (95\text{ nm} + 20\text{ nm}) \times 20 = 2.3$ μm is resembled by rectangular-shaped multilayers of different widths. The period of the HMM array is the same as we used for rectangular-shaped HMM arrays, i.e., $a = 2000$ nm.

Figures 4.25(a)-4.25(d) plot the transmission factor $\mathcal{T}_j(\omega, k_x, 0)$ between plates with such two trapezoidal-shaped HMM arrays for surface-parallel wavevector along x direction. The calculation of four different gap sizes $g = 5000,\ 1000,\ 500,\ 50$ nm are carried out using a RCWA based method. For a larger gap size $g = 5000$ nm [see Fig. 4.25(a)], the contributions are mainly from the propagating modes above the

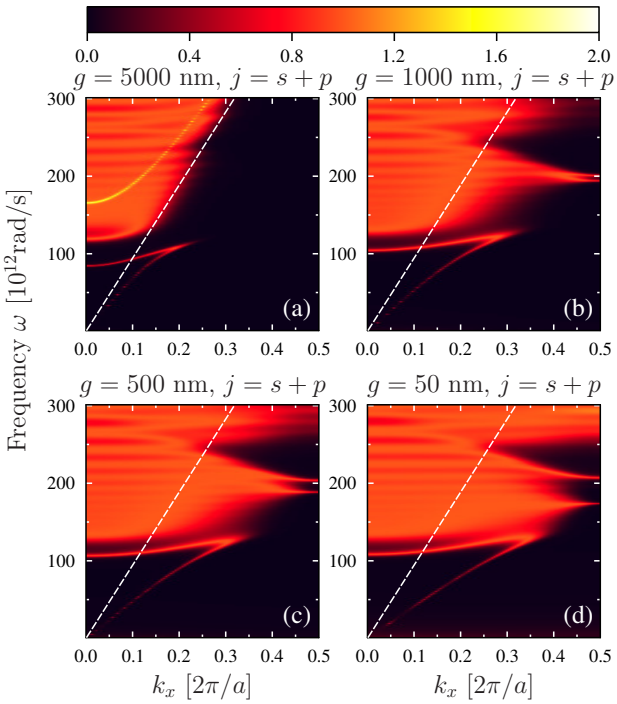

Figure 4.25: Transmission factor $\mathcal{T}_j(\omega, k_x, 0)$ between two trapezoidal-shaped hyperbolic metamaterial gratings depicted in Fig. 4.24 for surface-parallel wavevector along x direction at different gap sizes of (a) $g = 5000$ nm, (b) $g = 1000$ nm, (c) $g = 500$ nm, and (d) g=50 nm. The dashed white line indicates the light line in vacuum.

light line. There only exist two low-frequency surface modes below the light line. The brightest band, which has a maximum value close to two, is due to the degeneration of s- and p-polarized modes. The s-polarized contribution to the RHT comes from guided modes mostly inside the vacuum gap, as in the MIM structure discussed in Chapter 2, which is characterized by a low-frequency cutoff in the transmission-factor map. The hyperbolic medium behaves like a metal for s-polarized light [electric field direction along y direction] as dictated by the material's negative permittivity $\epsilon_\perp$ along y direction. The contribution from s polarization is not present for smaller gap sizes, because the s-polarized mode experiences a cutoff at smaller gap sizes. The contribution of p-polarized light to RHT exists more extensively, both above [propagating modes] and below [surface modes] light line. The two low-frequency surface-mode bands become more separated as gap size decreases. These two bands correspond to a symmetric and antisymmetric mode

pair resulted from splitting of SPPs supported by individual gold-HMM interfaces. They share the same origin as those discussed previously for rectangular-shaped HMM. Besides the two low-frequency bands, the structure presents ultrabroadband transmission factors, which are also of p-polarized nature. High transmission factor extends even to the 1st Brillouin zone boundary, i.e. $k_x = 0.5\ [2\pi/a]$, for smaller gaps. From the plots in Fig. 4.25, it is obvious that the trapezoidal-shaped HMM-based plates not can not only achieve far-field RHT close to blackbody limit, but also, when their separation is small, achieve super-Planckian RHT by making use of most near-field states.

To unveil the underlying physical origin of the broadband p-polarized modes which play a major role in contributing to the RHT for surface-parallel wavevectors along x direction, we calculate the dispersion relation of the p-polarized modes [see also paper **IV**]. The dispersion curve can clearly outline the transmission factor map, which confirms the role of different modes in contributing to RHT. We check the mode profiles of serveral representative modes and find out that the modes contributing to the broadband transmission factor show typical GSP-like modes featuring enhanced magnetic fields [17, 114, 116]. Each trapezoidal-shaped HMM stack can be treated as a series of gap-plasmon resonators with varying widths. The resonance frequency of each resonator depends on its width, which dictates such a trapezoidal-shaped HMM stack has an ultrabroadband resonance coupled to propagating modes [i.e., states above light line]. We observe at certain frequency a second-order GSP excited at the base of the HMM stack where the resonator is wider; at the same time a first-order GSP resonance is excited at a narrower part of the stack. Compared to rectangular-shaped HMM which has a uniform width, the GSP bands are enriched in numbers and occupy a broader frequency range by the introduction of trapezoidal-shaped HMM. Note also that these GSP modes also form symmetric and antisymmetric pairs due to adjacency of the two HMM arrays, which is more clearly shown for the rectangular-shaped HMM array discussed in the previous subsection [see Fig. 4.23].

A full characterization of RHT between two plates requires a calculation of transmission factors for all surface-parallel wavevectors over a frequency range relevant to the temperature setting as given by Eq. 4.3. Besides transmission factor maps along x direction shown in Fig. 4.25, we need to compute transmission factors for all possible surface-parallel wavevector directions. The result at a representative frequency [see also paper **IV**] shows that for larger gap sizes the contributions come from both s- and p-polarized propagating modes [inside light cone]. It is interesting to notice that, at the gap size of $g = 5000$ nm, the distributions of transmission factors for s and p polarizations are almost complementary to each other; summation of them would lead to a nearly unitary transmission factor filling the whole light cone. As the gap size decreases, the contribution from modes outside the light cone becomes dominant, suggesting more and more near-field interactions. At $g = 1000$ nm, the heat flux over a broad frequency range is already beyond the far-field blackbody limit [see Figs. 4.26(a) and 4.26(b)]. Both s- and p-polarized thermally exicted photons contribute to RHT over a broad (k_x, k_y) combinations.

For better understanding of these RHT channels, we examine the profiles of modes with ($k_x = 0, k_y \neq 0$) [see also paper **IV**]. These modes are nothing but guided modes by the HMM array. It is easy to imagine that each trapezoidal-shaped HMM stack, being structurally invariant in y direction, functions like an optical waveguide [204]; a single profile-patterned HMM array is simply a waveguide array; two arrays form a super-waveguide array. Due to very high contrast in permittivity values, the guided modes are hybrid in polarization, which means they can be excited by either s- or p-polarized photons. The modes inside the light cone manifests GSP modes, propagating along y while radiating out to free space. Again for s polarization, there exists a series of modes outside light cone. These modes are due to symmetric and antisymmetric couplings between the fundamental modes or higher order modes supported by each HMM arrary. It is worth noting that, unlike all dielectric waveguides, these hybrid modes supported by HMM waveguide exhibit a reverse ordering, i.e. higher order with a larger k_y, due to the indefinite permittivity tensor [164, 204]. We also observe a G-SPP mode, as in the GMP structure, mainly confined inside the vacuum gap between the two HMM arrays, which does not exist in an individual HMM array.

Finally, in Fig. 4.26(a) we plot the integrated transmission factor $\Phi(\omega)$ between the two HMM arrays at four different gap sizes. We also superimpose the integrated transmission factor Φ_{BB} between two blackbodies. At lower frequencies the trapeziodal-shaped HMM array shows a higher transmission factor than the blackbody. This is mainly contributed by the coupling between waveguide modes of the trapezoidal-shaped HMM waveguide and the G-SPP modes inside the vacuum gap. The coupling of GSP modes between two HMM arrays starts playing an important role for angular frequency above around 120×10^{12} rad/s [see Fig. 4.25]. As the gap size decreases down to 50 nm, the transmission factors between two HMM arrays get beyond that between two blackbodies almost over all the spectra range we studied, which enables us to achieve an ultrabroadband super-Planckian RHT. We demonstrate super-Planckian radiation by comparing the spectral heat flux between two HMM arrays with temperature $T_1 = 301$ K, $T_2 = 300$ K to that between two blackbodies with the same temperature configuration in Fig. 4.26(b). At the very near field with $g = 50$ nm, HMM array performs much better than blackbodies, ranging from 4.4 to 1236 times of that between two blackbodies across the whole spectra range we study. We predict that the performance can be even improved by using 2D periodic HMM pyramids arrays which support GSP resonance for both s- and p-polarized photons with almost all surface-parallel wavevector directions.

In conclusion, we have numerically demonstrated a broadband super-Planckian RHT achieved using profile-patterned HMM arrays. Unlike the modes supported by homogeneous multilayered HMM or nanowire arrays, which are dependent on filling ratio between metals and dielectrics, modal properties of profile-patterned HMMs are also geometry dependent. This provides us another degree of freedom to further engineer the spectral properties of the near-field RHT. Profile-patterned HMM holds a great potential for achieving an ultrabroadband tailorable super-Plackian RHT, which can be critical for an optimum energy transfer through vacuum.

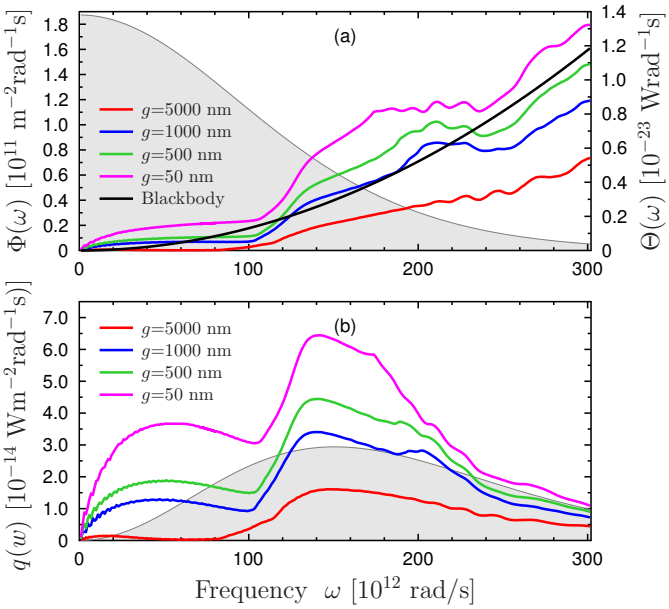

Figure 4.26: (a) Integrated transmission factor spectra $\Phi(\omega)$ for the structure depicted in Fig. 4.24 with gap size of $g = 5000$ nm, $g = 1000$ nm, $g = 500$ nm, and $g = 50$ nm and that between two blackbodies. (b) Spectral heat flux $q(\omega)$ for the same configuration as shown in (a) for $T_1 = 301$ K and $T_2 = 300$ K. The gray lines with shading in (a) and (b) indicate Planck's oscillator term $\Theta(\omega, 301\text{ K}) - \Theta(\omega, 300\text{ K})$ and spectral heat flux between two blackbodies for the same temperature configuration, respectively.

Chapter 5

Conclusions and Future Work

This thesis has presented the enhanced near-field radiative heat transfer (RHT) between plasmonic nanostructures. We express the heat flux between two 1D/2D periodic structures in terms of reflection matrix $\mathbf{R}$ which is obtained by a scattering approach based on rigorous coupled-wave analysis (RCWA). Li's factorization rules are deployed in this method to improve the convergence rate for structures with high permittivity contrast, such as in grooved metal plates (GMPs). Utilizing this method, we numerically demonstrated that by nanostructuring of metal surfaces one can turn metal plate from a good reflector thus poor thermal emitter in the infrared regime into a good candidate for radiative thermal energy transfer at both near- and far-field limits. The underlying physical mechanism of the artificial surface modes that lead to this strong enhancement in the RHT is revealed by calculating photonic band diagrams and examining mode profiles via complex wavenumber eigenvalue simulation (CWES) based on FEM.

More concretely, we have numerically confirmed the enhanced near-field RHT with two categories of plasmonic nanostructures, i.e., GMP structure and profile-patterned hyperbolic metamaterial (HMM). For the GMP structure, we started with a simple 1D-periodic geometry to identify the role of spoof surface plasmon polariton (SSPP) modes and waveguide modes which contribute to the RHT. With the understanding of the role of SSPPs, we showed that by introducing a supercell structure with multiple groove depths or filling the grooves with a high refractive index dielectric material, RHT can be further enhanced and even exceed that between two blackbodies or two homogeneous plates of a polar dielectric. A 2D GMP structure with a C_4 symmetry was then proposed to achieve more frequency-selective enhanced RHT. For the profile-patterned hyperbolic metamaterial (HMM) structure, we chose a HMM consisting of 20 deep subwavelength Si-Au bilayers, which is a type-II HMM in the infrared regime. We studied the RHT between two such HMM plates patterned in either rectangular- or trapezoidal-shaped HMM arrays on a gold substrate. The trapezoidal-shaped HMM structure shows an ultrabroadband super-Planckian RHT. We attribute this ultrabroadband RHT to several coupled modes,

including SSPP modes, gap surface plasmon (GSP) modes, and hybrid waveguide modes. Both GMP and profile-patterned HMM structures exhibit a great flexibility in spectral tailorability, which is critically demanded by many applications such as TPVs.

Although the numerical method we demonstrated can handle 2D periodic structure, the computational time and resources consumed by especially the full **k**-space simulation are huge. In the future, we should take the advantage of the symmetry of the structure under study and implement the group-theoretic approach [205–208] to reduce the computational load[‡]. It is also interesting to upgrade the code to take lateral offset [79] and rotation [209] into consideration in calculation of RHT between two nanostructured plates. The sensitivity of RHT to lateral offsets or rotations is critical for carrying out experimental measurements and practical applications. From a material perspective, the noble metals, such as gold, silver, copper, etc., cannot survive under high temperature environment as high as 1000 °C, especially when they are engineered into nanostructures. For TPV applications, the emitters are usually working at high temperatures in order to match the efficiency curves of photovolatics, e.g., GaSb (1.71 μm, 1420 °C) [201], InGaAsSb on GaSb (2.48 $\sim$ 2.07 μm, 970 $\sim$ 1130 °C) [202], InAs (3.55μm, 540 °C) [203], they are definitely not a good choice of materials. Refractory plasmonic materials [210–213], such as TiN, HfN, TaN, HfO_3, etc., with chemical stability at temperature above 800 °C even in nanometer sizes, are promising candidates for utilizing plasmonic nanostructures to enhance RHT for near-field TPV applications. Numerical computation using such refractory plasmonic materials are therefore desirable.

[‡]The simulations were performed on resources provided by the Swedish National Infrastructure for Computing (SNIC) at PDC Centre for High Performance Computing (PDC-HPC). https://www.pdc.kth.se/resources/computers/tegner/hardware

Chapter 6

Guideline to Papers

I J. Dai, S. A. Dyakov, and M. Yan, "Enhanced near-field radiative heat transfer between corrugated metal plates: Role of spoof surface plasmon polaritons," Phys. Rev. B **92**, 035419 (2015).

Author's Contribution: Jin Dai contributes to conception, design, numerical simulations, interpretation of the numerical results, and drafting the paper.

II J. Dai, S. A. Dyakov, and M. Yan, "Radiative heat transfer between two dielectric-filled metal gratings," Phys. Rev. B **93**, 155403 (2016).

Author's Contribution: Jin Dai contributes to conception, design, numerical simulations, interpretation of the numerical results, and drafting the paper.

III J. Dai, S. A. Dyakov, S. I. Bozhevolnyi, and M. Yan, "Near-field radiative heat transfer between metasurfaces: A full-wave study based on two-dimensional grooved metal plates," Phys. Rev. B **94**, 125431 (2016).

Author's Contribution: Jin Dai contributes to conception, design, numerical simulations, interpretation of the numerical results, and drafting the paper.

IV J. Dai, F. Ding, S. I. Bozhevolnyi, and M. Yan, "Ultrabroadband super-planckian radiative heat transfer with profile-patterned hyperbolic metamaterial," arXiv preprinted arXiv:1609.04319 (2016).

Author's Contribution: Jin Dai contributes to conception, design, numerical simulations, interpretation of the numerical results, and drafting the paper.

Bibliography

[1] J. C. Maxwell, *Theory of Heat* (Courier Corporation, 2012).

[2] G. Kirchhoff, Monatsber. Königl. Preuss. Akad. Wiss. Berlin , 783 (1859).

[3] G. Kirchhoff, Ann. Physik **185**, 275 (1860).

[4] J. Stefan, ma-naturw. kaiser. Akda. Wiss **279**, 391 (1879).

[5] L. Boltzmann, Ann. Physik **258**, 291 (1884).

[6] W. Wien, Ann. Physik **294**, 662 (1896).

[7] M. Planck, Verhandl. Dtsc. Phys. Ges. **2**, 202 (1900).

[8] M. Planck, Verhandl. Dtsc. Phys. Ges. **2**, 237 (1900).

[9] F. Lord Rayleigh, Phil. Mag. Ser. 5 **49**, 539 (1900).

[10] M. Planck, Ann. Physik **309**, 553 (1901).

[11] A. Einstein, Dtsc. Phys. Ges. **18** (1916).

[12] J. B. Pendry, A. J. Holden, W. J. Stewart, and I. Youngs, Phys. Rev. Lett. **76**, 4773 (1996).

[13] J. B. Pendry, A. J. Holden, D. J. Robbins, and W. J. Stewart, IEEE Trans. Microw. Theory Tech. **47**, 2075 (1999).

[14] R. A. Shelby, D. R. Smith, and S. Schultz, Science **292**, 77 (2001).

[15] J. B. Pendry, Phys. Rev. Lett. **85**, 3966 (2000).

[16] J. B. Pendry, D. Schurig, and D. R. Smith, Science **312**, 1780 (2006).

[17] J. Hao, J. Wang, X. Liu, W. J. Padilla, L. Zhou, and M. Qiu, Appl. Phys. Lett. **96**, 251104 (2010).

[18] N. Liu, M. Mesch, T. Weiss, M. Hentschel, and H. Giessen, Nano Lett. **10**, 2342 (2010).

[19] K. Aydin, V. E. Ferry, R. M. Briggs, and H. A. Atwater, Nat. Commun. **2**, 517 (2011).

[20] M. Yan, J. Dai, and M. Qiu, J. Opt. **16**, 025002 (2014).

[21] M. G. Nielsen, A. Pors, O. Albrektsen, and S. I. Bozhevolnyi, Opt. Express **20**, 13311 (2012).

[22] T. Søndergaard, S. M. Novikov, T. Holmgaard, R. L. Eriksen, J. Beermann, Z. Han, K. Pedersen, and S. I. Bozhevolnyi, Nat. Commun. **3**, 969 (2012).

[23] Y. Cui, K. H. Fung, J. Xu, H. Ma, Y. Jin, S. He, and N. X. Fang, Nano Lett. **12**, 1443 (2012).

[24] F. Ding, Y. Jin, B. Li, H. Cheng, L. Mo, and S. He, Laser Photon. Rev. **8**, 946 (2014).

[25] A. Cattoni, P. Ghenuche, A.-M. Haghiri-Gosnet, D. Decanini, J. Chen, J.-L. Pelouard, and S. Collin, Nano Lett. **11**, 3557 (2011).

[26] E. E. Narimanov and A. V. Kildishev, Appl. Phys. Lett. **95**, 041106 (2009).

[27] Z. Ruan, M. Yan, C. W. Neff, and M. Qiu, Phys. Rev. Lett. **99**, 113903 (2007).

[28] M. Yan, Z. Ruan, and M. Qiu, Phys. Rev. Lett. **99**, 233901 (2007).

[29] A. Alù and N. Engheta, Phys. Rev. Lett. **100**, 113901 (2008).

[30] E. M. Smith, D. Panjwani, J. Ginn, A. P. Warren, C. Long, P. Figuieredo, C. Smith, J. Nath, J. Perlstein, N. Walter, C. Hirschmugl, R. E. Peale, and D. Shelton, Appl. Opt. **55**, 2071 (2016).

[31] A. Narayanaswamy and G. Chen, Phys. Rev. B **70**, 125101 (2004).

[32] M.-W. Tsai, T.-H. Chuang, C.-Y. Meng, Y.-T. Chang, and S.-C. Lee, Appl. Phys. Lett. **89**, 173116 (2006).

[33] I. Puscasu and W. L. Schaich, Appl. Phys. Lett. **92**, 233102 (2008).

[34] J. A. Schuller, T. Taubner, and M. L. Brongersma, Nat. Photon. **3**, 658 (2009).

[35] X. Liu, T. Tyler, T. Starr, A. F. Starr, N. M. Jokerst, and W. J. Padilla, Phys. Rev. Lett. **107**, 045901 (2011).

[36] J. A. Mason, S. Smith, and D. Wasserman, Appl. Phys. Lett. **98**, 241105 (2011).

[37] M. De Zoysa, T. Asano, K. Mochizuki, A. Oskooi, T. Inoue, and S. Noda, Nat. Photon. **6**, 535 (2012).

[38] N. Mattiucci, G. D'Aguanno, A. Alù, C. Argyropoulos, J. V. Foreman, and M. J. Bloemer, Appl. Phys. Lett. **100**, 201109 (2012).

[39] W. L. Schaich and I. Puscasu, Phys. Rev. B **86**, 245423 (2012).

[40] J.-J. Greffet, R. Carminati, K. Joulain, J.-P. Mulet, S. Mainguy, and Y. Chen, Nature **416**, 61 (2002).

[41] Z. Liu, H. Lee, Y. Xiong, C. Sun, and X. Zhang, Science **315**, 1686 (2007).

[42] J. Rho, Z. Ye, Y. Xiong, X. Yin, Z. Liu, H. Choi, G. Bartal, and X. Zhang, Nat. Commun. **1**, 143 (2010).

[43] S. S. Kruk, Z. J. Wong, E. Pshenay-Severin, K. O'Brien, D. N. Neshev, Y. S. Kivshar, and X. Zhang, Nat. Commun. **7** (2016).

[44] M. Planck, *The Theory of Heat Radiation* (Courier Corporation, 2013).

[45] S. Rytov, Akademii Nauk SSSR, Moscow (1953).

[46] S. Rytov, Y. A. Kravtsov, and V. Tatarskii, *Elements of Random Fields (Principles of Statistical Radiophysics vol 3)* (Berlin, Springer, 1989).

[47] D. Polder and M. van Hove, Phys. Rev. B **4**, 3303 (1971).

[48] C. M. Hargreaves, Phys. Lett. A **30**, 491 (1969).

[49] K. Joulain, J.-P. Mulet, F. Marquier, R. Carminati, and J.-J. Greffet, Surf. Sci. Rep. **57**, 59 (2005).

[50] M. Francoeur, M. P. Mengüç, and R. Vaillon, Appl. Phys. Lett. **93**, 043109 (2008).

[51] P.-O. Chapuis, S. Volz, C. Henkel, K. Joulain, and J.-J. Greffet, Phys. Rev. B **77**, 035431 (2008).

[52] M. F. Vaillon, M. P. Mengüç, and Rodolphe, J. Phys. D: Appl. Phys. **43**, 75501 (2010).

[53] R. S. Ottens, V. Quetschke, S. Wise, a. a. Alemi, R. Lundock, G. Mueller, D. H. Reitze, D. B. Tanner, and B. F. Whiting, Phys. Rev. Lett. **107**, 014301 (2011).

[54] T. Kralik, P. Hanzelka, M. Zobac, V. Musilova, T. Fort, and M. Horak, Phys. Rev. Lett. **109**, 224302 (2012).

[55] S. A. Dyakov, J. Dai, M. Yan, and M. Qiu, Phys. Rev. B **90**, 045414 (2014).

[56] S.-A. Biehs, M. Tschikin, R. Messina, and P. Ben-Abdallah, Appl. Phys. Lett. **102**, 131106 (2013).

[57] Y. Guo and Z. Jacob, Opt. Express **21**, 15014 (2013).

[58] Y. Guo, C. L. Cortes, S. Molesky, and Z. Jacob, Appl. Phys. Lett. **101**, 131106 (2012).

[59] B. Song, Y. Ganjeh, S. Sadat, D. Thompson, A. Fiorino, V. Fernández-Hurtado, J. Feist, F. J. Garcia-Vidal, J. C. Cuevas, P. Reddy, and E. Meyhofer, Nat. Nanotechnol. **10**, 253 (2015).

[60] P. Ben-Abdallah, S.-A. Biehs, and K. Joulain, Phys. Rev. Lett. **107**, 114301 (2011).

[61] K. Sasihithlu and A. Narayanaswamy, Phys. Rev. B **83**, 161406 (2011).

[62] P. Ben-Abdallah, K. Joulain, J. Drevillon, and C. Le Goff, Phys. Rev. B **77**, 075417 (2008).

[63] A. W. Rodriguez, M. T. H. Reid, and S. G. Johnson, Phys. Rev. B **86**, 220302 (2012).

[64] B. Guha, C. Otey, C. B. Poitras, S. Fan, and M. Lipson, Nano Lett. **12**, 4546 (2012).

[65] A. Kittel, W. Müller-Hirsch, J. Parisi, S.-A. Biehs, D. Reddig, and M. Holthaus, Phys. Rev. Lett. **95**, 224301 (2005).

[66] A. Narayanaswamy, S. Shen, and G. Chen, Phys. Rev. B **78**, 115303 (2008).

[67] E. Rousseau, A. Siria, G. Jourdan, S. Volz, F. Comin, J. Chevrier, and J.-J. Greffet, Nat. Photon. **3**, 514 (2009).

[68] S. Shen, A. Narayanaswamy, and G. Chen, Nano Lett. **9**, 2909 (2009).

[69] S. Shen, A. Mavrokefalos, P. Sambegoro, and G. Chen, Appl. Phys. Lett. **100**, 233114 (2012).

[70] P. J. van Zwol, L. Ranno, and J. Chevrier, Phys. Rev. Lett. **108**, 234301 (2012).

[71] P. J. van Zwol, S. Thiele, C. Berger, W. A. de Heer, and J. Chevrier, Phys. Rev. Lett. **109**, 264301 (2012).

[72] L. Worbes, D. Hellmann, and A. Kittel, Phys. Rev. Lett. **110**, 134302 (2013).

[73] A. P. McCauley, M. T. H. Reid, M. Krüger, and S. G. Johnson, Phys. Rev. B **85**, 165104 (2012).

[74] K. Kim, B. Song, V. Fernández-Hurtado, W. Lee, W. Jeong, L. Cui, D. Thompson, J. Feist, M. T. H. Reid, F. J. García-Vidal, J. C. Cuevas, E. Meyhofer, and P. Reddy, Nature **528**, 387 (2015).

[75] A. W. Rodriguez, O. Ilic, P. Bermel, I. Celanovic, J. D. Joannopoulos, M. Soljačić, and S. G. Johnson, Phys. Rev. Lett. **107**, 114302 (2011).

[76] S.-A. Biehs, P. Ben-Abdallah, F. S. S. Rosa, K. Joulain, and J.-J. Greffet, Opt. Express **19**, A1088 (2011).

[77] S.-A. Biehs, M. Tschikin, and P. Ben-Abdallah, Phys. Rev. Lett. **109**, 104301 (2012).

[78] R. Guérout, J. Lussange, F. S. S. Rosa, J.-P. Hugonin, D. A. R. Dalvit, J.-J. Greffet, A. Lambrecht, and S. Reynaud, Phys. Rev. B **85**, 180301 (2012).

[79] J. Lussange, R. Guérout, F. S. S. Rosa, J.-J. Greffet, A. Lambrecht, and S. Reynaud, Phys. Rev. B **86**, 085432 (2012).

[80] J. Dai, S. A. Dyakov, and M. Yan, Phys. Rev. B **92**, 035419 (2015).

[81] J. Dai, S. A. Dyakov, and M. Yan, Phys. Rev. B **93**, 155403 (2016).

[82] J. Dai, S. A. Dyakov, S. I. Bozhevolnyi, and M. Yan, Phys. Rev. B **94**, 125431 (2016).

[83] X. Liu and Z. Zhang, ACS Photonics **2**, 1320 (2015).

[84] J. Shi, B. Liu, P. Li, L. Y. Ng, and S. Shen, Nano Lett. **15**, 1217 (2015).

[85] X. Liu, R. Z. Zhang, and Z. Zhang, ACS Photonics **1**, 785 (2014).

[86] L. Zhu, A. P. Raman, and S. Fan, Proc. Natl. Acad. Sci. USA **112**, 12282 (2015).

[87] E. Rephaeli, A. Raman, and S. Fan, Nano Lett. **13**, 1457 (2013).

[88] A. P. Raman, M. A. Anoma, L. Zhu, E. Rephaeli, and S. Fan, Nature **515**, 540 (2014).

[89] M. Laroche, R. Carminati, and J.-J. Greffet, J. Appl. Phys. **100**, 063704 (2006).

[90] K. Park, S. Basu, W. King, and Z. Zhang, J. Quant. Spectrosc. Radiat. Transfer **109**, 305 (2008).

[91] C. R. Otey, W. T. Lau, and S. Fan, Phys. Rev. Lett. **104**, 154301 (2010).

[92] S. Basu and M. Francoeur, Appl. Phys. Lett. **98**, 113106 (2011).

[93] L. Zhu, C. R. Otey, and S. Fan, Phys. Rev. B **88**, 184301 (2013).

[94] H. Iizuka and S. Fan, J. Appl. Phys. **112**, 024304 (2012).

[95] Y. Yang, S. Basu, and L. Wang, Appl. Phys. Lett. **103**, 163101 (2013).

[96] H. Iizuka and S. Fan, J. Quant. Spectrosc. Radiat. Transfer **148**, 156 (2014).

[97] K. Ito, K. Nishikawa, H. Iizuka, and H. Toshiyoshi, Appl. Phys. Lett. **105**, 253503 (2014).

[98] K. I. Garcia-Garcia and J. Alvarez-Quintana, Int. J. Thermophys. **81**, 76 (2014).

[99] L. Zhu and S. Fan, Phys. Rev. Lett. **117**, 134303 (2016).

[100] K. Joulain, Y. Ezzahri, J. Drevillon, B. Rousseau, and D. D. S. Meneses, Opt. Express **23**, A1388 (2015).

[101] A. Ghanekar, J. Ji, and Y. Zheng, Appl. Phys. Lett. **109**, 123106 (2016).

[102] L. P. Wang and Z. M. Zhang, NANOSC MICROSC THERM **17**, 337 (2013).

[103] P. Ben-Abdallah and S.-A. Biehs, Phys. Rev. Lett. **112**, 044301 (2014).

[104] K. Joulain, J. Drevillon, Y. Ezzahri, and J. Ordonez-Miranda, Phys. Rev. Lett. **116**, 200601 (2016).

[105] V. Kubytskyi, S.-A. Biehs, and P. Ben-Abdallah, Phys. Rev. Lett. **113**, 074301 (2014).

[106] S. A. Dyakov, J. Dai, M. Yan, and M. Qiu, J. Phys. D: Appl. Phys. **48**, 305104 (2015).

[107] J. B. Pendry, J. Phys. Condens. Matter **11**, 6621 (1999).

[108] R. Wood, Phil. Mag. Ser. 6 **4**, 396 (1902).

[109] D. Pines, Rev. Mod. Phys. **28**, 184 (1956).

[110] U. Fano, Phys. Rev. **103**, 1202 (1956).

[111] R. H. Ritchie, Phys. Rev. **106**, 874 (1957).

[112] H. Raether, *Surface Plasmons on Smooth Surfaces* (Springer, 1988).

[113] R. Zia, M. D. Selker, P. B. Catrysse, and M. L. Brongersma, J. Opt. Soc. Am. A **21**, 2442 (2004).

[114] S. I. Bozhevolnyi and T. Søndergaard, Opt. Express **15**, 10869 (2007).

[115] E. N. Economou, Phys. Rev. **182**, 539 (1969).

[116] J. Jung, T. Søndergaard, and S. I. Bozhevolnyi, Phys. Rev. B **79**, 035401 (2009).

[117] P. B. Johnson and R. W. Christy, Phys. Rev. B **6**, 4370 (1972).

[118] E. D. Palik, *Handbook of Optical Constants of Solids*, Vol. 3 (Academic press, 1998).

[119] M. Moskovits, Rev. Mod. Phys. **57**, 783 (1985).

[120] A. Otto, I. Mrozek, H. Grabhorn, and W. Akemann, J. Phys. Condens. Matter **4**, 1143 (1992).

[121] A. M. Michaels, M. Nirmal, and L. E. Brus, J. Am. Chem. Soc. **121**, 9932 (1999).

[122] H. Xu, E. J. Bjerneld, M. Käll, and L. Börjesson, Phys. Rev. Lett. **83**, 4357 (1999).

[123] W. L. Barnes, A. Dereux, and T. W. Ebbesen, Nature **424**, 824 (2003).

[124] H.-T. Chen, W. J. Padilla, J. M. O. Zide, A. C. Gossard, A. J. Taylor, and R. D. Averitt, Nature **444**, 597 (2006).

[125] H. Zhou, F. Ding, Y. Jin, and S. He, Progress In Electromagnetics Research **119**, 449 (2011).

[126] F. Bigourdan, F. Marquier, J.-P. Hugonin, and J.-J. Greffet, Opt. Express **22**, 2337 (2014).

[127] J. B. Pendry, L. Martín-Moreno, and F. J. Garcia-Vidal, Science **305**, 847 (2004).

[128] F. J. Garcia-Vidal, L. Martín-Moreno, and J. B. Pendry, J. Opt. A: Pure and Appl. Opt. **7**, S97 (2005).

[129] L. Shen, X. Chen, Y. Zhong, and K. Agarwal, Phys. Rev. B **77**, 075408 (2008).

[130] N. Yu, Q. J. Wang, M. A. Kats, J. A. Fan, S. P. Khanna, L. Li, A. G. Davies, E. H. Linfield, and F. Capasso, Nat. Mater. **9**, 730 (2010).

[131] A. Alù, G. D'Aguanno, N. Mattiucci, and M. J. Bloemer, Phys. Rev. Lett. **106**, 123902 (2011).

[132] M. A. Kats, D. Woolf, R. Blanchard, N. Yu, and F. Capasso, Opt. Express **19**, 14860 (2011).

[133] X. Gao, J. H. Shi, H. F. Ma, W. X. Jiang, and T. J. Cui, J. Phys. D: Appl. Phys. **45**, 505104 (2012).

[134] X. Shen, T. J. Cui, D. Martin-Cano, and F. J. Garcia-Vidal, Proc. Natl. Acad. Sci. USA **110**, 40 (2013).

[135] H. F. Ma, X. Shen, Q. Cheng, W. X. Jiang, and T. J. Cui, Laser Photon. Rev. **8**, 146 (2014).

[136] S.-H. Kim, S. S. Oh, K.-J. Kim, J.-E. Kim, H. Y. Park, O. Hess, and C.-S. Kee, Phys. Rev. B **91**, 035116 (2015).

[137] C. R. Williams, S. R. Andrews, S. A. Maier, A. I. Fernández-Domínguez, L. Martín-Moreno, and F. J. García-Vidal, Nat. Photon. **2**, 175 (2008).

[138] A. B. Khanikaev, S. H. Mousavi, G. Shvets, and Y. S. Kivshar, Phys. Rev. Lett. **105**, 126804 (2010).

[139] S. A. Maier, S. R. Andrews, L. Martín-Moreno, and F. J. García-Vidal, Phys. Rev. Lett. **97**, 176805 (2006).

[140] A. Pors, E. Moreno, L. Martin-Moreno, J. B. Pendry, and F. J. Garcia-Vidal, Phys. Rev. Lett. **108**, 223905 (2012).

[141] D. Lu, J. J. Kan, E. E. Fullerton, and Z. Liu, Nat. Nanotechnol. **9**, 48 (2014).

[142] H. N. S. Krishnamoorthy, Z. Jacob, E. Narimanov, I. Kretzschmar, and V. M. Menon, Science **336**, 205 (2012).

[143] M. A. Noginov, H. Li, Y. A. Barnakov, D. Dryden, G. Nataraj, G. Zhu, C. E. Bonner, M. Mayy, Z. Jacob, and E. E. Narimanov, Opt. Lett. **35**, 1863 (2010).

[144] Z. Jacob, I. I. Smolyaninov, and E. E. Narimanov, Appl. Phys. Lett. **100**, 181105 (2012).

[145] J. Zhou, A. F. Kaplan, L. Chen, and L. J. Guo, ACS Photonics **1**, 618 (2014).

[146] V. P. Drachev, V. A. Podolskiy, and A. V. Kildishev, Opt. Express **21**, 15048 (2013).

[147] A. Poddubny, I. Iorsh, P. Belov, and Y. Kivshar, Nat. Photon. **7**, 948 (2013).

[148] L. Ferrari, C. Wu, D. Lepage, X. Zhang, and Z. Liu, Progress in Quantum Electronics **40**, 1 (2015).

[149] Z. Liu, H. Lee, Y. Xiong, C. Sun, and X. Zhang, Science **315**, 1686 (2007).

[150] Z. Jacob, J.-Y. Kim, G. V. Naik, A. Boltasseva, E. E. Narimanov, and V. M. Shalaev, Appl. Phys. B **100**, 215 (2010).

[151] J. Kim, V. P. Drachev, Z. Jacob, G. V. Naik, A. Boltasseva, E. E. Narimanov, and V. M. Shalaev, Opt. Express **20**, 8100 (2012).

[152] M. Y. Shalaginov, S. Ishii, J. Liu, J. Liu, J. Irudayaraj, A. Lagutchev, A. V. Kildishev, and V. M. Shalaev, Appl. Phys. Lett. **102**, 173114 (2013).

[153] X. Ni, G. V. Naik, A. V. Kildishev, Y. Barnakov, A. Boltasseva, and V. M. Shalaev, Appl. Phys. B **103**, 553 (2011).

[154] K. V. Sreekanth, T. Biaglow, and G. Strangi, J. Appl. Phys. **114**, 134306 (2013).

[155] K. V. Sreekanth, A. De Luca, and G. Strangi, Sci. Rep. **3**, 3291 (2013).

[156] T. Tumkur, G. Zhu, P. Black, Y. A. Barnakov, C. E. Bonner, and M. A. Noginov, Appl. Phys. Lett. **99**, 151115 (2011).

[157] H. Shen, D. Lu, B. VanSaders, J. J. Kan, H. Xu, E. E. Fullerton, and Z. Liu, Phys. Rev. X **5**, 021021 (2015).

[158] T. U. Tumkur, L. Gu, J. K. Kitur, E. E. Narimanov, and M. A. Noginov, Appl. Phys. Lett. **100**, 161103 (2012).

[159] H. N. S. Krishnamoorthy, Z. Jacob, E. Narimanov, I. Kretzschmar, and V. M. Menon, Science **336**, 205 (2012).

[160] J. Rho, Z. Ye, Y. Xiong, X. Yin, Z. Liu, H. Choi, G. Bartal, and X. Zhang, Nat. Commun. **1**, 143 (2010).

[161] S. Ishii, A. V. Kildishev, E. Narimanov, V. M. Shalaev, and V. P. Drachev, Laser Photon. Rev. **7**, 265 (2013).

[162] A. J. Hoffman, L. Alekseyev, S. S. Howard, K. J. Franz, D. Wasserman, V. A. Podolskiy, E. E. Narimanov, D. L. Sivco, and C. Gmachl, Nat. Mater. **6**, 946 (2007).

[163] G. V. Naik, J. Liu, A. V. Kildishev, V. M. Shalaev, and A. Boltasseva, Proc. Natl. Acad. Sci. USA **109**, 8834 (2012).

[164] X. Yang, J. Yao, J. Rho, X. Yin, and X. Zhang, Nat. Photon. **6**, 450 (2012).

[165] B. Wood, J. B. Pendry, and D. P. Tsai, Phys. Rev. B **74**, 115116 (2006).

[166] Y. Liu, G. Bartal, and X. Zhang, Opt. Express **16**, 15439 (2008).

[167] J. J. Saarinen, S. M. Weiss, P. M. Fauchet, and J. E. Sipe, J. Appl. Phys. **104**, 013103 (2008).

[168] J. Yao, Z. Liu, Y. Liu, Y. Wang, C. Sun, G. Bartal, A. M. Stacy, and X. Zhang, Science **321**, 930 (2008).

[169] J. Yao, Y. Wang, K.-T. Tsai, Z. Liu, X. Yin, G. Bartal, A. M. Stacy, Y.-L. Wang, and X. Zhang, Phil. Trans. R. Soc. A **369**, 3434 (2011).

[170] P. Evans, W. R. Hendren, R. Atkinson, G. A. Wurtz, W. Dickson, A. V. Zayats, and R. J. Pollard, Nanotechnology **17**, 5746 (2006).

[171] M. A. Noginov, Y. A. Barnakov, G. Zhu, T. Tumkur, H. Li, and E. E. Narimanov, Appl. Phys. Lett. **94**, 151105 (2009).

[172] V. P. Ulin and S. G. Konnikov, Semiconductors **41**, 832 (2007).

[173] A. G. Cullis, L. T. Canham, and P. D. J. Calcott, J. Appl. Phys. **82**, 909 (1997).

[174] L. V. Alekseyev, V. A. Podolskiy, and E. E. Narimanov, Adv. Optoelectron **2012** (2012).

[175] A. A. Orlov, P. M. Voroshilov, P. A. Belov, and Y. S. Kivshar, Phys. Rev. B **84**, 045424 (2011).

[176] O. Kidwai, S. V. Zhukovsky, and J. E. Sipe, Opt. Lett. **36**, 2530 (2011).

[177] M. Tschikin, S.-A. Biehs, R. Messina, and P. Ben-Abdallah, J. Opt. **15**, 105101 (2013).

[178] M. S. Mirmoosa, F. Rüting, I. S. Nefedov, and C. R. Simovski, J. Appl. Phys. **115**, 234905 (2014).

[179] H. B. Callen and T. A. Welton, Phys. Rev. **83**, 34 (1951).

[180] L. D. Landau and E. Lifshitz, *Statistical Physics* (Pergamon, Oxford, 1980).

[181] G. S. Agarwal, Phys. Rev. A **11**, 230 (1975).

[182] M. Francoeur, M. P. Mengüç, and R. Vaillon, J. Quant. Spectrosc. Radiat. Transfer **110**, 2002 (2009).

[183] L. Li and C. W. Haggans, J. Opt. Soc. Am. A **10**, 1184 (1993).

[184] M. G. Moharam, E. B. Grann, D. A. Pommet, and T. K. Gaylord, J. Opt. Soc. Am. A **12**, 1068 (1995).

[185] M. G. Moharam, D. A. Pommet, E. B. Grann, and T. K. Gaylord, J. Opt. Soc. Am. A **12**, 1077 (1995).

[186] G. Granet and B. Guizal, J. Opt. Soc. Am. A **13**, 1019 (1996).

[187] P. Lalanne and G. M. Morris, J. Opt. Soc. Am. A **13**, 779 (1996).

[188] L. Li, J. Opt. Soc. Am. A **13**, 1870 (1996).

[189] G. Granet, J. Opt. Soc. Am. A **16**, 2510 (1999).

[190] D. M. Whittaker and I. S. Culshaw, Phys. Rev. B **60**, 2610 (1999).

[191] E. Popov and M. Nevière, J. Opt. Soc. Am. A **18**, 2886 (2001).

[192] S. G. Tikhodeev, A. L. Yablonskii, E. A. Muljarov, N. A. Gippius, and T. Ishihara, Phys. Rev. B **66**, 045102 (2002).

[193] A. Lambrecht and V. N. Marachevsky, Phys. Rev. Lett. **101**, 160403 (2008).

[194] G. Bimonte, Phys. Rev. A **80**, 042102 (2009).

[195] R. Messina and M. Antezza, Phys. Rev. A **84**, 042102 (2011).

[196] R. Guérout, J. Lussange, H. B. Chan, A. Lambrecht, and S. Reynaud, Phys. Rev. A **87**, 052514 (2013).

[197] C. Luo, A. Narayanaswamy, G. Chen, and J. D. Joannopoulos, Phys. Rev. Lett. **93**, 213905 (2004).

[198] A. W. Rodriguez, O. Ilic, P. Bermel, I. Celanovic, J. D. Joannopoulos, M. Soljačić, and S. G. Johnson, Phys. Rev. Lett. **107**, 114302 (2011).

[199] L. Li, J. Opt. Soc. Am. A **14**, 2758 (1997).

[200] S.-A. Biehs, F. S. Rosa, and P. Ben-Abdallah, *Nanoscale radiative heat transfer and its applications* (INTECH Open Access Publisher, 2012).

[201] A. W. Bett and O. V. Sulima, Semicond. Sci. Technol. **18**, S184 (2003).

[202] M. W. Dashiell, J. F. Beausang, H. Ehsani, G. J. Nichols, D. M. Depoy, L. R. Danielson, P. Talamo, K. D. Rahner, E. J. Brown, S. R. Burger, P. M. Fourspring, W. F. TopperJr., P. F. Baldasaro, C. A. Wang, R. K. Huang, M. K. Connors, G. W. Turner, Z. A. Shellenbarger, G. Taylor, J. Li, R. Martinelli, D. Donetski, S. Anikeev, G. L. Belenky, and S. Luryi, IEEE Trans. Electron Devices **53**, 2879 (2006).

[203] C. A. Wang, H. K. Choi, S. L. Ransom, G. W. Charache, L. R. Danielson, and D. M. DePoy, Appl. Phys. Lett. **75**, 1305 (1999).

[204] M. Yan, L. Thylén, and M. Qiu, Opt. Express **19**, 3818 (2011).

[205] B. Bai and L. Li, J. Opt. A: Pure and Appl. Opt. **7**, 783 (2005).

[206] B. Bai and L. Li, J. Opt. A: Pure and Appl. Opt. **7**, 271 (2005).

[207] B. Bai and L. Li, J. Opt. Soc. Am. A **23**, 572 (2006).

[208] B. Bai and L. Li, Opt. Commun. **262**, 140 (2006).

[209] R. Guérout, C. Genet, A. Lambrecht, and S. Reynaud, EPL (Europhysics Letters) **111**, 44001 (2015).

[210] G. V. Naik, V. M. Shalaev, and A. Boltasseva, Adv. Mater. **25**, 3264 (2013).

[211] U. Guler, A. Boltasseva, and V. M. Shalaev, Science **344**, 263 (2014).

[212] W. Li, U. Guler, N. Kinsey, G. V. Naik, A. Boltasseva, J. Guan, V. M. Shalaev, and A. V. Kildishev, Adv. Mater. **26**, 7959 (2014).

[213] P. N. Dyachenko, S. Molesky, A. Y. Petrov, M. Störmer, T. Krekeler, S. Lang, M. Ritter, Z. Jacob, and M. Eich, Nat. Commun. **7**, 11809 (2016).